

박사 학위논문
Ph. D. Dissertation

선형과 비선형 해석을 위한 연속체 역학 기반
빔 유한요소의 개발

Development of Continuum Mechanics Based Beam Elements for Linear and
Nonlinear Analysis



윤 경 호 (尹 景 虎 Yoon, Kyungho)
기계항공시스템학부 해양시스템공학전공
School of Mechanical, Aerospace and Systems Engineering,
Division of Ocean Systems Engineering

KAIST

2015

Development of Continuum Mechanics Based Beam
Elements for Linear and Nonlinear Analysis



Development of Continuum Mechanics Based Beam Elements for Linear and Nonlinear Analysis

Advisor : Professor Phill-Seung Lee

by

Kyungho Yoon

School of Mechanical, Aerospace and Systems Engineering

Division of Ocean Systems Engineering

KAIST

A thesis submitted to the faculty of KAIST in partial fulfillment of the requirements for the degree of Doctor of Philosophy in the School of Mechanical, Aerospace and Systems Engineering, Division of Ocean Systems Engineering. The study was conducted in accordance with Code of Research Ethics¹

한국과학기술원



SINCE 1971

2014. 11. 3

Approved by

Professor Phill-Seung Lee

¹ Declaration of Ethical Conduct in Research: I, as a graduate student of KAIST, hereby declare that I have not committed any acts that may damage the credibility of my research. These include, but are not limited to: falsification, thesis written by someone else, distortion of research findings or plagiarism. I affirm that my thesis contains honest conclusions based on my own careful research under the guidance of my thesis advisor.

Development of Continuum Mechanics Based Beam Elements for Linear and Nonlinear analysis

Kyungho Yoon

The present dissertation has been approved by the dissertation committee
as a Ph. D. dissertation at KAIST

11 (Month) 3 (Day), 2014 (Year)

Committee head 이 필 승 (인)

Committee member 오 일 권 (인)

Committee member 조 연 우 (인)

Committee member 임 세 영 (인)

Committee member 김 도 년 (인)

DOSE
20115476

윤 경 호. Yoon, Kyungho. Development of continuum mechanics based beam elements for Linear and Nonlinear Analysis. 선형과 비선형 해석을 위한 연속체 역학 기반 빔 유한요소의 개발. School of Mechanical, Aerospace and Systems Engineering, Division of Ocean Systems Engineering. 2015. 116 p. Advisor Prof. Lee, Phill-Seung. Text in English

ABSTRACT

Beams are very important and widely used structural members in engineering practice. Recently, applications of beams have been rapidly extended from classical metallic structures to nano- and bio-structures, in which finite element method is a tool dominantly adopted for analysis and design. To cover such new applications, the modeling capability and nonlinear performance become more important in finite element analysis of beams.

First, we develop continuum mechanics beam elements in which fully coupled 3-D behaviors among stretching, bending, shearing, twisting and warping are considered. The beam element is directly degenerated from an assemblage of 3-D solid elements. The element has cross-sectional discretization which provides enhanced modeling capabilities for complicated 3-D geometries including curved and twisted geometries, varying cross-sections, and arbitrary cross-sectional shapes.

Second, we propose a new and efficient displacement model to ensure the continuity of warping in beams with discontinuously varying arbitrary cross-sections. The entire warping displacement field is constructed by a combination of the three basis warping function, one free warping function and two interface warping functions, with warping degrees of freedom (DOFs). A new method to simultaneously calculate the free warping function and the corresponding twisting center is also introduced. Based on this method, the interface warping functions and the twisting centers at the interface cross-sections are obtained by solving a set of coupled equations at the interface of two different cross-sections.

Third, we present the nonlinear formulation and performance of continuum mechanics based beam elements, in which fully coupled 3D behaviors of stretching, bending, shearing, twisting, and warping are automatically considered. The beam elements are directly degenerated from assemblages of 3D solid elements under the assumptions of Timoshenko beam theory. Therefore, cross-sectional discretization is possible and the elements can model complicated 3D beam geometries including curved and twisted geometries, varying cross-sections, eccentricities, and arbitrary cross-sectional shapes. In particular, the proposed nonlinear formulation can accurately predict large twisting behaviors coupled with stretching, bending, shearing, and warping. Through various numerical examples, we demonstrate the geometric (and material) nonlinear performance of the continuum mechanics based beam elements.

Finally, we propose a new numerical method to improve nonlinear performance: the eigen recomposition. We classify and investigate the miss leading phenomena in internal virtual work via eigenvalue analysis. In order to improve the internal virtual work, the obtained nonlinear stiffness matrix is recomposed by the assumed eigenvector and the corresponding estimated eigenvalue. The performance of the recomposed stiffness matrix is demonstrated through several beam element examples.

Keywords: Finite element method; Beam element; Torsion; Twisting; Warping;

Table of Contents

Abstract	i
Table of Contents	iii
List of Tables	vi
List of Figures	vii

Chapter 1. Introduction

1.1 Research Motivation	1
1.2 Overview	2
1.2.1 On Degenerated Beam Elements	2
1.2.2 On Mathematical Warping Theory	3
1.3 Research Object & Contents	5

Chapter 2. Continuum Mechanics Based Beam Elements

2.1 Kinematic Description	6
2.1.1 Interpolation of Geometry	7
2.1.2 Interpolation of Displacement	9
2.1.3 Interpolation of Warping Displacement	10
2.2 Calculation of Warping Function	11
2.3 Numerical Integration	14
2.4 Numerical Studies	16
2.4.1 Rectangular Cross-section Beam Problem	17
2.4.2 Tubular and Angle Cross-section Beam Problem	20
2.4.3 Various Solid Cross-section Beam Problem	24
2.4.4 Curved Wide Flange Cross-section Beam Problem	26
2.4.5 Varying Wide Flange Cross-section Beam Problem	30
2.4.6 Wind Turbine Blade Problem	32
2.5 Concluding Remarks	32

Chapter 3. Continuity of Warping Displacement in Discontinuously Varying Beam

3.1 Motivation	34
3.2 Modeling of Warping Displacement Fields	35
3.2.1 New Warping Displacement Model	36

3.2.2 Free Warping Function.....	38
3.2.3 Interface Warping Function	40
3.3 Numerical Studies	43
3.3.1 Step Varying Rectangular Cross-section Problem.....	45
3.3.2 Discontinuously Varying Thin-walled Cross-section Problem	48
3.3.3 Partially Constrained Warping Problem	51
3.3.4 Curved Beam Problem with a Discontinuously Varying Cross-section	52
3.4 Concluding Remarks	54
 Chapter 4. General Nonlinear Formulation of Continuum Mechanics Based Beam	
4.1 Large Displacement Kinematics.....	55
4.2 Green-Lagrange strain	60
4.3 Incremental Equilibrium Equation	62
4.4 Elastoplastic Material Model.....	64
4.5 Numerical Studies	65
4.5.1 Patch Test	67
4.5.2 45 Degree Bend Beam Problem.....	69
4.5.3 Curved Beam Problem	69
4.5.4 Z-shaped Cross-section Beam Problem.....	72
4.5.5 Cross-shaped Cross-section Beam Problem.....	73
4.5.6 Twisted Cantilever Beam Problem	78
4.5.7 Lateral Post-buckling Problem.....	81
4.5.8 Framed Dome Problem	83
4.6 Concluding Remarks	83
 Chapter 5. Eigen Recomposition Method to Improve Nonlinear Performance	
5.1 Motivation	85
5.2 Stiffening of Rigid Body Rotation	86
5.3 Deficiency of Shear Eigenmode	88
5.4 Eigenvalue Analysis.....	89
5.5 Eigen Recomposition Method	92
5.6 Numerical Studies	93
5.6.1 Straight Cantilever Problem	93
5.6.2 Right Angle Frame Problem.....	96

5.6.3 Portal Frame Problem	96
5.6.4 Offshore Jacket Problem	98
5.7 Concluding Remarks	100
Chapter 6. Conclusions & Future works	
6.1 Conclusions	101
6.2 Future Works	102
Appendix	104
Reference	107



List of Tables

Table 1-1 Formulation of mathematical warping theories and its modeling capability	4
Table 2-1 Reference values used for angles of twist at the loaded tips for rectangular cross-section beam problems with free warping	17
Table 2-2 Angles of twist at the loaded tips for tubular cross-section beam problems under uniform torsion with constrained warping. Eight 16-node cross-sectional elements are used and N denotes the number of beam elements used	21
Table 2-3 Angles of twist at the loaded tips for tubular cross-section beam problems under uniform torsion with constrained warping. Eight 2-node beam elements are used ($N = 8$).....	21
Table 2-4 Angles of twist at the loaded tips for angle cross-section beam problems under non-uniform torsion with constrained warping. Three 16-node cross-sectional elements are used and N denotes the number of beam elements used.	22
Table 2-5 Angles of twist at the loaded tips for angle cross-section beam problems under non-uniform torsion with constrained warping. Eight 2-node beam elements are used ($N = 8$)	22
Table 2-6 Angles of twist at the loaded tip for various solid cross-section beam problems	23
Table 2-7 Angles of twist and displacement w at the loaded tip for the curved wide flange cross-section beam problems according to the warping direction used. Four 2-node beam elements ($N = 4$) and 16-node cross-sectional elements are used.....	26
Table 2-8 Angles of twist and displacement w at the loaded tip for the curved wide flange cross-section beam problems with constrained warping according to D/R . 16-node cross-sectional elements are used and N denotes the number of beam elements used	26
Table 2-9 Angles of twist at the loaded tips for the varying wide flange cross-section beam problems under uniform torsion. Four 3-node beam elements are used ($N = 4$)	28
Table 4-1 Large twisting analysis of the beam, shell, and solid element models in the numerical examples considered in this study	66
Table 4-2 Free tip displacements when $F_z = 600$ in 45 degree bend beam problem	68

List of Figures

Figure 1-1 The concept of the general degenerated element.	2
Figure 1-2 The existing degeneration procedure for constructing beam element with a wide flange cross-section.	3
Figure 1-3 A cantilever beam subjected to torsional moment and its warped cross-section.	4
Figure 2-1 The concept of the continuum mechanics based beam finite element with sectional discretization. In this figure, the beam is modeled by nine 3-D solid elements and the model has 3 cross-sectional planes along the beam length.	6
Figure 2-2 Continuum mechanics beam finite element with cross-sectional mesh. (a) 3-node beam finite element, (b) Cross-sectional mesh at beam node k	7
Figure 2-3 Directions of warping displacements. (a) and (b) Correct and wrong warping directions at a sharing node, (c) Warping direction same to the longitudinal direction of beam elements, (d) and (e) Uniform and varying warping directions at varying beam cross-sections.	10
Figure 2-4 A cross-section to solve St. Venant equations. (a) Cross-sectional Cartesian coordinate system (point of origin C_k) and a vector normal to cross-sectional boundary, (b) Cross-sectional mesh and the center of twist T_k	12
Figure 2-5 Straight cantilever beam problems (a) Uniform torsion problem (a straight beam subjected to torsional moment at the free tip) (b) Non-uniform torsion problem (a straight beam subjected to uniformly distributed torsional moment).	14
Figure 2-6 Various cross-sectional discretizations with different interpolation functions and meshes. (a) Single element meshes (1st, 2nd, 3rd and 4th order interpolations), (b) 1x1, 3x3, 6x6 and 12x12 linear meshes, (c) Distorted meshes ($\tan \theta = 0$, $b/4a$, $2b/4a$ and $3b/4a$) of 16-node cross-sectional elements.	15
Figure 2-7 Relative errors in angle of twist at the loaded tip for various aspect ratios (a/b); (a) Corresponding to the interpolation orders in Fig. 2-6(a); (b) Corresponding to the meshes of linear cross-sectional elements in Fig. 2-6(b); (c) Corresponding to the distorted cross-sectional meshes in Fig.2-6(c).	16
Figure 2-8 Tubular and angle cross-sections with various thicknesses and cross-sectional meshes used. (a) Tubular cross-sections ($a = 0.5$, $b = 2$), (b) Angle cross-sections ($a = 1$, $b = 2$).	18
Figure 2-9 Solid element models and meshes used. (a) Tubular cross-section beam with 128x20 meshes of 27-node solid elements ($p_1 = 0.125N$, $p_2 = 0.25N$), (b) Angle cross-section beam with 76x20 meshes of 27-node solid elements ($p_1 = 0.0125N/m$, $p_2 = 0.025N/m$).	19
Figure 2-10 Method to measure angles of twist in the solid element models of the tubular and angle cross-section beams.	20

Figure 2-11 Cross-sectional discretizations of various solid cross-sections modeled on the yz -plane. (a) Trapezoidal cross-section modeled by a single 16-node cross-sectional element ($a = 2$, $b = 4$), (b) Circular cross-section modeled by a single 16-node cross-sectional element ($R = 2$), (c) Solid cross-section with four splines modeled by seven 16-node cross-sectional elements ($R = 2$, $a = 1$). 22

Figure 2-12 Distributions of transverse shear stress- xy in the solid cross-section with four splines. (Left: cross-sectional meshes used, Right: stress distribution) (a) Solid element solution calculated by 630 27-node solid elements. 63 and 10 solid elements are used on cross-sections and in beam length, respectively. (b) Beam element solution calculated by three beam elements. Seven 16-node cross-sectional elements are used. 23

Figure 2-13 Curved wide flange cross-section beam problems. (a) Geometry of the curved wide flange cross-section beam problem and cross-sectional mesh used, (b) Shell finite element models used. 24

Figure 2-14 Angle of twist and displacement w along the beam length in the curved wide flange cross-section beam problems. 25

Figure 2-15 Curved wide flange cross-section beam problems with three different D/R . (a) $D/R = 0.1$, (b) $D/R = 0.2$, (c) $D/R = 0.5$ 25

Figure 2-16 Varying wide flange cross-section beam problems. (a) Geometry of the varying wide flange cross-section beam problem and cross-sectional mesh used, (b) Shell finite element models used. 27

Figure 2-17 Angle of twist and displacement u along the beam length in the varying wide flange cross-section beam problems. 27

Figure 2-18 Varying wide flange cross-section beam problems with four different tapering degrees. (a) $\tan 0.5\theta = 0.025$ ($\theta = 2.864$ deg.), (b) $\tan 0.5\theta = 0.095$ ($\theta = 10.854$ deg.), (c) $\tan 0.5\theta = 0.225$ ($\theta = 25.361$ deg.), (d) $\tan 0.5\theta = 0.475$ ($\theta = 50.815$ deg.). 29

Figure 2-19 Displacement v and angle of twist along the beam length in varying wide flange cross-section beam problems with an eccentric end tip load ($\tan 0.5\theta = 0.025$). 29

Figure 2-20 Wind turbine blade problems. (a) Geometry of the wind turbine blade with a NACA airfoil and cross-sectional mesh used, (b) Loading conditions. Left: flexural-torsion case, Right: pure torsion case (resultant moment: $M_x = 2.0 N \cdot m$). 30

Figure 2-21 Shell element model for the wind turbine blade problems. 31

Figure 2-22 Displacements v , w and the angle of twist along the beam length in the wind turbine blade problems. (a) Flexural-torsion case. The displacements are given at point **Q**. (b) Pure torsion case. For the shell model, the angle of twist is evaluated from the relative displacements between two points **A** and **B** because the distribution of the angle is not uniform on the cross-section due to the effect of local deformation, but the angle of twist for the beam model is given at point **A**. 31

Figure 3-1 Various beam problems. (a) Beam problems with continuous varying cross-section (prismatic and tapered beams), (b) Beam problem with discontinuously varying cross-section.	34
Figure 3-2 Warping DOFs used for a discontinuously varying cross-section beam. (a) A discontinuously varying cross-section beam, (b) Finite element model and warping DOF used at each nodes, (c) Individual amplitude of the basis warping functions along the beam length.	36
Figure 3-3 Twisting kinematics and twisting center.	37
Figure 3-4 Cross-sections of a discontinuously varying cross-section beam. (a) Cross-sections (I) and (II), and their interface Ω_c , (b) Interconnected domain and twisting center, (c) Cross-sectional meshes used at the interface.	39
Figure 3-5 Three special cases for the interface warping functions. (a) Free interface, (b) Fully constrained interface, (c) Partially constrained interface.	40
Figure 3-6 Nodal warping DOFs used for (a) free-free, (b) constrained-free, (c) constrained-constrained warping problems.	42
Figure 3-7 Step varying rectangular cross-section problem. (a) Problem description (unit: m), (b) Beam element model, cross-sectional mesh used and the number of each nodal DOFs used, (c) Solid element model used.	43
Figure 3-8 Twisting centers in the step varying rectangular cross-section problem. (a) $(\lambda_y, \lambda_z) = (0, 0)$ for the free warping function of cross-section A , (b) $(\lambda_y, \lambda_z) = (0, -0.0833)$ for the interface warping function at $x = 5m$, (c) $(\lambda_y, \lambda_z) = (0, -0.25)$ for the free warping function of cross-section B	44
Figure 3-9 Numerical results along the beam length in the step varying rectangular cross-section problem. (a) Angle of twist, (b) Transverse displacement v at Q , (c) Shear stress σ_{xy} at Q , (d) Shear stress σ_{xz} at Q	44
Figure 3-10 Transverse shear stresses in the cross-section for the step varying rectangular cross-section problem. (a) σ_{xy} at $x = 2.5m$, (b) σ_{xy} at $x = 7.5m$, (c) σ_{xz} at $x = 2.5m$, (d) σ_{xz} at $x = 7.5m$	45
Figure 3-11 Discontinuously varying thin-walled cross-section beam problem. (a) Problem description (unit: m), (b) Beam element model, cross-sectional meshes used and the number of each nodal DOFs used, (c) Shell element model used.	46
Figure 3-12 Twisting centers in the discontinuously varying thin-walled cross-section beam problem. (a) $(0.0037, -0.4952)$ for the free warping function of cross-section A , (b) $(-0.3584, -0.1037)$ for the interface warping function at $x = 4m$, (c) $(-0.4163, 0)$ for the free warping function of cross-section B , (d) $(-0.3584, 0.1037)$ for the interface warping function at $x = 10m$, (e) $(0.0037, 0.4952)$ for the free warping function of cross-section C	47

Figure 3-13 Angle of twist and displacement v along the beam length in the discontinuously varying thin-walled cross-section beam problem. (a) Sampling points Q in the cross-sections, (b) Angle of twist (left) and displacement v (right).	47
Figure 3-14 Partially constrained warping problem. (a) Problem description (unit: m), (b) Beam element model, cross-sectional mesh used, constrained warping area (shaded area) and the numbers of the nodal DOFs used, (c) Solid element model used.	49
Figure 3-15 Twisting centers in the partially constrained warping problem. (a) $(\lambda_y, \lambda_z) = (0, -0.4369)$ for the interface warping function at $x = 0m$, (b) $(\lambda_y, \lambda_z) = (0, 0)$ for the free warping function.	50
Figure 3-16 Numerical results of the partially constrained warping problem. (a) Angle of twist, (b) Displacement v at Q , (c) Shear stress σ_{xy} at Q , (d) Shear stress σ_{xz} at Q	50
Figure 3-17 Curved beam problem. (a) Problem description (unit: m), (b) Beam element model, cross-sectional meshes used and the numbers of nodal DOFs used, (c) Solid element model used ($p_1 = 0.041667N$, $p_2 = 0.125N$, $p_3 = 1.0N$).	51
Figure 3-18 Numerical results of the curved beam problem along the beam length. (a) Angle of twist θ_φ for the load case - I, (b) Displacement w for the load case - I, (c) Angle of twist θ_φ for the load case - II, (d) Displacement w for the load case - II.	53
Figure 4-1 A 3-node continuum mechanics based beam element with cross-sectional discretization in the configuration at time t . In this figure, the continuum mechanics based beam element consists of 9 sub-beams.	55
Figure 4-2 A continuum mechanics based beam element: (a) beam nodes and coordinate system used in the beam element and (b) cross-sectional nodes and elements in the cross-sectional mesh.	56
Figure 4-3 Gauss integration points in the sub-beam element m in Fig. 1: (a) sub-beam element m and (b) gauss integration points in beam cross-sections.	63
Figure 4-4 Patch test with distorted meshes ($\varphi = s\pi/16$) and cross-sectional discretization.	66
Figure 4-5 Relative errors for various distortion angle parameter s . (a) x -directional load $F_x = 1000kN$ is applied at end tip and the errors are evaluated according to the x -directional displacement u , (b) y -directional moment $M_y = 10kN \cdot m$ is applied at end tip and the errors are evaluated according to the y -directional displacement v	67
Figure 4-6 45 degree bend beam problem with square cross-section and its discretization.	68
Figure 4-7 Load-displacement curves of free end tip in 45 degree bend beam problem.	68

Figure 4-8 Curved deep beam problem for verifying modeling capabilities. (a) Dimensions, beam finite element model and cross-sectional discretization, (b) Solid finite element model.	70
Figure 4-9 Numerical results of the curved deep beam problem along the beam length when $D/R = 0.1$. (a) Displacement u , (b) Displacement v , (c) Displacement w , (d) Associated deformed shape.	71
Figure 4-10 Relative difference at the loaded tip for curved deep beam problem according to the various D/R ratios.	71
Figure 4-11 Z-shaped cross-section beam problem and its longitudinal and cross-sectional meshes (unit: m).	71
Figure 4-12 Numerical results in the Z-shaped cross-section beam problem: (a) load-displacement curves and (b) distributions of the von Mises stress obtained from the continuum mechanics based beam elements.	72
Figure 4-13 Cross-shaped cross-section beam problem (unit: m): (a) longitudinal and cross-sectional meshes used in the beam model (5 beam elements) and (b) solid element model used (4,000 solid elements).	73
Figure 4-14 Numerical results for Load Case I in the cross-shaped cross-section beam problem: (a) and (b) load-displacement curves and deformed shapes, respectively, when five 2-node beam elements were used; and (c) and (d) load-displacement curves and deformed shapes, respectively, when five 3-node beam elements used. (Note: The center nodes of the 3-node beam elements are not plotted.).	74
Figure 4-15 Numerical results for Load Case II in the cross-shaped cross-section beam problem (five 2-node beam elements): (a) load-displacement curves, (b) distributions of the von Mises stress obtained from the beam element model, and (c) distributions of the von Mises stress obtained from the solid element model.	75
Figure 4-16 Twisted cantilever beam problem (unit: m): (a) problem description and (b) the longitudinal and cross-sectional meshes used (8 beam elements). The twisted geometry is modeled simply through changing the director vectors of the continuum mechanics based beams (${}^0\mathbf{V}_y^k$ and ${}^0\mathbf{V}_z^k$). (c) Shell element model (800 shell elements).	76
Figure 4-17 Numerical results in the twisted cantilever beam problem: (a) load-displacement curves at the free tip for Load Case I and (b) twist angle-stretch relationship for Load Case II when the prescribed displacement is applied.	76
Figure 4-18 Deformed shapes for Load Case II in the twisted cantilever beam problem: (a) shell element model and (b) beam element model.	77
Figure 4-19 Numerical results for Load Case III in the twisted cantilever beam problem: (a) load-displacement curve between M_x and θ_x at the free tip, (b) relationship between u and	

θ_x at the free tip, and (c) deformed shapes when the twist angles at the free tip are 0 , π , 2π , 3π , and 4π 78

Figure 4-20 Lateral post-buckling analyses of a straight cantilever beam with a mono-symmetric I-section (unit: *mm*): (a) the longitudinal and cross-sectional meshes used (8 beam elements), (b) four load cases, and (c) shell element model (180 shell elements). 79

Figure 4-21 Lateral post-buckling responses for the four load cases in Fig. 15(b): (a) and (b) elastic material used, and (c) and (d) elastoplastic material used. 80

Figure 4-22 Framed dome problem and the finite element discretization using the continuum mechanics based beam elements. 82

Figure 4-23 Numerical results of the framed dome problem: (a) load-displacement curves for the elastic analysis, (b) load-displacement curve for the elastoplastic analysis, and (c) deformed shapes. 82

Figure 5-1 The eight eigenpairs for 2D plane stress element. (a) Basic eigenmodes, (b) eigenmodes subjected to the uniform stress distribution. 85

Figure 5-2 An isoparametric body subjected to the rigid body rotation. 86

Figure 5-3 Isoparametric bodies subjected to the three types of shear deformation. 88

Figure 5-4 The numerical results of eigenvalue analysis for nonlinear stiffness matrix with respective stress component. 89

Figure 5-5 Straight cantilever problem with the beam element model (10 beam elements) and square cross-section (unit: *cm*). 94

Figure 5-6 Numerical results for Load Case I in the straight cantilever problem: (a) number of iteration used according to the applied load, (b) load-displacement curves. 94

Figure 5-7 Numerical results for Load Case II in the straight cantilever problem: (a) number of iteration used according to the applied load, (b) load-displacement curves. 94

Figure 5-8 Right angle frame problem with the beam element model (16 beam elements) and square cross-section (unit: *cm*). 95

Figure 5-9 Numerical results in the right angle frame problem: (a) number of iteration used according to the applied load, (b) load-displacement curves. 95

Figure 5-10 Deformed shapes in the right angle frame problem. 95

Figure 5-11 Portal frame problem with the beam element model (24 beam elements) and rectangular cross-section (unit: *cm*). 96

Figure 5-12 Load-displacement curves in portal frame problem. 97

Figure 5-13 Deformed shapes in the portal frame problem. 94

Figure 5-14 Offshore jacket problem with the beam element model (88 beam elements) and square cross-section (unit: *m*). 98

Figure 5-15 Load-displacement curves in the offshore jacket problem. 99

Figure 5-16 Deformed shapes in the offshore jacket problem. 99

Figure A-1 Initial and deformed configurations of a prismatic straight beam. 105



Chapter 1. Introduction

1.1 Research Motivation

The finite element method is widely used to predict physical phenomena in various engineering analyses, for example, solids and structures, heat transfer, fluids, electromagnetic fields. Although a voluminous amount of information on these techniques are published, the development of more effective procedures is still an important undertaking.

The classes of structural elements (truss, beam, plate, shell, and so on) are significant developments among the various methods to achieve an effective analysis. In particular, beam finite elements can be exploited to accomplish an efficient quantitative analysis to predict the global behavior of large scale problems.

Practical applications are increasingly involving more complicated geometries and small stressed regions for more efficient and economical material usage. Furthermore, new applications, such as nano- and bio-structures, aggravate difficulties encountered in beam finite element analyses. To address such complexity, the modeling capability and linear and nonlinear performance become more important.

Considerable efforts have been made over a number of years to develop beam theories and beam finite elements [1-22]. On the foundation of classical beam theories, recent works have focused on developing high-performance beam finite elements. As a result, modeling and analysis capabilities have been continuously improved, for example, see Refs. [23-49].

Continuum mechanics based formulations, meanwhile, have been very successfully used for the analysis of general beam structures [25-28]. They can easily represent general 3-D curved and twisted geometries including fully coupled complete strain states. Furthermore, the formulation is simple and straightforward. In spite of these great advantage, the original degenerated continuum beam elements can, in general, consider only rectangular cross-sections. While several studies has been made to overcome the limitations of the continuum beam element [25-28], the resulting new beams could not express arbitrary beam cross-sections.

In general, when a non-circular cross-section beam is subjected to twisting, the beam cross-sections do not remain in-plane during the deformations, and out-of-plane displacements occur. The effect is called warping. The behavior of warping is coupled with bending, shearing, and stretching under various loading conditions. The twisting and the coupling behaviors cannot be accurately predicted without considering warping. The inclusion of the warping effect in the beam element formulation is very important. To consider the fully coupled warping effect, the warping displacements can be included in the beam element formulation as additional displacement fields with corresponding degrees of freedom.

As discussed above, beam elements with high performance and modeling capabilities are required for more efficient analysis of new applications. In the present research, we develop new continuum mechanics based beam elements for linear and nonlinear analyses. The developed beam elements can contribute to analysis of complicated beam applications.

1.2 Overview

In this section, a short overview on the foundations of degenerated beam elements and on the mathematical warping theory is given.

1.2.1 On Degenerated Beam Elements

The concepts of geometry and displacement interpolations that have been employed in the formulation of continuum elements can also be employed in the evaluation of beam element matrices. However, whereas in the formulation of the continuum elements the displacements are interpolated in terms of nodal displacements, in the formulation of degenerated beam elements, the displacements are interpolated in terms of mid-point displacements and rotations, see Fig. 1-1.

The degeneration concept offers a simple and straightforward approach to incorporate geometric and material nonlinearity, as formulated directly from the continuum setting. Also, it inherently has superior modeling capability, easily and precisely representing complicated 3D geometries, curved and twisted geometries, and arbitrary and varying cross-sections. Furthermore, fully coupled stretching, bending, shearing, twisting, and warping behaviors can be automatically considered due to the fully coupled 3D strain states. Despite its superior characteristics, the degenerated beam formulation has not been dominantly used because of limitations related to difficulty in degeneration of complicated cross-sections and performance of geometric nonlinear analyses.

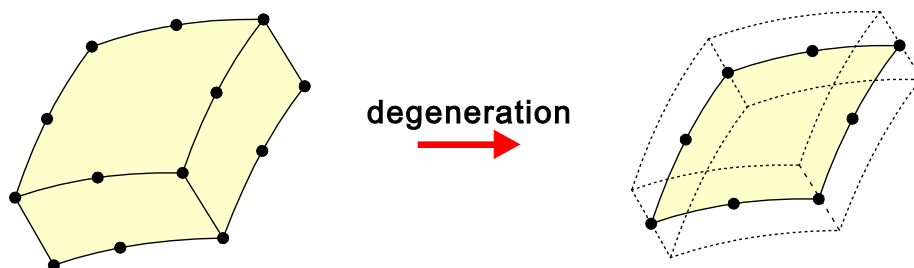


Figure 1-1. The concept of the general degenerated element.

The original formulation of degenerated beam elements is interpolated by mid-point displacements and rotations of rectangular cross-sections. In order to encompass various beam cross-sections, a new degeneration method using a square frame that includes the cross-sectional domain is introduced, as illustrated in Fig. 1-2. However, the resulting beams do not clearly model arbitrary cross-sections, and accompany complexity and difficulties in numerical integration.

Most of beam elements introduce problems that impede the performance of nonlinear analysis. For a long time, considerable efforts have been made to improve upon existing geometric nonlinear analyses. Although novel numerical methods have been successfully introduced, limitations remain. Furthermore, all of these studies solely focused on the non-vectorial nature of rotational variables. There is consequently still need for more insight into nonlinear analyses by adopting various perspectives and clearer guidelines.

1.2.2 On Mathematical Warping Theory

The inclusion of the warping effect in a beam finite element formulation is essential for predicting twisting actions, see Fig. 1-3 and 1-4. Various mathematical equations for modeling warping and twisting have been developed [19-23, 29-49]. In this section, four representative warping theories, St. Venant theory, Vlasov's thin-walled beam theory, Benscoter theory, and Jourasky theory, are introduced. The formulation and modeling capability of these theories are illustrated in Table 1-1.

In 1853 the French engineer Adhemar Jean Barrede Saint-Venant presented the classical torsion theory to the French Academy of Science. This theory is the basis for present-day analyses. St. Venant proved that a cross-section does not remain in-plane after twisting. The cross-section becomes a warped surface. In St. Venant torsion theory, the cross-section is assumed to warp freely out of its plane and the rate of the twisting angle is assumed to be constant. The warping deformation is modeled by a free warping function and constant twisting rate [19-21]. The free warping function can be obtained by solving the well-known St. Venant equations. This theory leads to some error in the case of non-uniform torsion, where the rate of the twisting angle varies along the length of the beam.

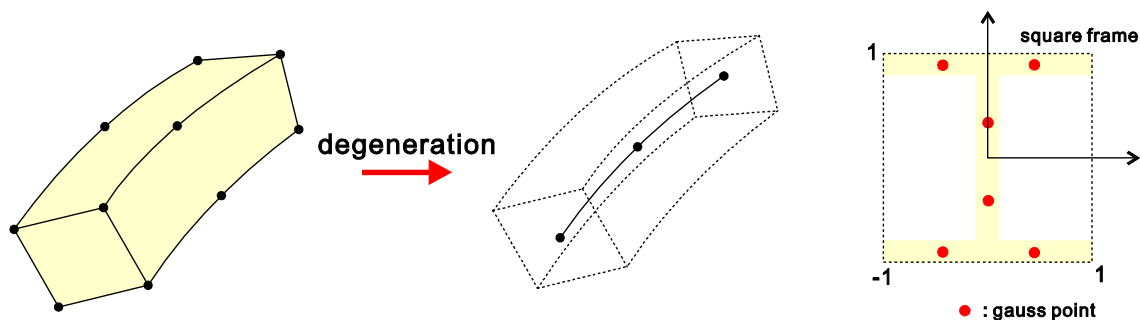


Figure 1-2. The existing degeneration procedure for constructing beam element with a wide flange cross-section.

Table 1-1. Formulation of mathematical warping theories and its modeling capability.

	St. Venant torsion theory	Vlasov's thin-walled theory	Benscoter theory	Jourawsky theory
Formulation	$u_w = f(y, z)$	$u_w = f(y, z)\theta'_x(x)$	$u_w = f(y, z)\alpha(x)$	$u_w = f(y, z)\theta'_x(x) + \psi(y, z)$
Unoform torsion	○	○	○	○
Non-uniform torsion	X	○	○	○
Secondary warping	X	X	○	○

In Vlasov's thin-walled beam theory [22], the warping deformation is modeled by a free warping function and the rate of the twisting angle. This theory can consider the non-uniform warping deformation effect but the transverse shear strain is neglected. Because of neglecting the transverse shear deformations through the wall thickness, some error arises in the case of closed cross-sections, where the shear stresses are statically indeterminate. This additional shear stress distribution is called the secondary shear effect.

In Benscoter theory, the warping deformation is modeled by a free warping function and longitudinal function as an arbitrary parameter. The employment of the arbitrary parameter allows approximation of the secondary shear effect. De ville De Goyet presented some examples to compare solution of a shell element model and an analytical solution based on Benscoter theory with a closed cross-section. These examples show the efficiency and sufficient accuracy of Benscoter theory.

In Jourawsky theory, the warping deformation is modeled by a free warping function with a longitudinal function according to the rate of the twisting angle and secondary warping function. The secondary warping function is evaluated from an equilibrium equation with St. Venant torsion and an induced secondary shear stress distribution. The consideration of the secondary warping function makes it possible to precisely take into account the secondary warping effect. However, evaluating this function also requires additional efforts and cost.

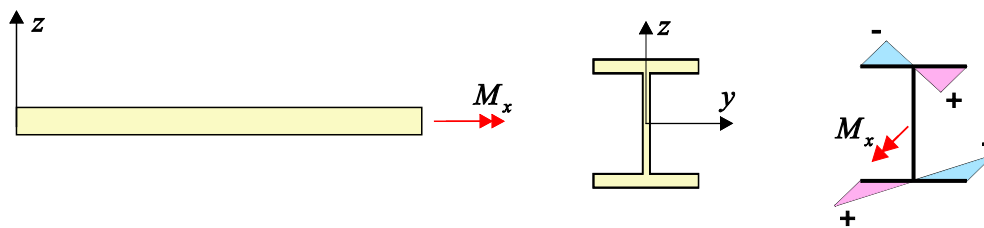


Figure 1-3. A cantilever beam subjected to torsional moment with wide flange cross-section and its warped cross-section.

1.3 Research Object & Contents

The objective of this research is to develop continuum mechanics based beam element for linear and nonlinear analysis. The developed element should satisfy following requirements:

- The warping effects fully coupled with stretching, bending, shearing, twisting are included.
- The formulation can handle all complicated 3D geometries including curved and twisted geometries, varying cross-sections, and arbitrary cross-sectional shapes.
- Inter-elemental continuity of warping displacement is ensured.
- High modeling capabilities and performance is available.

In the following chapter, we present the fundamental formulation of the continuum mechanics based beam elements in linear analysis. The superior modeling capability is demonstrated through the means of several numerical examples.

In chapter 3, we present a new and efficient method to model continuous warping displacement field in beam with discontinuously varying cross-sections. New equations to calculate the free warping function and the interface warping function are introduced.

In chapter 4, we present a geometric and material nonlinear formulation of the continuum mechanics based beam elements. The superior performance and modeling capability in nonlinear applications, particularly in large twisting problem, is demonstrated through the well-established numerical examples.

In chapter 5, we present a new method to improve nonlinear performance. The superior performance of the eigen recomposition method is illustrated through the several numerical examples.

Finally, in chapter 6, we present the conclusions and future works.

Chapter 2. Continuum Mechanics Based Beam Elements

In this chapter, we present the fundamental formulation of the continuum mechanics based beam elements in linear analysis. The superior modeling capability is demonstrated through the means of several numerical examples. [50]

2.1 Kinematic Description

In this section, we present the kinematics of the continuum mechanics based beam finite element which directly derived by degenerating an assemblage of 3-D solid finite elements.

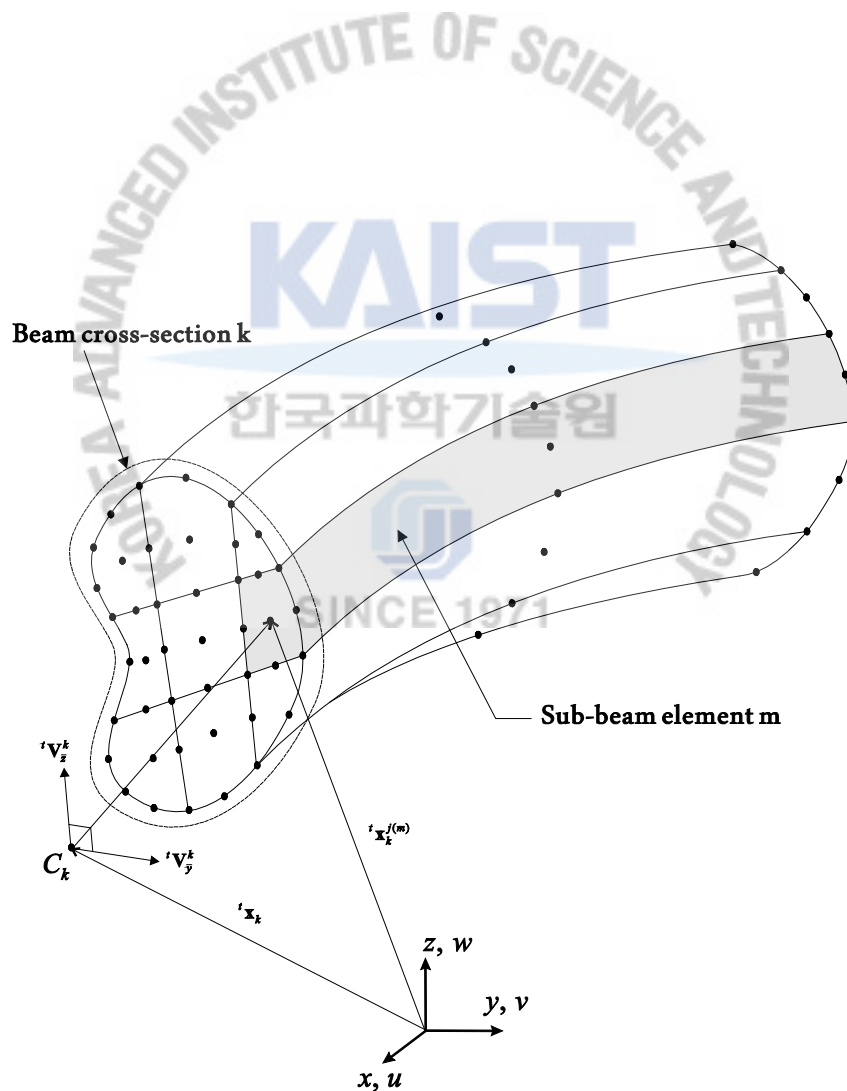


Figure 2-1. The concept of the continuum mechanics based beam finite element with sectional discretization. In this figure, the beam is modeled by nine 3-D solid elements and the model has 3 cross-sectional planes along the beam length.

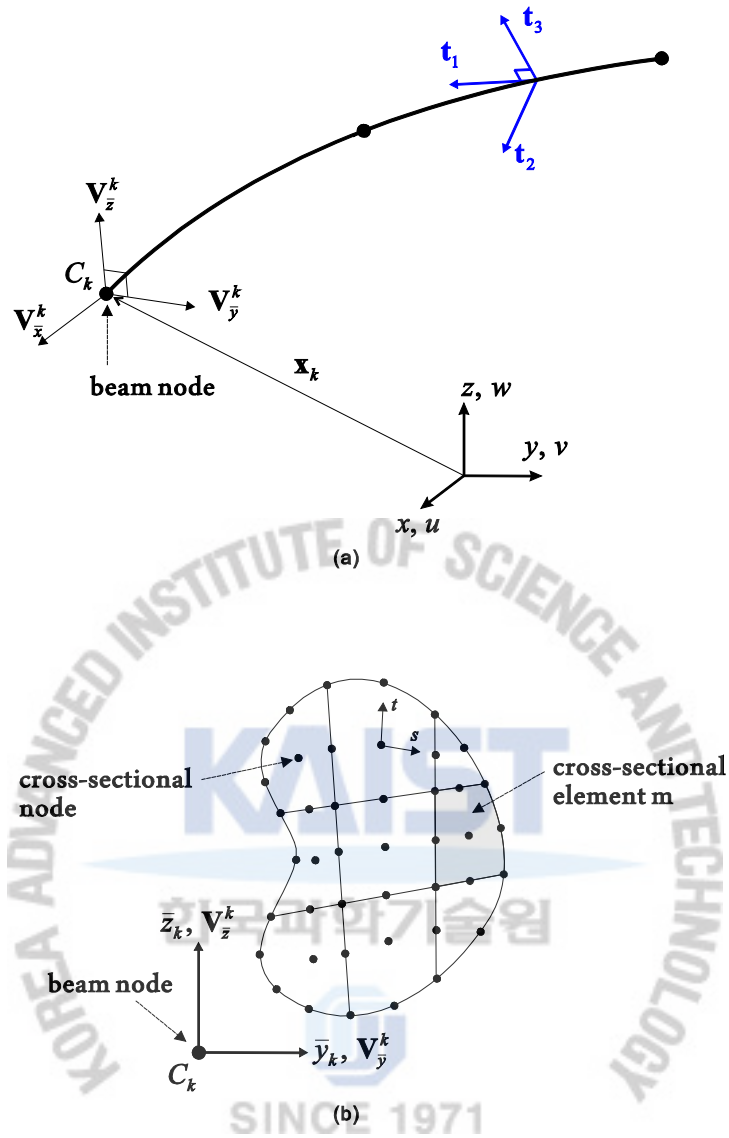


Figure 2-2. Continuum mechanics beam finite element with cross-sectional mesh. (a) 3-node beam finite element, (b) Cross-sectional mesh at beam node k .

2.1.1 Interpolation of Geometry

Starting with an arbitrary geometry of a beam discretized by 3-D solid finite elements, as shown in Fig. 2-1. The material fiber vector for solid element m in the global Cartesian coordinate system is given by

$${}^t \mathbf{x}^{(m)} = \sum_{i=1}^n h_i(r, s, t) {}^t \mathbf{x}_i^{(m)}, \quad (2-1)$$

where t is time parameter which characterizes the configuration, n is the total number of solid model nodes, $h_i(r, s, t)$ 3-D interpolation functions for the usual isoparametric procedure, and ${}^t \mathbf{x}_i^{(m)}$ are the coordinates of node i . Since the nodes of the solid model are aligned on the cross-sectional plane k , Eq. (2-1) can be divided into the multiplication of 1-D $h_k(r)$ and 2-D shape function $h_j(s, t)$,

$${}^t \mathbf{x}^{(m)} = \sum_{k=1}^q h_k(r) \sum_{j=1}^p h_j(s, t) {}^t \mathbf{x}_k^{j(m)}, \quad (2-2)$$

in which q is the number of the cross-sectional planes, p is the number of the nodes of the solid element m (shaded in Fig. 2-1) positioned at each cross-sectional plane and ${}^t \mathbf{x}_k^{j(m)}$ are the coordinate of the j th cross-sectional node in cross-sectional plane k corresponding to the solid element m . The assumption of Timoshenko beam theory can be enforced at all the cross-sectional nodes by

$${}^t \mathbf{x}_k^{j(m)} = {}^t \mathbf{x}_k + \bar{y}_k^{j(m)} {}^t \mathbf{V}_{\bar{y}}^k + \bar{z}_k^{j(m)} {}^t \mathbf{V}_{\bar{z}}^k, \quad (2-3)$$

where ${}^t \mathbf{x}_k$ are the position of origin at point C_k corresponding to the beam nodes, ${}^t \mathbf{V}_{\bar{y}}^k$ and ${}^t \mathbf{V}_{\bar{z}}^k$ are the orthogonal director vectors at cross-sectional plane k , and $\bar{y}_k^{j(m)}$ and $\bar{z}_k^{j(m)}$ represent the material position of the j th cross-sectional node of the solid element m in the cross-sectional Cartesian coordinate system described by the basis vectors ${}^t \mathbf{V}_{\bar{y}}^k$ and ${}^t \mathbf{V}_{\bar{z}}^k$. The vector relation in Eq. (2-3) is graphically represented in Figs. 2-1 and 2-2.

Applying Eq. (2-3) to Eq. (2-2), the material fiber vector of the continuum mechanics based beam finite elements corresponding to the solid element m at configuration t is obtained as

$${}^t \mathbf{x}^{(m)} = \sum_{k=1}^q h_k(r) {}^t \mathbf{x}_k + \sum_{k=1}^q h_k(r) \bar{y}_k^{(m)} {}^t \mathbf{V}_{\bar{y}}^k + \sum_{k=1}^q h_k(r) \bar{z}_k^{(m)} {}^t \mathbf{V}_{\bar{z}}^k \quad (2-4)$$

$$\text{with } \bar{y}_k^{(m)} = \sum_{j=1}^p h_j(s, t) \bar{y}_k^{j(m)}, \quad \bar{z}_k^{(m)} = \sum_{j=1}^p h_j(s, t) \bar{z}_k^{j(m)}, \quad (2-5)$$

where $\bar{y}_k^{(m)}$ and $\bar{z}_k^{(m)}$ denote the position in the cross-sectional Cartesian coordinate system in the cross-sectional plane k . Then, Eq. (2-4) becomes the position vector of the sub-beam m corresponding to the solid beam m . The continuum mechanics based beam finite element consists of the m number of sub-beams. It is important to know that Eq. (2-4) is the geometry interpolation of the solid element m aligned in the beam length direction in which the kinematic assumption of the Timoshenko beam theory is enforced.

Then, the point C_k corresponds to the k th beam node. The beam node at point C_k can be arbitrarily positioned on cross-sectional plane k defined by the two director vectors ${}^t \mathbf{V}_{\bar{y}}^k$ and ${}^t \mathbf{V}_{\bar{z}}^k$ in Fig. 2-1. The longitudinal reference line that is used to define the geometry of the beam is created by connecting the beam nodes. In this paper, it is important to know the difference between beam nodes and cross-sectional nodes, see Figs. 2-1 and 2-2.

As mentioned, the geometry interpolation of the beam element in Eq. (2-4) corresponds to the solid element m . The simple assemblage of the interpolation functions corresponding to all the solid elements aligned along the beam length direction represents the geometry interpolation of the whole beam element. As a result, the beam finite element shown in Fig. 2-2(a) can have a cross-sectional discretization in Fig. 2-2(b) at each beam node. The size and shape of the cross-sections can arbitrarily vary but the cross-sectional mesh pattern should be the same to maintain the continuity of the geometry on all the cross-sectional planes.

2.1.2 Interpolation of Displacement

From the interpolation of geometry in Eq. (2-4), the interpolation of displacements corresponding to the solid element m is derived as in [50]

$$\mathbf{u}^{(m)} = \sum_{k=1}^q h_k(r) \mathbf{u}_k + \sum_{k=1}^q h_k(r) \bar{y}_k^{(m)} \hat{\mathbf{R}}(\boldsymbol{\theta}^k)^0 \mathbf{V}_y^k + \sum_{k=1}^q h_k(r) \bar{z}_k^{(m)} \hat{\mathbf{R}}(\boldsymbol{\theta}^k)^0 \mathbf{V}_z^k \quad (2-6)$$

$$\text{with } \mathbf{u}_k = \begin{bmatrix} u_k \\ v_k \\ w_k \end{bmatrix}, \boldsymbol{\theta}^k = \begin{bmatrix} \theta_x^k \\ \theta_y^k \\ \theta_z^k \end{bmatrix} \text{ and } \hat{\mathbf{R}}(\boldsymbol{\theta}^k) = \begin{bmatrix} 0 & -\theta_z^k & \theta_y^k \\ \theta_z^k & 0 & -\theta_x^k \\ -\theta_y^k & \theta_x^k & 0 \end{bmatrix}, \quad (2-7)$$

where \mathbf{u}_k is the displacement vector of node k , $\boldsymbol{\theta}^k$ is the rotation vector of node k , and $\hat{\mathbf{R}}$ is skew-symmetric matrix operator.

Eq. (2-6) indicates that the displacement fields of all the solid elements that compose the whole beam is determined by the three translations and three rotations (six degrees of freedom) at each beam node because the nodes of the solid elements are placed on the cross-sectional planes and the kinematic assumption of the Timoshenko beam theory is enforced. Therefore, the assemblage of the solid elements can act like a single beam element and the beam element can have the cross-sectional discretization.

The basic displacement field in Eq. (2-6) can be enriched by adding various displacement patterns and then the generalized interpolation of displacements is obtained

$$\mathbf{u}_g^{(m)} = \mathbf{u}^{(m)} + \mathbf{u}_a^{(m)}, \quad (2-8)$$

in which $\mathbf{u}_a^{(m)}$ is the additional interpolation of displacements, which could include warping displacements, displacements for cross-sectional distortions and so on.

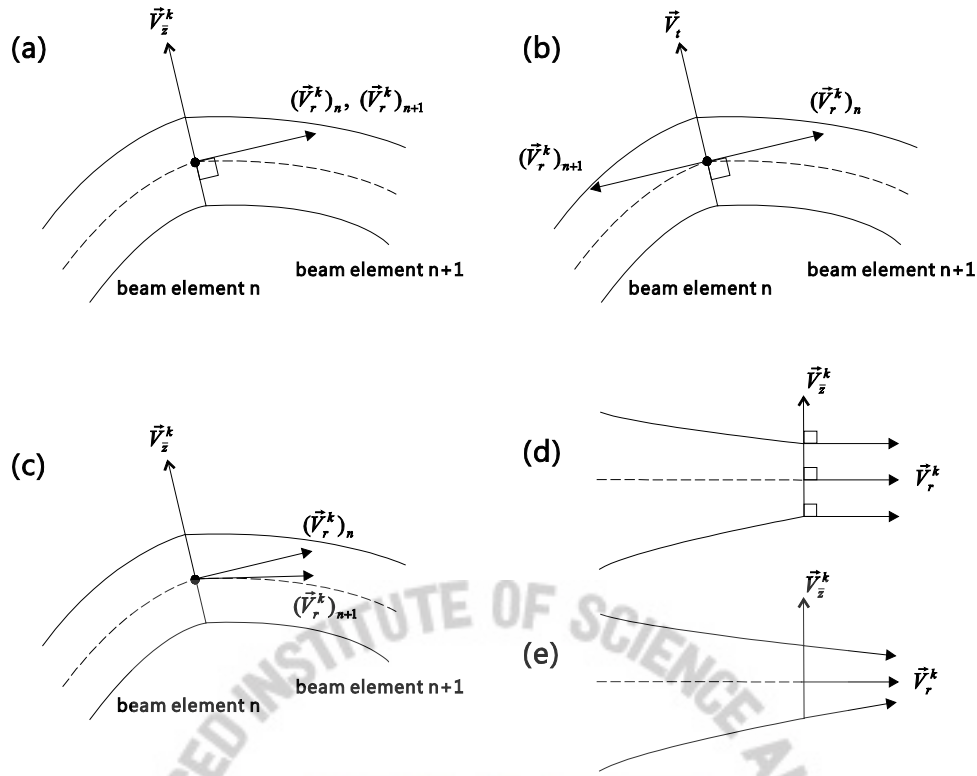


Figure 2-3. Directions of warping displacements. (a) and (b) Correct and wrong warping directions at a sharing node, (c) Warping direction same to the longitudinal direction of beam elements, (d) and (e) Uniform and varying warping directions at varying beam cross-sections.

2.1.3 Interpolation of Warping Displacement

In order to consider the warping displacements, we use the enriched displacements

$$\mathbf{u}_g^{(m)} = \mathbf{u}^{(m)} + \mathbf{u}_w^{(m)}, \quad (2-9)$$

$$\text{with } \mathbf{u}_w^{(m)} = \sum_{k=1}^q h_k(r) f_k^{(m)}(s, t) \mathbf{V}_x^k, \quad (2-10)$$

where $f_k^{j(m)}$ are the so-called warping function which obtained by solving St. Venant equations. \mathbf{V}_x^k is director vector normal to cross-sectional plane k and is defined by the director vectors \mathbf{V}_y^k and \mathbf{V}_z^k

$$\mathbf{V}_x^k = \mathbf{V}_y^k \times \mathbf{V}_z^k \quad \text{or} \quad \mathbf{V}_x^k = -\mathbf{V}_y^k \times \mathbf{V}_z^k. \quad (2-11)$$

The sign of the directions in Eq. (2-11) should be carefully chosen to enforce the continuity of the longitudinal displacements at beam nodes shared by beam elements. Figs. 2-3(a) and (b) show the correct and wrong warping directions, respectively.

Note that the numerical solutions depend on the directions of the warping displacements chosen. When varying cross-sections are considered, the warping directions we use correspond to Fig. 2-3(d). Figs. 2-3(c) and (e) show alternative choices of the warping directions, which are defined by the longitudinal direction of the beam elements, but the directions in Figs. 2-3(a) and (d) give better numerical results, in particular, when few beam elements are used. Some numerical results that show the effect of the warping direction will be presented in numerical studies.

Based on the cross-sectional discretization at beam node k in Fig. 2-2(b), we introduce the interpolation of warping displacements. The natural choice is to use

$$f_k^{(m)}(s,t) = \sum_{j=1}^p h_j(s,t) f_k^{j(m)}, \quad (2-12)$$

where $f_k^{j(m)}$ are warping degrees of freedom at beam node k corresponding to the solid element m . In this case, the total number of degrees of freedom for warping at each beam node is the same as the number of cross-sectional nodes on each cross-sectional plane. Therefore, Eq. (2-12) requires many additional warping degrees of freedom at beam nodes depending on the cross-sectional meshes used and the resulting element is similar to the beam element in [29].

In order to use only one additional degree of freedom for warping displacements at each beam node, we then use

$$f_k^{(m)}(s,t) = \sum_{j=1}^p h_j(s,t) f_k^{j(m)} \alpha_k, \quad (2-13)$$

in which α_k is the warping degree of freedom at beam node k and $f_k^{j(m)}$ is the pre-calculated warping values on cross-sectional plane k by solving St. Venant equations. Then, the continuum mechanics based beam finite element with cross-sectional discretization that allows for the warping effect has only seven degrees of freedom at each beam node. Through the warping degree of freedom α_k in Eq. (2-13), the inter-elemental continuity of the warping displacements is ensured since adjacent beam elements connect to the same beam node. Without considering the inter-elemental continuity, non-uniform warping behaviors along beam length due to non-uniform torsion or constrained warping conditions cannot be properly predicted.

Note that the interpolation of warping displacements in Eq. (2-12) does not require pre-calculation, that is, the warping is automatically considered in the beam formulation. However, a special treatment is required to remove redundant rigid body modes that occur due to the warping degrees of freedoms $f_k^{j(m)}$ [29].

2.2 Calculation of Warping Function

Here we present the procedure for calculating the warping values $f_k^{j(m)}$ in Eq. (2-13). The warping values are numerically calculated by solving St. Venant equations in the 2-D cross-sectional domain Ω_k with its boundary $\partial\Omega_k$ on cross-sectional plane k , see Fig. 2-4

$$\frac{\partial^2 \bar{f}_k}{\partial \bar{y}_k^2} + \frac{\partial^2 \bar{f}_k}{\partial \bar{z}_k^2} = 0 \quad \text{in } \Omega_k, \quad (2-14)$$

$$n_{\bar{y}}^k \frac{\partial \bar{f}_k}{\partial \bar{y}_k} + n_{\bar{z}}^k \frac{\partial \bar{f}_k}{\partial \bar{z}_k} = n_{\bar{y}}^k \bar{z}_k - n_{\bar{z}}^k \bar{y}_k \quad \text{on } \partial\Omega_k, \quad (2-15)$$

in which \bar{f}_k is the warping function defined in the cross-sectional Cartesian coordinate system with the point of origin C_k , and $n_{\bar{y}}^k$ and $n_{\bar{z}}^k$ are the components of the vector normal to the cross-sectional boundary $\partial\Omega_k$. Note that, in general, the position of origin C_k does not coincide with the center of twist of the cross-sectional plane.

St. Venant equations can be easily solved by the standard finite element formulation

$$\int_{\Omega_k} \left(\frac{\partial \bar{f}_k}{\partial \bar{y}_k} \frac{\partial \delta \bar{f}_k}{\partial \bar{y}_k} + \frac{\partial \bar{f}_k}{\partial \bar{z}_k} \frac{\partial \delta \bar{f}_k}{\partial \bar{z}_k} \right) d\Omega = \int_{\partial\Omega_k} (n_{\bar{y}}^k \bar{z}_k - n_{\bar{z}}^k \bar{y}_k) dS, \quad (2-16)$$

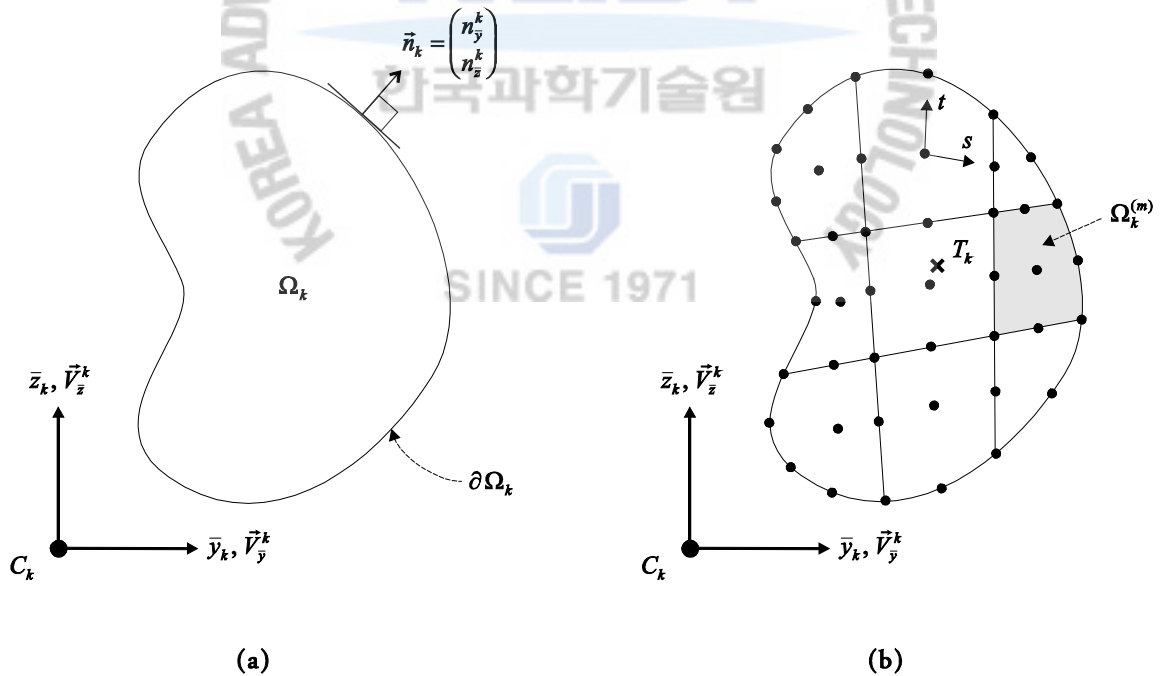


Figure 2-4. A cross-section to solve St. Venant equations. (a) Cross-sectional Cartesian coordinate system (point of origin C_k) and a vector normal to cross-sectional boundary, (b) Cross-sectional mesh and the center of twist T_k .

where $\delta \bar{f}_k$ is the variation of the warping function discretized by the same mesh as shown in Fig. 2-2(b) and the interpolation of warping in the cross-sectional element m (corresponding to the solid element m) is the same as in Eqs. (2-5), (2-12) and (2-13)

$$\bar{f}_k^{(m)} = \sum_{j=1}^p h_j(s,t) \bar{f}_k^{j(m)}, \quad (2-17)$$

where $\bar{f}_k^{j(m)}$ are the values of the warping function at cross-sectional nodes. Note that when we solve Eq. (2-16), one warping degree of freedom that is arbitrarily chosen should be prescribed to avoid the singularity of the system matrix obtained by Eq. (2-16).

If the origin of the cross-sectional Cartesian coordinate system C_k is moved, the boundary condition term in the right hand side of Eqs. (2-15) and (2-16) is changed. As a result, the solution of St. Venant equations (warping function $\bar{f}_k^{(m)}$) depends on where we position the origin of the cross-sectional Cartesian coordinate system.

The proper warping function $f_k^{(m)}$ is the solution calculated when the center of twist coincides with the origin of the cross-sectional Cartesian coordinate system because the beam cross-sections subjected to torsion rotate about the center of twist with the resulting warping. Therefore, the proper warping function ($f_k^{(m)}$) corresponding to the center of twist should be transformed from the warping function ($\bar{f}_k^{(m)}$) corresponding to the origin C_k ,

$$f_k^{(m)} = M(\bar{f}_k^{(m)}) + \bar{y}_k^T M(\bar{z}_k^{(m)}) - \bar{z}_k^T M(\bar{y}_k^{(m)})$$

with $M(g^{(m)}) = g^{(m)} - \frac{1}{A} \sum_{m=1}^d \int_{\Omega_k^{(m)}} g^{(m)} da$, (2-18)

where \bar{y}_k^T and \bar{z}_k^T represent the position of the center of twist T_k on cross-sectional plane k , $\Omega_k^{(m)}$ is the domain of the cross-sectional element m , d is the number of cross-sectional elements and A is the cross-sectional area $A = \sum_{m=1}^d \int_{\Omega_k^{(m)}} da$. This is the key step to reach an effective element formulation.

From the solution of the warping function ($\bar{f}_k^{(m)}$) corresponding to the origin C_k , the position of the center of twist in Eq. (2-18) can be calculated [18] by,

$$\bar{y}_k^T = \frac{I(\bar{f}_k^{(m)}, \bar{y}_k^{(m)})I(\bar{y}_k^{(m)}, \bar{z}_k^{(m)}) - I(\bar{f}_k^{(m)}, \bar{z}_k^{(m)})I(\bar{y}_k^{(m)}, \bar{y}_k^{(m)})}{I(\bar{y}_k^{(m)}, \bar{y}_k^{(m)})I(\bar{z}_k^{(m)}, \bar{z}_k^{(m)}) - I^2(\bar{y}_k^{(m)}, \bar{z}_k^{(m)})},$$

$$\bar{z}_k^T = \frac{I(\bar{f}_k^{(m)}, \bar{y}_k^{(m)})I(\bar{z}_k^{(m)}, \bar{z}_k^{(m)}) - I(\bar{f}_k^{(m)}, \bar{z}_k^{(m)})I(\bar{y}_k^{(m)}, \bar{z}_k^{(m)})}{I(\bar{y}_k^{(m)}, \bar{y}_k^{(m)})I(\bar{z}_k^{(m)}, \bar{z}_k^{(m)}) - I^2(\bar{y}_k^{(m)}, \bar{z}_k^{(m)})}, \quad (2-19)$$

in which an integration operator I is defined by

$$I(g_1^{(m)}, g_2^{(m)}) = \sum_{m=1}^d \int_{\Omega_k^{(m)}} [M(g_1^{(m)})M(g_2^{(m)})] da. \quad (2-20)$$

All the integrations in Eqs. (2-18), (2-19) and (2-20) are numerically calculated.

It is important to note that, although the calculated center of twist is the approximated one for the actual beam cross-section, it is the exact center of twist for the discretized beam cross-section; that is, when torsion is applied at the center of twist in the discretized beam cross-section, no transverse displacements occur.

2.3 Numerical Integration

With the interpolations of the geometry and the displacements given, the procedure to construct the strain-displacement matrix, the stiffness matrix and the load vector is standard as in Ref. [3].

When the width and height of a beam cross-section are small compared to the beam length, the beam finite element locks, that is, the element is too stiff in bending. However, the locking can be easily removed using a mixed formulation that is effectively implemented by using reduced integration corresponding to the r -direction [3]. We use this procedure in our implementation.

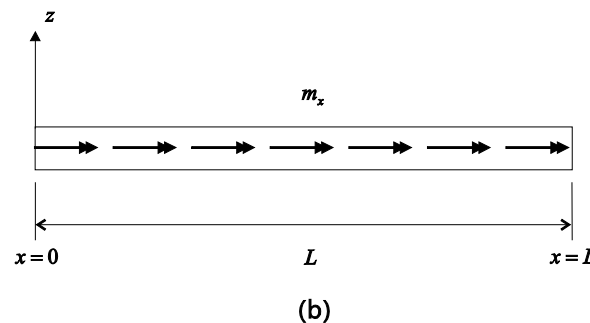
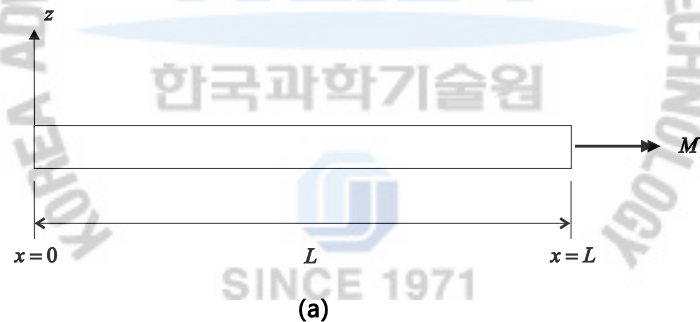


Figure 2-5. Straight cantilever beam problems (a) Uniform torsion problem (a straight beam subjected to torsional moment at the free tip) (b) Non-uniform torsion problem (a straight beam subjected to uniformly distributed torsional moment).

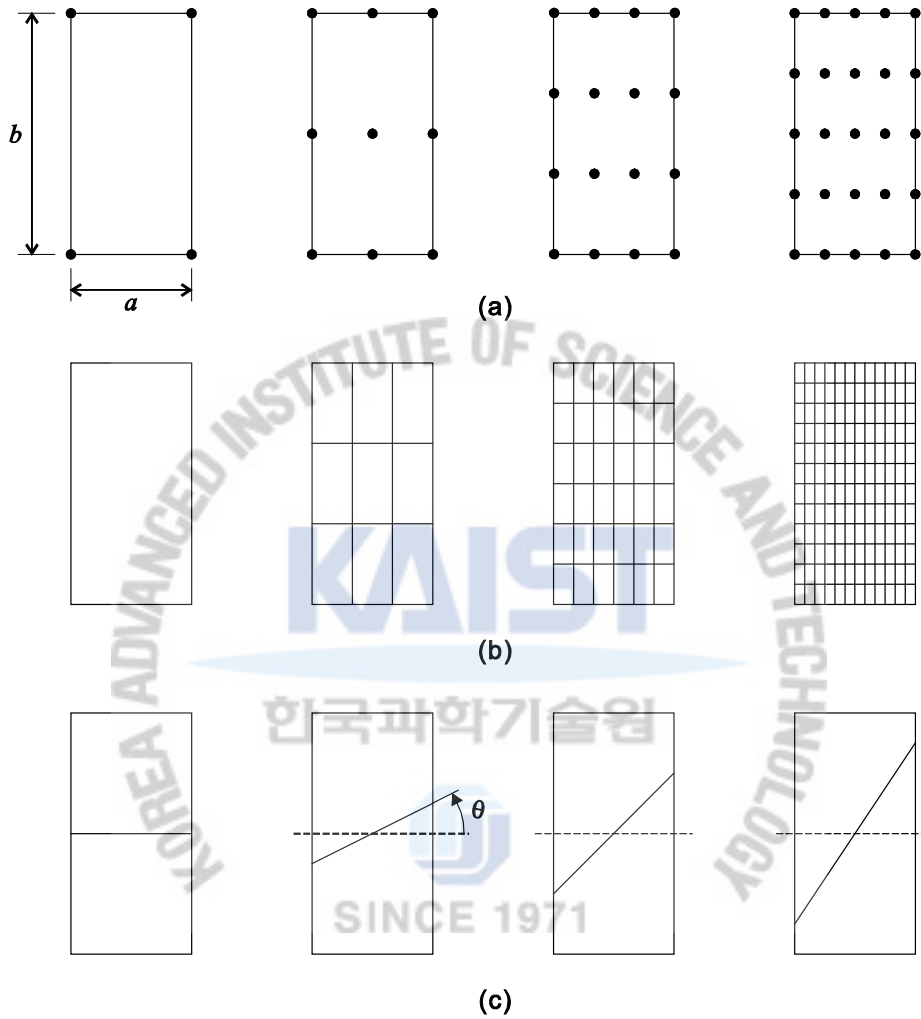


Figure 2-6. Various cross-sectional discretizations with different interpolation functions and meshes. (a) Single element meshes (1st, 2nd, 3rd and 4th order interpolations), (b) 1x1, 3x3, 6x6 and 12x12 linear meshes, (c) Distorted meshes ($\tan \theta = 0, b/4a, 2b/4a$ and $3b/4a$) of 16-node cross-sectional elements.

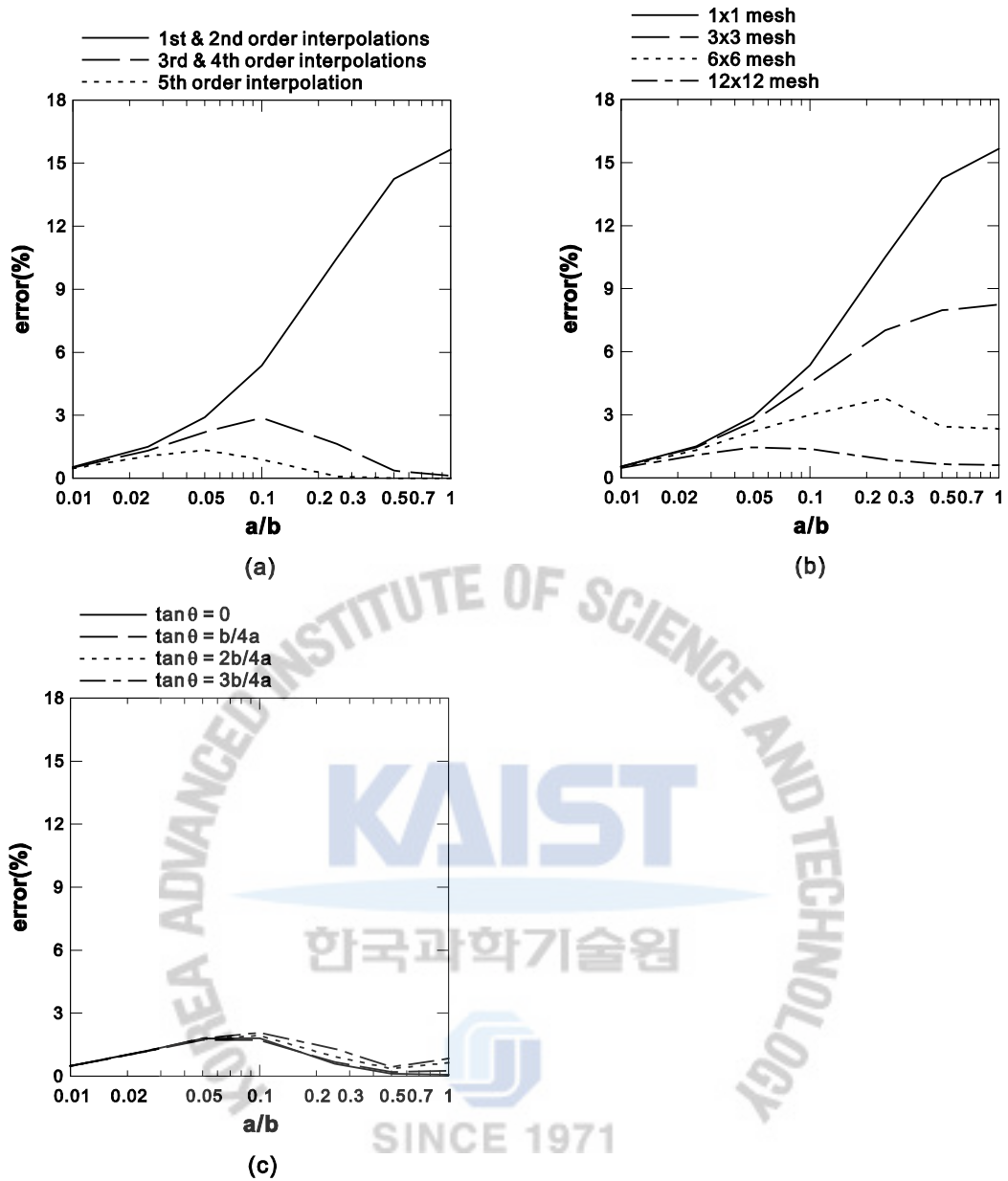


Figure 2-7. Relative errors in angle of twist at the loaded tip for various aspect ratios (a/b); (a) Corresponding to the interpolation orders in Fig. 2-6(a); (b) Corresponding to the meshes of linear cross-sectional elements in Fig. 2-6(b); (c) Corresponding to the distorted cross-sectional meshes in Fig.2-6(c).

2.4 Numerical Studies

To verify the proposed formulation and to study the twisting behavior of the beam element depending on geometries, boundary conditions and cross-sectional meshes, we perform various numerical analyses using our beam elements. The results are compared with available analytical solutions and solutions of equivalent finite

element models. Young's modulus $E = 2.0 \times 10^{11} \text{ N/m}^2$ and Poisson's ratio $\nu = 0$ are used for all the beam problems considered in this section.

2.4.1 Rectangular cross-section beam problems

A straight cantilever beam of $L = 20\text{m}$ with a rectangular cross-section is subjected to torsional moment $M_x = 1.0\text{N} \cdot \text{m}$ at the center of twist at the free tip ($x = L$) as shown in Fig. 2-5(a). Then, uniform torsion occurs on all the beam cross-sections. Various aspect ratios of width to height (a/b) are considered for the rectangular cross-section, see Fig. 2-6. Warping is free at both ends and along the beam length. The boundary condition is given as

$$u = v = w = \theta_x = \theta_y = \theta_z = 0 \quad \text{at } x = 0. \quad (2-21)$$

We model the problem with the proposed single 2-node beam finite element, and various cross-sectional discretizations shown in Fig. 2-6 are tested. It is very important to note that in uniform torsion problems of prismatic beams with free warping, the same solutions are obtained regardless of the number of beam elements and the order of beam elements used.

The angles of twist in these numerical calculations mainly depend on the cross-sectional mesh used. In Fig 2-7, we plot the errors in the angle of twist at the loaded tip. The error is calculated by comparing the numerical approximations to the converged solutions obtained by the 50x50 mesh of 16-node cross-sectional elements because the analytical solutions in [1] do not have enough effective digits. Table 2-1 shows the analytical solutions by Timoshenko and the reference solutions used.

Table 2-1. Reference values used for angles of twist at the loaded tips for rectangular cross-section beam problems with free warping

a/b	Timoshenko	50x50 mesh of 16-node cross-sectional elements
0.01	3.75E-05	3.7645E-05
0.1	4.01E-08	3.9954E-08
0.25	2.85E-09	2.8445E-09
0.5	4.37E-10	4.3690E-10
1.0	8.89E-11	8.8912E-11

² In order to avoid difficulties in specifying the boundary conditions of equivalent shell and solid finite element models, zero Poisson's ratio is used.

Fig. 2-7(a) shows the errors according to the order of finite elements used to model the cross-section corresponding to the meshes in Fig. 2-5(a). It is very interesting to note that the 1st and 2nd order interpolations (4-node and 9-node cross-sectional elements) and the 3rd and 4th order interpolations (16-node and 25-node cross-sectional elements) give the identical results, respectively. It can be expected that the warping functions of rectangular cross-sections have the characteristics of odd functions. When a single 16-node cross-sectional element is used, the error is less than 3% in the whole range of the aspect ratio a/b . The solutions are also very accurate in two extreme cases: the square cross-section ($a/b = 1$) and the thin cross-section ($a/b \ll 1$). A more accurate solution by a single 36-node cross-sectional element (5th order interpolation) is also presented.

Fig. 2-7(b) shows the error in the angle of twist when 1x1, 3x3, 6x6 and 12x12 meshes of 4-node cross-sectional elements in Fig. 2-6(b) are used. The linear element gives good accuracy for the thin cross-section case. While, as the mesh is refined, the error decreases in the whole range of a/b , the solutions of the 12x12 mesh of the linear elements are not better than those of a single 36-node cross-sectional element.

Through the two tests, we can conclude that the use of higher order cross-sectional elements is more effective than use of many lower order cross-sectional elements. The use of the 16-node elements for cross-sectional discretizations gives reasonable accuracy for general engineering purposes.

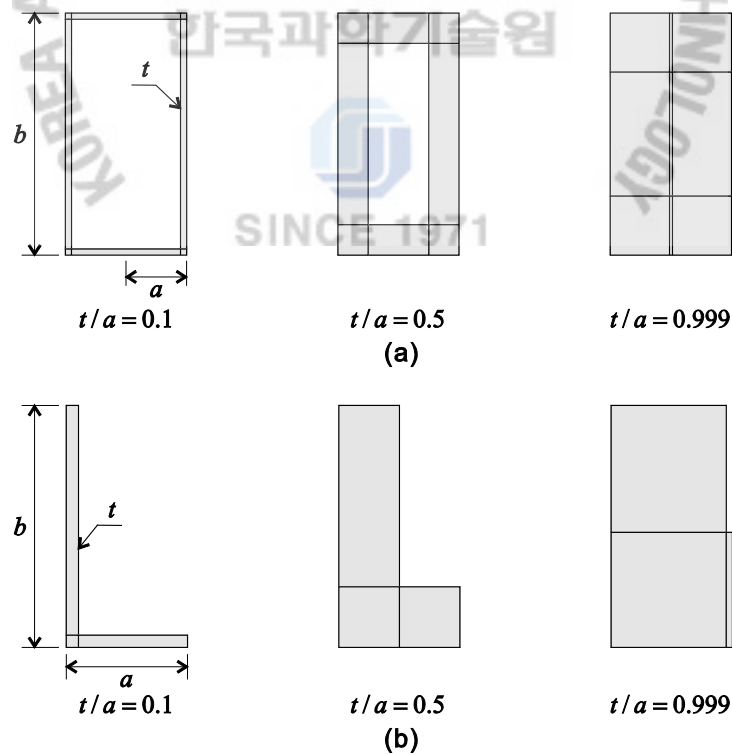


Figure 2-8. Tubular and angle cross-sections with various thicknesses and cross-sectional meshes used. (a) Tubular cross-sections ($a = 0.5$, $b = 2$), (b) Angle cross-sections ($a = 1$, $b = 2$).

In general, thin-walled beams are composed of several thin plates that have a ratio $a/b < 0.1$, and the graphs in Fig. 2-7(a) show that the 4-node cross-sectional element gives 5% and 9% errors for $a/b = 0.1$ and $a/b = 0.2$, respectively. The use of one 4-node cross-sectional element for each plate section of thin-walled beams gives solutions accurate enough for engineering practices.

Additionally, Fig. 2-7(c) reveals that the effect of mesh distortion on error in the angle of twist is not considerable when 16-node cross-sectional elements are used.

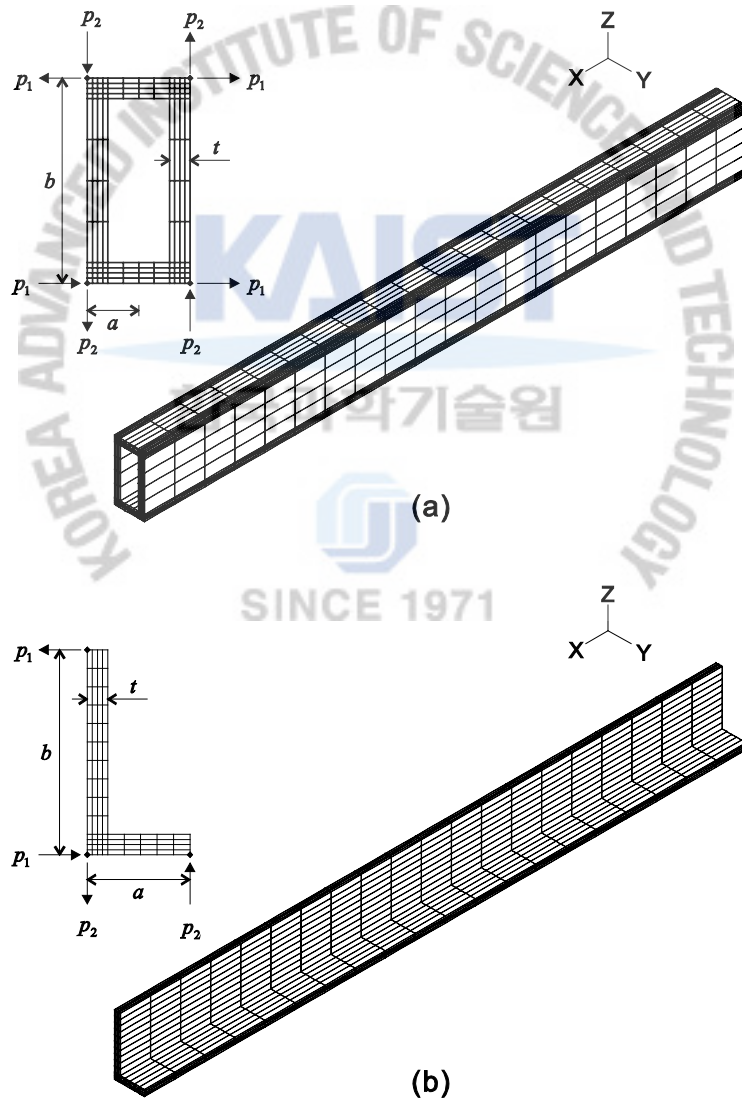


Figure 2-9. Solid element models and meshes used. (a) Tubular cross-section beam with 128x20 meshes of 27-node solid elements ($p_1 = 0.125N$, $p_2 = 0.25N$), (b) Angle cross-section beam with 76x20 meshes of 27-node solid elements ($p_1 = 0.0125N/m$, $p_2 = 0.025N/m$).

2.4.2 Tubular and angle cross-section beam problems

Considering the tubular and angle cross-sections in Fig. 2-8, we analyze the straight cantilever beam problem of length $L = 20$ in Fig. 2-5. Torsional moment $M_x = 1.0N \cdot m$ is applied at the center of twist at $x = L$ for the tubular cross-section problems as in Fig. 2-5(a) and uniformly distributed torsional moment $m_x = 1.0N \cdot m/m$ is applied at the center of twist along the beam length for the angle cross-section problems as in Fig. 2-5(b). For both problems, the warping of the beam is constrained at the fixed end

$$u = v = w = \theta_x = \theta_y = \theta_z = \alpha = 0 \quad \text{at } x = 0. \quad (2-22)$$

As shown in Fig. 2-8, for both cross-sections, the cross-sectional dimensions a and b are fixed and three different thicknesses ($t/a = 0.1, 0.5$ and 0.999) are considered. As the ratio t/a goes to 1.0 , the cross-sections get closer to a rectangular cross-section. Each tubular cross-section is modeled by eight cross-sectional elements and each angle cross-section is modeled by three cross-sectional elements, see Fig. 2-8.

Reference solutions are calculated by the 27-node solid element models in Fig. 2-9. Note that the solid element solutions depend on how we apply the torsional moment on the solid element models. A special point in the modeling is that the torsional moments need to be imposed appropriately. We assign the loads described in Fig. 2-9, where

$$l_i \cdot p_i = M_i = \frac{K_i}{K_t} M \quad (2-23)$$

Here, p_i is the point load exerting a couple-moment M_i on plate section i , l_i is the length of the plate section i , K_i and K_t are the torsional stiffness of the plate section i and the complete cross-section, respectively, and M is the total twisting moment applied. The tubular and angle cross-sections in Fig. 2-9 consist of 4- and 2-plate sections, respectively. In order to approximate K_i and K_t , we use the formulas available for thin-walled cross-section beams under free warping [1]. The same rule is used for thick-walled cross-section cases.

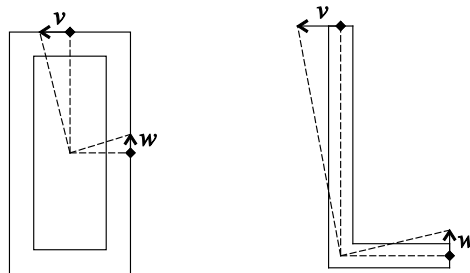


Figure 2-10. Method to measure angles of twist in the solid element models of the tubular and angle cross-section beams.

Fig. 2-10 shows the method used to measure the angles of twist in the solid element models of the tubular and angle cross-section beam problems. The angles calculated from translational displacements at two sampling points as shown in Fig. 2-10 are averaged.

Tables 2-2 and 2-3 present the numerical results for the tubular cross-section beam problems under uniform torsion in the three different thickness cases. The use of 16-node cross-sectional elements gives good agreement with the reference solutions in all the thickness cases. Tables 2-4 and 2-5 show a similar investigation for the angle cross-section beam problems under non-uniform torsion. For both beam problems, two 2-node beam elements and one 3-node beam element give solutions accurate enough for engineering practice.

Table 2-2. Angles of twist at the loaded tips for tubular cross-section beam problems under uniform torsion with constrained warping. Eight 16-node cross-sectional elements are used and N denotes the number of beam elements used.

N	$t/a = 0.1$		$t/a = 0.5$		$t/a = 0.999$	
	2-node beam	3-node beam	2-node beam	3-node beam	2-node beam	3-node beam
1	1.6480E-09	1.6466E-09	5.1020E-10	5.0960E-10	4.3824E-10	4.3751E-10
2	1.6459E-09	1.6414E-09	5.0930E-10	5.0756E-10	4.3717E-10	4.3525E-10
4	1.6400E-09	1.6377E-09	5.0707E-10	5.0643E-10	4.3479E-10	4.3430E-10
8	1.6376E-09	1.6376E-09	5.0642E-10	5.0642E-10	4.3430E-10	4.3430E-10
16	1.6376E-09	1.6376E-09	5.0642E-10	5.0642E-10	4.3430E-10	4.3430E-10
Ref.	1.6023E-09		5.0121E-10		4.3053E-10	

Table 2-3. Angles of twist at the loaded tips for tubular cross-section beam problems under uniform torsion with constrained warping. Eight 2-node beam elements are used ($N = 8$).

Cross-sectional elements used	$t/a = 0.1$	$t/a = 0.5$	$t/a = 0.999$
1st order (4-node ele.)	1.6269E-09	4.8751E-10	4.0053E-10
2nd order (9-node ele.)	1.6288E-09	4.9997E-10	4.3047E-10
3rd order (16-node ele.)	1.6376E-09	5.0642E-10	4.3430E-10
Ref.	1.6023E-09	5.0121E-10	4.3053E-10

Table 2-4. Angles of twist at the loaded tips for angle cross-section beam problems under non-uniform torsion with constrained warping. Three 16-node cross-sectional elements are used and N denotes the number of beam elements used.

N	$t/a = 0.1$		$t/a = 0.5$		$t/a = 0.999$	
	2-node beam	3-node beam	2-node beam	3-node beam	2-node beam	3-node beam
1	1.0220E-07	1.0065E-07	1.0287E-09	1.0196E-09	2.1845E-10	2.1779E-10
2	9.9214E-08	9.7687E-08	1.0110E-09	9.9918E-10	2.1716E-10	2.1602E-10
4	9.6044E-08	9.6469E-08	9.8671E-10	9.8918E-10	2.1479E-10	2.1486E-10
8	9.5940E-08	9.6073E-08	9.8484E-10	9.8594E-10	2.1437E-10	2.1449E-10
16	9.5940E-08	9.5973E-08	9.8484E-10	9.8511E-10	2.1437E-10	2.1440E-10
Ref.	9.7160E-08		1.0008E-09		2.1629E-10	

Table 2-5. Angles of twist at the loaded tips for angle cross-section beam problems under non-uniform torsion with constrained warping. Eight 2-node beam elements are used ($N = 8$).

Cross-sectional elements used	$t/a = 0.1$	$t/a = 0.5$	$t/a = 0.999$
1st order (4-node ele.)	9.3925E-08	8.5206E-10	1.8475E-10
2nd order (9-node ele.)	9.5601E-08	9.5350E-10	2.0308E-10
3rd order (16-node ele.)	9.5940E-08	9.8484E-10	2.1437E-10
Reference solutions	9.7160E-08	1.0008E-09	2.1629E-10

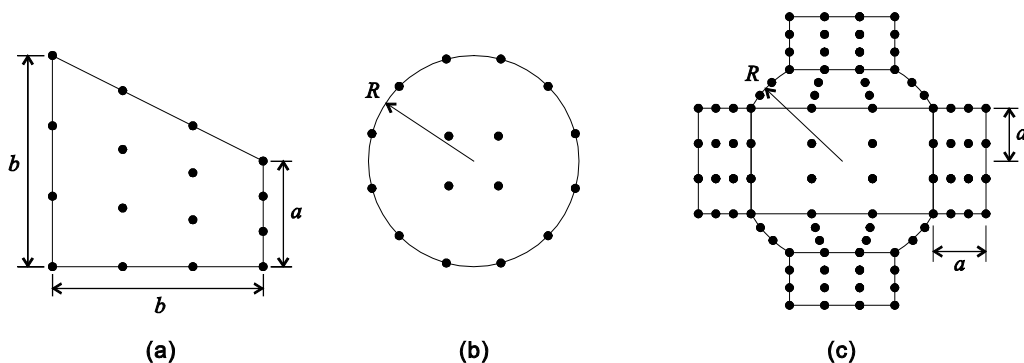


Figure 2-11. Cross-sectional discretizations of various solid cross-sections modeled on the yz -plane. (a) Trapezoidal cross-section modeled by a single 16-node cross-sectional element ($a = 2$, $b = 4$), (b) Circular cross-section modeled by a single 16-node cross-sectional element ($R = 2$), (c) Solid cross-section with four splines modeled by seven 16-node cross-sectional elements ($R = 2$, $a = 1$).

Table 2-6. Angles of twist at the loaded tip for various solid cross-section beam problems.

Cross-section	1st order (4-node cross-sectional el.)	2nd order (9-node cross-sectional ele.)	3rd order (16-node cross-sectional ele.)	Reference solutions
Trapezoidal	8.3158E-12	9.1001E-12	1.0845E-11	1.0632E-11
Circular	1.8750E-11	8.1482E-12	7.9401E-12	7.9578E-12
Spline	4.2236E-12	4.3103E-12	4.6444E-12	4.2890E-12

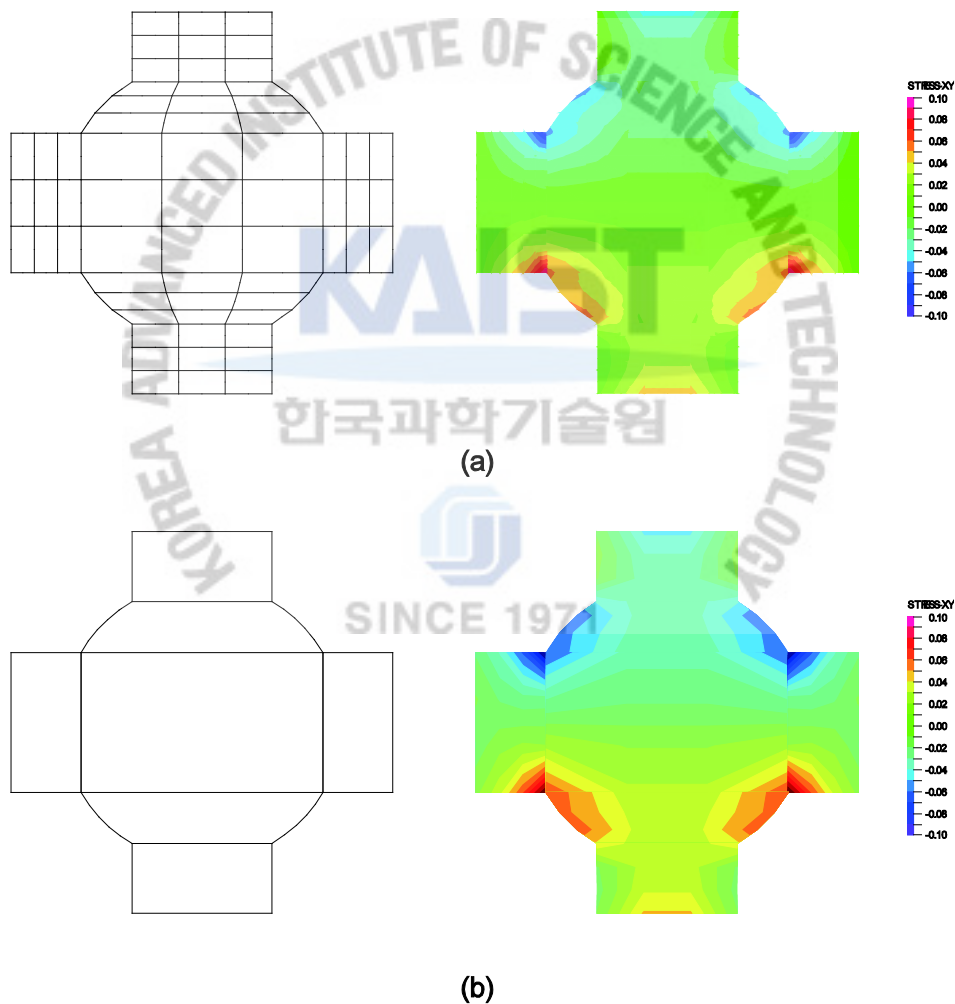


Figure 2-12. Distributions of transverse shear stress-xy in the solid cross-section with four splines. (Left: cross-sectional meshes used, Right: stress distribution) (a) Solid element solution calculated by 630 27-node solid elements. 63 and 10 solid elements are used on cross-sections and in beam length, respectively. (b) Beam element solution calculated by three beam elements. Seven 16-node cross-sectional elements are used.

2.4.3 Various solid cross-section beam problems

Let us consider straight beam problems with three different solid cross-sections (trapezoidal, circular and spline cross-sections) in Fig. 2-11. The beam length is $L = 20$, the boundary condition for free warping are used as in Eq. (2-21) and the torsional moment $M_x = 1.0N \cdot m$ is applied at the center of twist at $x = L$ as shown in Fig. 2-5(a). A single cross-sectional element is used for the trapezoidal and circular cross-sections and seven cross-sectional elements are used for the spline cross-section. In the beam length direction, a single 2-node beam element is used. Reference solutions are obtained from [5].

The results in Table 2-6 suggest that the single 16-node cross-sectional element gives good accuracy for the trapezoidal and circular sections. For the cross-section with four splines, more cross-sectional elements will give better results. To this point, we overall conclude that the 16-node cross-sectional element with the 3rd order interpolation function is effective in general cross-section cases including thin- and thick-walled cross-sections.

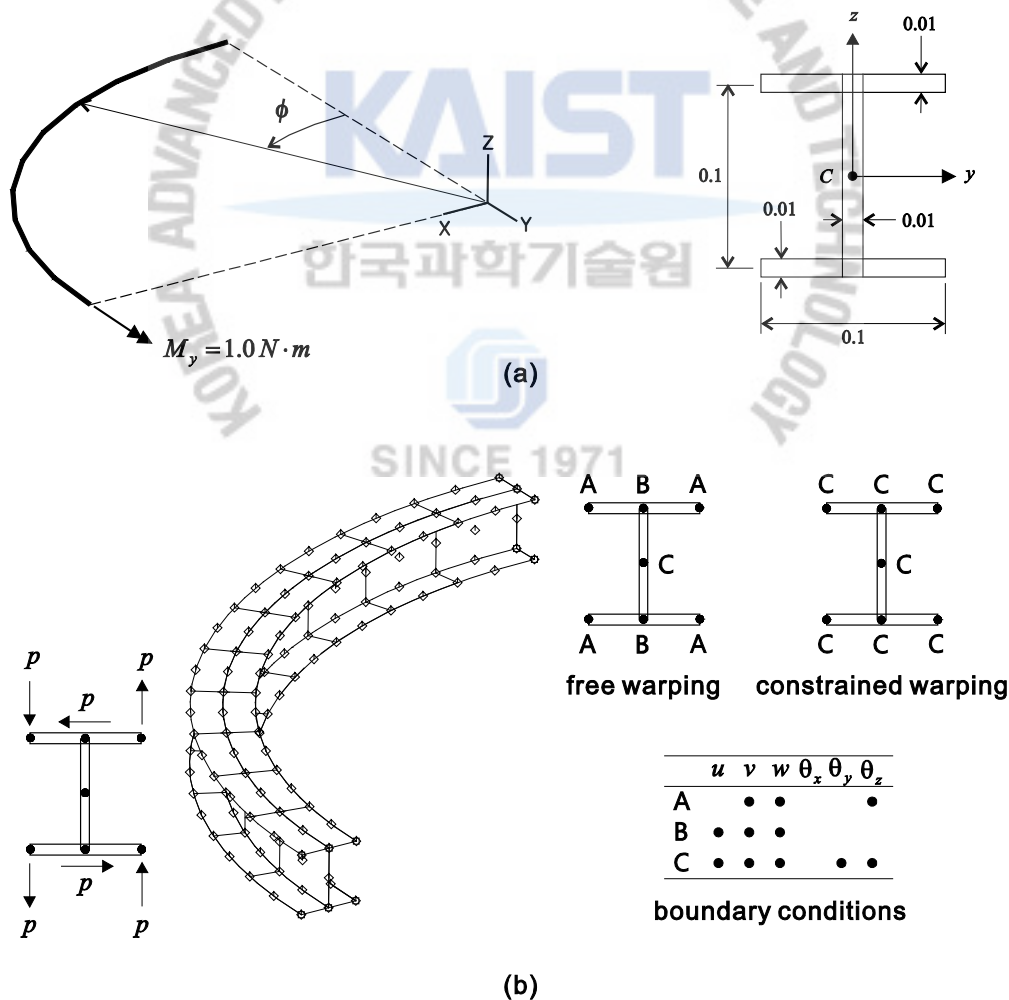


Figure 2-13. Curved wide flange cross-section beam problems. (a) Geometry of the curved wide flange cross-section beam problem and cross-sectional mesh used, (b) Shell finite element models used.

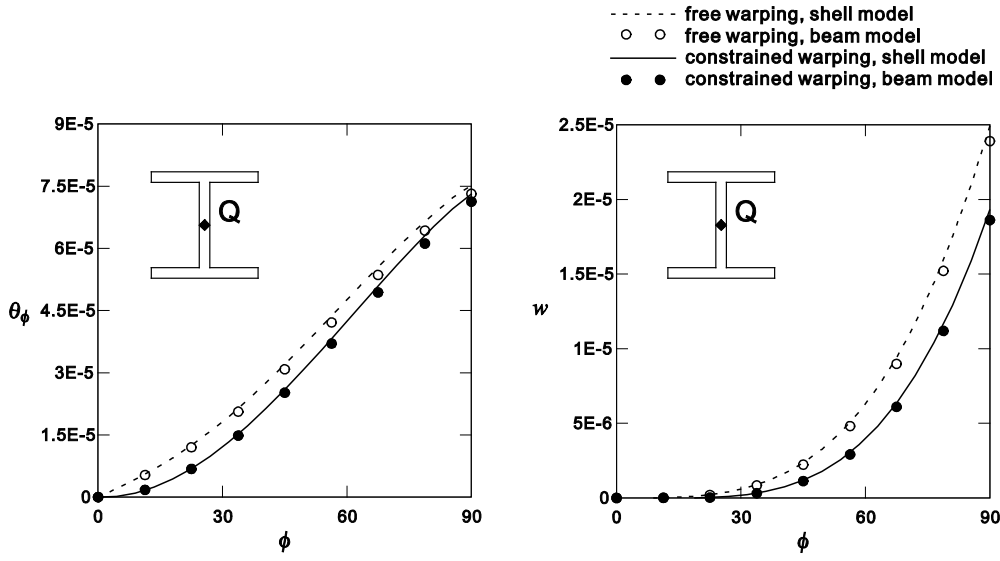


Figure 2-14. Angle of twist and displacement w along the beam length in the curved wide flange cross-section beam problems.

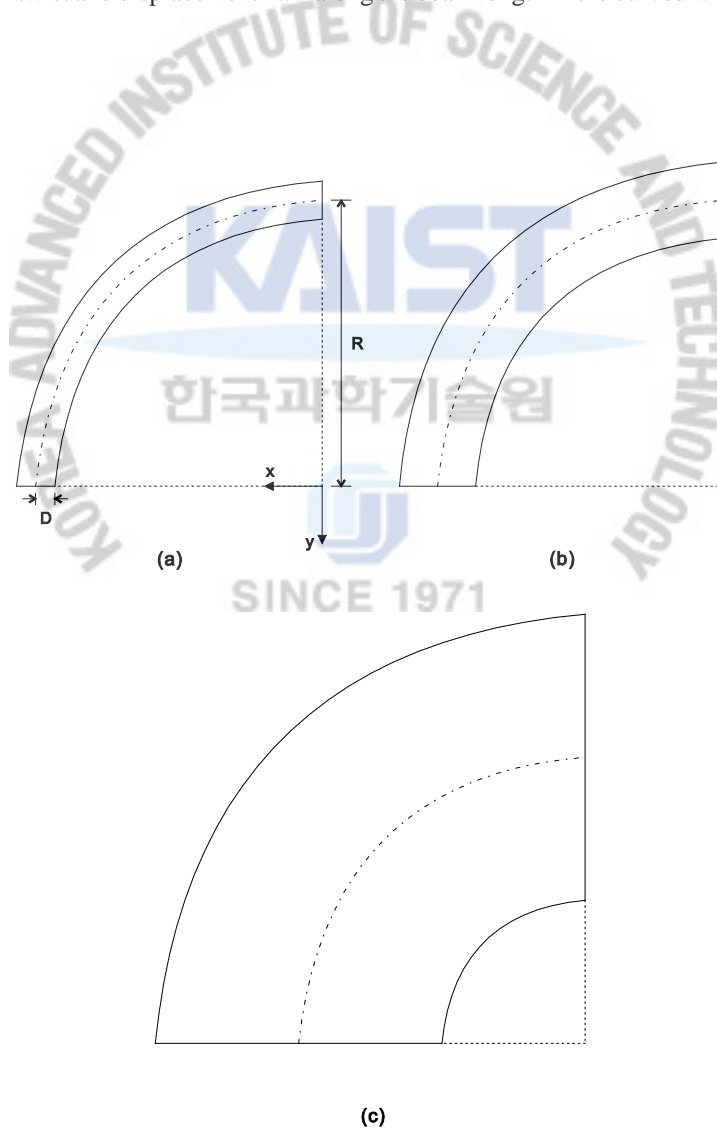


Figure 2-15. Curved wide flange cross-section beam problems with three different D/R . (a) $D/R = 0.1$, (b) $D/R = 0.2$, (c) $D/R = 0.5$.

Additionally, we analyze the spline cross-section beam problem with constrained warping by using three beam elements with seven 16-node cross-sectional elements. The boundary condition in Eq. (2-22) is used. The results are compared with the solutions of the solid element model with 630 27-node solid elements. Fig. 2-12 shows the distributions of transverse shear stress- xy on the cross-sectional plane at $x = L/2$. The angles of twist calculated at the loaded tips are 4.6051E-12 and 4.5968E-12 for the solid and beam element models, respectively.

2.4.4 Curved wide flange cross-section beam problems

We consider the curved wide flange cross-section beam problems shown in Fig. 2-13. The geometry of the beam is a quarter arc. The boundary conditions at $\varphi = 0^\circ$ are $u = v = w = \theta_x = \theta_y = \theta_z = 0$ for free warping and $u = v = w = \theta_x = \theta_y = \theta_z = \alpha = 0$ for constrained warping. The beam is subjected to the torsional moment $M_y = 1.0N \cdot m$ at the tip ($\varphi = 90^\circ$). We use seven 16-node cross-sectional elements for the wide flange cross-section as shown in Fig. 2-13(a).

Table 2-7. Angles of twist and displacement w at the loaded tip for the curved wide flange cross-section beam problems according to the warping direction used. Four 2-node beam elements ($N = 4$) and 16-node cross-sectional elements are used.

Warping direction	Free warping		Constrained warping	
	Angle of twist	w	Angle of twist	w
Fig. 3(a)	7.5199E-05	2.3273E-05	7.3136E-05	1.7909E-05
Fig. 3(c)	7.2384E-05	2.2232E-05	7.0503E-05	1.7233E-05
Ref.	7.5220E-05	2.4925E-05	7.3547E-05	1.9020E-05

Table 2-8. Angles of twist and displacement w at the loaded tip for the curved wide flange cross-section beam problems with constrained warping according to D/R . 16-node cross-sectional elements are used and N denotes the number of beam elements used.

D/R	Angle of twist			w		
	$N = 4$	$N = 8$	Ref.	$N = 4$	$N = 8$	Ref.
0.1	7.1272E-05	7.1265E-05	7.3547E-05	1.8613E-05	1.8599E-05	1.9020E-05
0.2	1.5101E-05	1.5102E-05	1.8024E-05	4.0321E-06	4.0296E-06	4.2771E-06
0.5	2.4656E-07	2.4659E-07	3.9216E-06	6.1726E-08	6.1694E-08	6.1724E-08

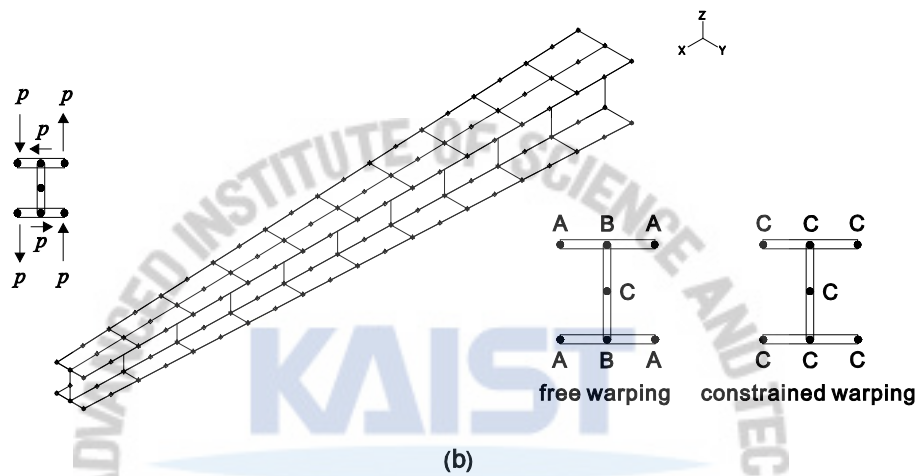
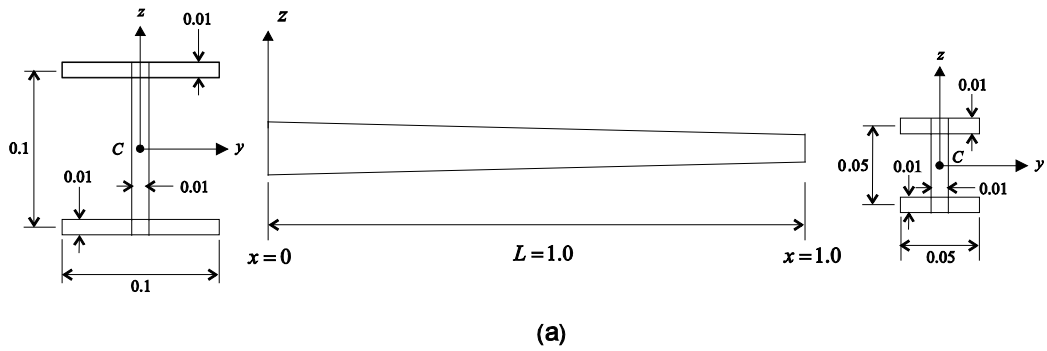


Figure 2-16. Varying wide flange cross-section beam problems. (a) Geometry of the varying wide flange cross-section beam problem and cross-sectional mesh used, (b) Shell finite element models used.

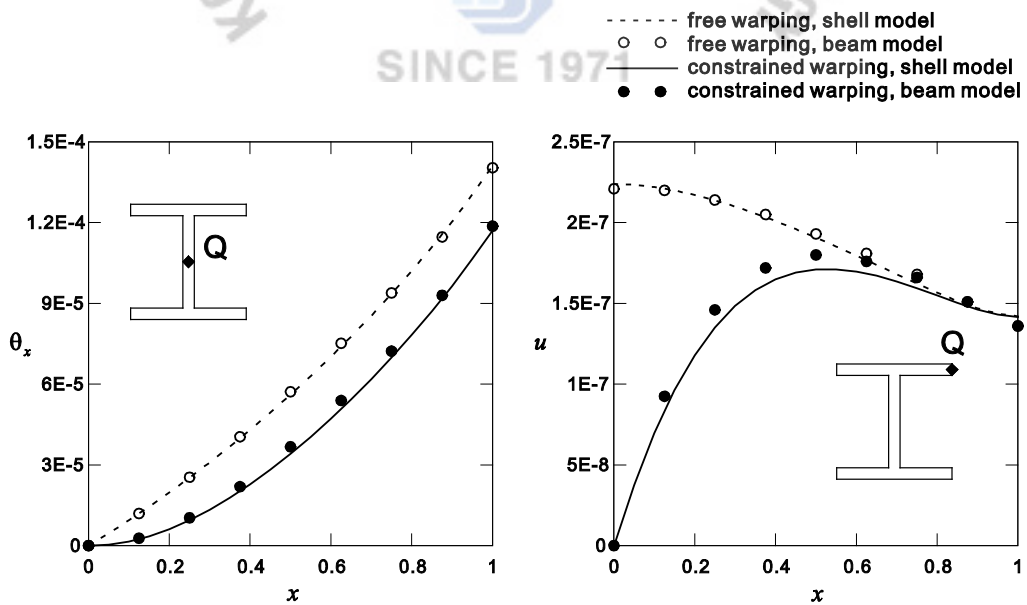


Figure 2-17. Angle of twist and displacement u along the beam length in the varying wide flange cross-section beam problems.

Since the beam problems have thin-walled cross-sections, shell finite element solutions are used as references. Fig. 2-13(b) shows the shell finite element model including the mesh, the boundary conditions for free and constrained warping and the external loading equivalent to the beam problem. For each plate, ten MITC9 shell elements are used along the beam length. In the figure, the point load is $p = 10/3N$ and A, B and C denote the boundary conditions used. Note that to obtain a proper beam model for free warping, special attention needs to be carefully given. The angles of twist for the reference solutions are obtained from the rotation degrees of freedom of the shell elements.

Fig. 2-14 shows the distributions of the angle of twist and displacement w along the beam length corresponding to the point Q when four 3-node beam elements are used. Although the torsional moment is applied at the free tip, it is very hard to accurately calculate the response of this beam problem without considering the warping effect coupled with bending, shearing and stretching. Note that in the thin-walled cross-section beam problems, the results calculated by 4-node or 9-node cross-sectional elements are almost the same.

In the beam problems, we test the effect of the warping direction used. Table 2-7 shows the numerical results when the warping directions in Figs. 2-3(a) and (c) are used. To clearly investigate the effect, four 2-node elements are used. The warping direction in Fig. 2-3(a) gives better results. However, when the number of the beam elements used increases or higher order beam elements are used, the difference becomes smaller.

Table 2-8 shows the numerical results depending on D/R defined in Fig. 2-15. As D/R increases (that is, the beam becomes deeper), the angles of twist calculated shows a bigger difference from the reference solutions because the effect of local deformation that cannot be captured by our beam element becomes more dominant.

Table 2-9. Angles of twist at the loaded tips for the varying wide flange cross-section beam problems under uniform torsion. Four 3-node beam elements are used ($N = 4$).

$\tan 0.5\theta$	Free warping		Constrained warping	
	Present study	Ref.	Present study	Ref.
0.025	1.3771E-04	1.40641E-04	1.1454E-04	1.16549E-04
0.095	8.5779E-05	8.74165E-05	5.9483E-05	6.01527E-05
0.225	3.8829E-05	3.86123E-05	2.0123E-05	1.91705E-05
0.475	2.0648E-05	1.87122E-05	8.2445E-06	7.11663E-06

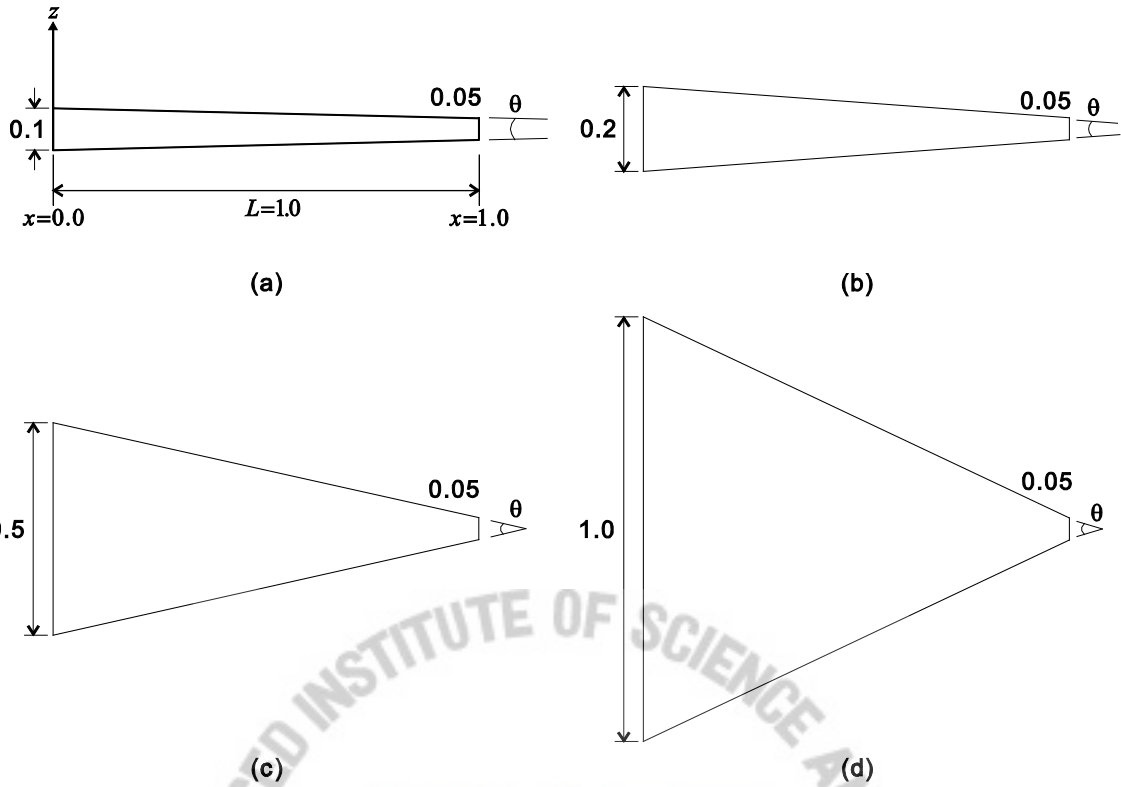


Figure 2-18. Varying wide flange cross-section beam problems with four different tapering degrees. (a) $\tan 0.5\theta = 0.025$ ($\theta = 2.864$ deg.), (b) $\tan 0.5\theta = 0.095$ ($\theta = 10.854$ deg.), (c) $\tan 0.5\theta = 0.225$ ($\theta = 25.361$ deg.), (d) $\tan 0.5\theta = 0.475$ ($\theta = 50.815$ deg.).

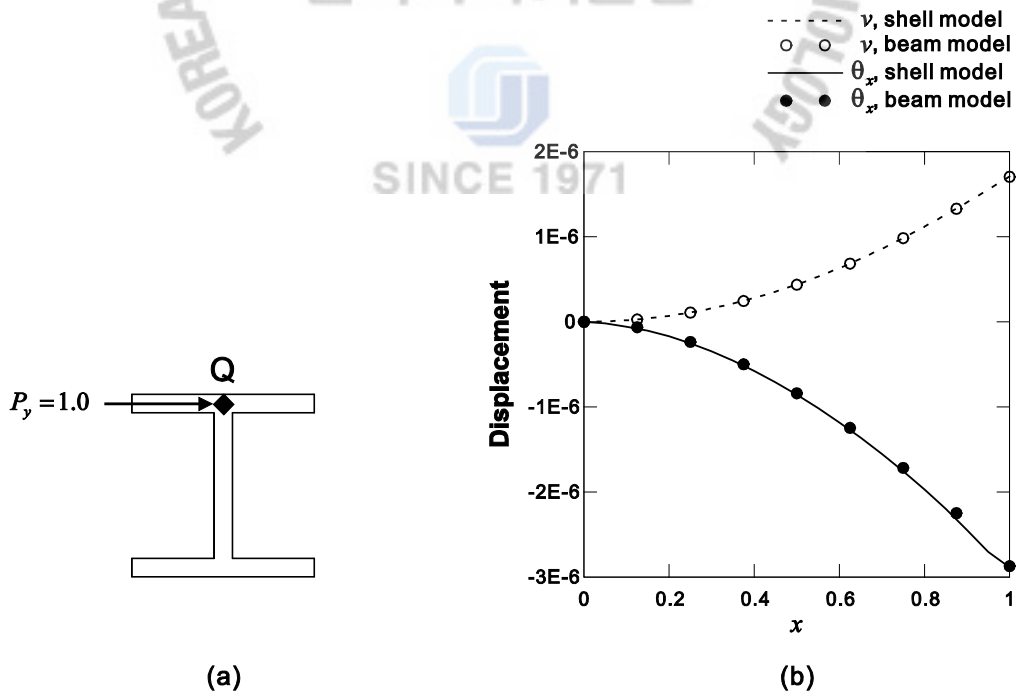


Figure 2-19. Displacement v and angle of twist along the beam length in varying wide flange cross-section beam problems with an eccentric end tip load ($\tan 0.5\theta = 0.025$).

2.4.5 Varying wide flange cross-section beam problems

Consider here the straight wide flange beam with a varying cross-section shown in Fig. 2-16. The boundary conditions are at , are $u = v = w = \theta_x = \theta_y = \theta_z = 0$ for free warping and $u = v = w = \theta_x = \theta_y = \theta_z = \alpha = 0$ for constrained warping. The beam dimensions are linearly decreasing from $x = 0$ to $x = 1.0$ except for the plate thicknesses that remain constant. A torsional moment $M_x = 1.0 N \cdot m$ is applied at tip ($x = 1.0$). For the beam model, seven 16-node cross-sectional elements for the wide flange cross-section are used as shown in Fig. 2-16(a).

For the shell finite element model to calculate reference solutions, see Fig. 2-16(b), $p = 20/3 N$ and the boundary conditions for the free and constrained warping cases are the same as in the curved wide flange cross-section beam problems. The angles of twist for the reference solutions are obtained from the rotation degrees of freedom of the shell elements.

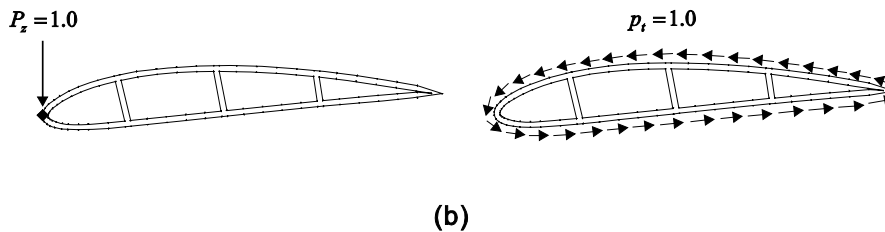
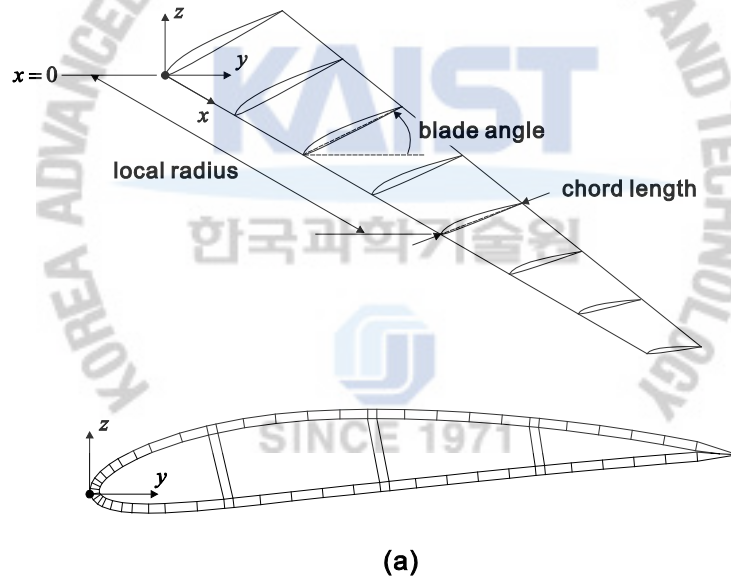


Figure 2-20. Wind turbine blade problems. (a) Geometry of the wind turbine blade with a NACA airfoil and cross-sectional mesh used, (b) Loading conditions. Left: flexural-torsion case, Right: pure torsion case (resultant moment: $M_x = 2.0 N \cdot m$).

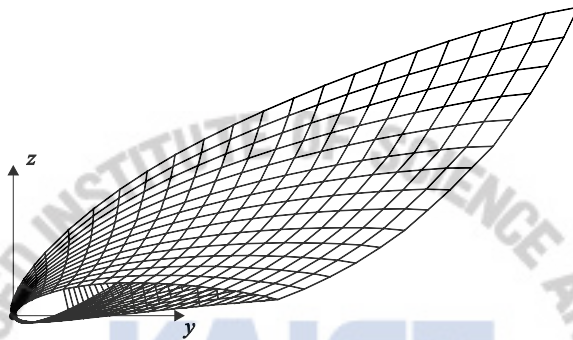
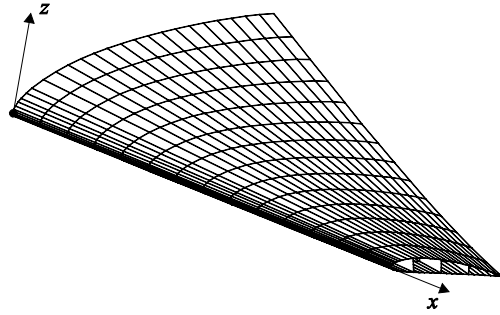


Figure 2-21. Shell element model for the wind turbine blade problems.

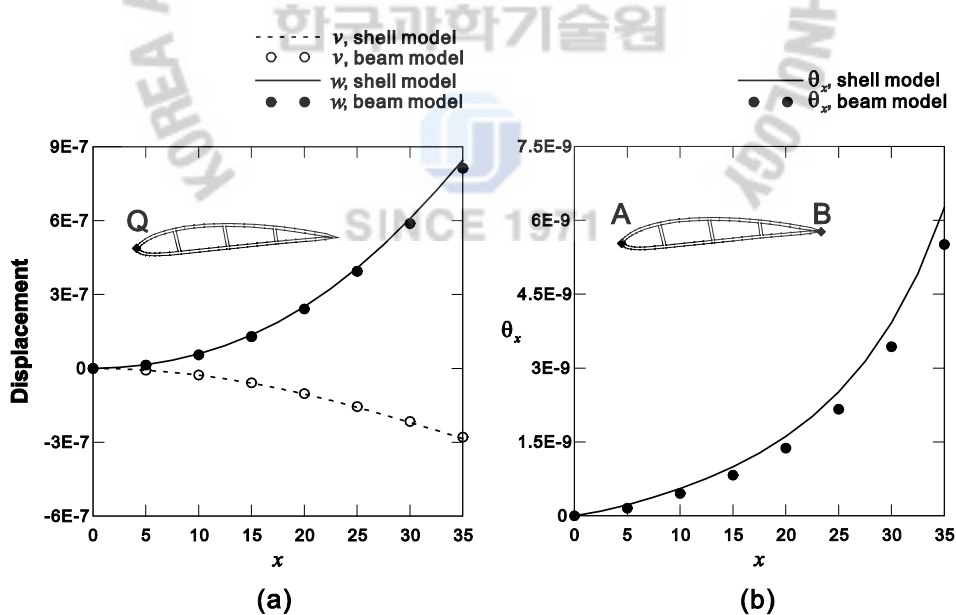


Figure 2-22. Displacements v , w and the angle of twist along the beam length in the wind turbine blade problems. (a) Flexural-torsion case. The displacements are given at point **Q**. (b) Pure torsion case. For the shell model, the angle of twist is evaluated from the relative displacements between two points **A** and **B** because the distribution of the angle is not uniform on the cross-section due to the effect of local deformation, but the angle of twist for the beam model is given at point **A**.

Fig. 2-17 shows the distributions of the displacements (the angles of twist and the warping displacement) corresponding to the point Q when four 3-node beam elements are used. Table 2-9 presents the angles of twist calculated for four different tapering degrees defined by $\tan 0.5\theta$ in Fig. 2-18. Until the tapering degree $\tan 0.5\theta = 0.225$, the numerical results show reasonable accuracy compared with the reference solutions. However, when the tapering degree is extremely high as in the case of $\tan 0.5\theta = 0.475$, the difference between the beam and shell solutions are large although more beam finite elements are used.

In Fig. 2-19, we present the displacement distribution when an eccentric lateral force $P_y = 1.0N$ is applied at the free tip ($x = 1.0$) in order to result in a flexure-torsion problem as shown in Fig. 2-19(a), and warping is constrained at the fixed end and $\tan 0.5\theta = 0.025$.

2.4.6 Wind turbine blade problem

We consider the wind turbine blade problem shown in Fig. 2-20(a). The geometry of the blade is described by the equations in Appendix A with design parameters $L = 35m$, $c_0 = 8.395m$, $c_L = 3.425m$, $\beta_0 = 29\text{deg.}$, $\beta_L = 3.6\text{deg.}$, $p = 0.4$, $m = 0.04$, $h = 0.125$. Three stiffeners are positioned at $s = 0.2$, 0.5 and 0.75 along the blade length. The airfoil surfaces and stiffeners have thickness $t = 0.05m$.

The boundary condition at $x = 0$ is $u = v = w = \theta_x = \theta_y = \theta_z = \alpha = 0$, that is, warping is also constrained. Fig. 2-20(b) shows two different loading conditions on the cross-section at $x = L$: a transverse point load ($P_z = 1.0N$) to result in flexural-torsion behavior and a uniformly distributed load ($p_r = 1.0N/m$) around the airfoil surface to result in pure torsion.

To analyze the wind turbine blade problem using the beam finite elements, we use seven beam finite elements and sixty-one 4-node cross-sectional elements for the airfoil cross-section as in Fig. 2-20(a). The number of total degrees of freedom used is 56.

Using the MITC9 shell finite elements, reference solutions are calculated, see Fig. 2-21. All the degrees of freedom are fixed at $x = 0$. We use 770 shell elements and 4680 degrees of freedom for the shell model.

Figs. 2-22(a) and (b) show the numerical results for the flexural-torsion case and pure torsion cases, respectively. Although, for the beam model, we use only 1.2 percent of the degrees of freedom of the shell models, the beam model solutions exhibit excellent accuracy compared with the shell model solutions.

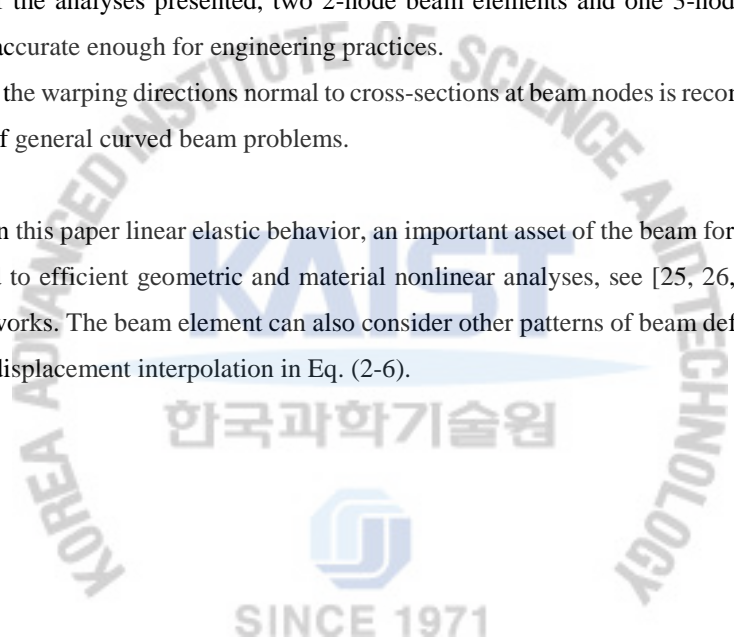
2.5 Concluding Remarks

In this chapter, we proposed a continuum mechanics based beam finite element with warping displacements. We presented the general formulation including how the geometry and displacements are defined and how warping displacements are efficiently accounted for. The novel features of the beam element are the simple and straightforward formulation, the inclusion of fully coupled warping effects, the ability of handling complicated geometry and only one additional degree of freedom at each beam node.

The various numerical results showed the effectiveness of the beam elements. Especially, excellent modeling capabilities and solution accuracy of the proposed beam element were observed. Regarding the beam problems considered, we have made the following observations:

- In order to correctly predict the torsional behaviors of beams with general cross-sections, the use of 16-node cross-sectional elements is effective. However, thin-walled cross-section beam problems, 4-node or 9-node cross-sectional elements can be enough.
- In most of the analyses presented, two 2-node beam elements and one 3-node beam element give solutions accurate enough for engineering practices.
- The use of the warping directions normal to cross-sections at beam nodes is recommended for accurate analyses of general curved beam problems.

While we assumed in this paper linear elastic behavior, an important asset of the beam formulation is that it can be directly extended to efficient geometric and material nonlinear analyses, see [25, 26, 30], and this will be described in future works. The beam element can also consider other patterns of beam deformation by properly enriching the basic displacement interpolation in Eq. (2-6).



Chapter 3. Continuity of Warping Displacement in Discontinuously Varying Beam

In this chapter, we propose a new and efficient warping displacement model to ensure the continuity of warping in beams with discontinuously varying arbitrary cross-sections. The obtained warping displacement fields are not only continuous in the entire domain of the beams, but also fully coupled with the other basic behaviors of the beam (stretching, shearing, and bending) [51].

3.1 Motivation

Beams widely used in many engineering applications have been analyzed by the finite element method. It is well known that appropriate consideration of the warping effect in the finite element analysis of non-circular cross-section beams is crucial for an accurate prediction of their twisting behavior [1-3].

In displacement-based beam finite element formulations, warping effects can be accounted for by adding warping displacement fields to Timoshenko's basic displacement fields. It is very important to appropriately construct the additional warping displacement fields in the beam formulations and there have been many studies, see Refs. [23, 43-50] and therein. Most previous studies have focused on relatively simple continuously varying cross-section beams, such as prismatic and tapered beams, see Fig. 3-1 (a). When the cross-section discontinuously varies along the beam length as shown in Fig. 3-1 (b), the variation in the warping displacement is very complicated. Most existing formulations cannot properly represent the complicated warping behavior.

To describe the torsional warping effect in discontinuously varying thin-walled cross-section beams, a kinematic compatibility condition has been proposed to consider the interaction between two different cross-sections at a discontinuous interface [33, 36]. The warping displacement models require a single warping DOF at each beam node in thin-walled cross-section beams. When a discontinuously varying cross-section beam is subjected to torsion, the twisting center also varies along the beam length. However, this effect is not considered in the previous beam formulations.

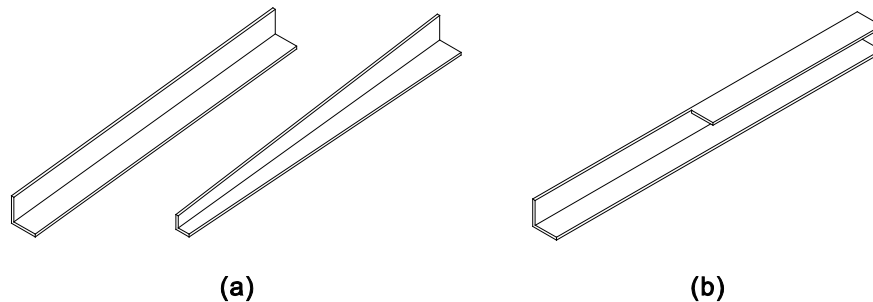


Figure 3-1. Various beam problems. (a) Beam problems with continuous varying cross-section (prismatic and tapered beams), (b) Beam problem with discontinuously varying cross-section.

An easy and simple method of modeling the warping displacements in discontinuously varying cross-section beams is to discretize the beam cross-sections with cross-sectional elements and nodes and to properly construct the continuity of nodal warping DOFs between two cross-sectional meshes at the interface [48, 49]. Since, in this warping displacement model, a large number of warping DOFs is required at each beam node and the number of warping DOFs depends on the cross-sectional meshes used, this warping displacement model has not been widely used.

In this study, we develop a new and efficient modeling method to construct the continuous warping displacement fields for discontinuously varying arbitrary cross-section beams. In order to model the continuity of warping, we define three basis warping functions (one free warping function and two interface warping functions) and the corresponding warping DOFs. The basis warping functions are multiplied by the corresponding warping DOFs and interpolated along the beam length. Therefore, in our warping displacement model, at most three warping DOFs are required at each beam node for torsional warping displacement fields. Furthermore, the three warping DOFs can be condensed when the same functions exist among the basis warping functions.

The obtained warping displacement fields are not only continuous in the entire domain of the beams, but also fully coupled with the other basic behaviors of the beam (stretching, shearing, and bending) by employing the formulation of continuum mechanics based beam finite elements as proposed in our previous study [50]. The greatest advantage of the continuum mechanics based beam finite elements is their modeling ability to easily deal with very complicated beam geometries. In the warping displacement model, it is crucial to obtain the correct twisting centers. Otherwise, the warping effect coupled with stretching, shearing, and bending cannot be properly considered and erroneous responses will be obtained.

The most challenging issue in this study is how to calculate the interface warping functions without knowing the twisting centers at the interfaces. In order to solve this problem, we develop a new method to simultaneously calculate the free warping function and the corresponding twisting center. Based on the method, the interface warping functions and the corresponding twisting center are also simultaneously calculated by solving a set of coupled equations at interfaces where the cross-section discontinuously varies. In the coupled equations, the Lagrange multiplier is employed to enforce the continuity of warping at the interface.

3.2 Modeling of Warping Displacement Fields

In this section, based on the formulation of the continuum mechanics based beam finite element allowing warping displacements, we introduce a new approach to constructing the continuity of warping with the definition of three basis warping functions. In the beam formulation, warping is fully coupled with bending, shearing, and stretching. The beam element can consider free/constrained warping conditions and uniform/non-uniform torsions, and model eccentricities, curved geometries, continuously varying cross-sections, as well as arbitrary cross-sections (including thin/thick-walled, open/closed, and single/multi-cell cross-sections).

3.2.1 New Warping Displacement Model

The variation in warping displacements is very complicated around discontinuous interfaces and the twisting center also varies along the beam length direction. Therefore, it is difficult to construct the warping displacement field by using only the free warping function obtained by St. Venant equation. The basic idea of this study is that the complicated warping displacement field $\mathbf{u}_w^{(m)}$ in Eq. (2-9) can be represented by a linear combination of the free warping function and the warping functions at the discontinuous interface. However, it is challenging to find the interface warping functions that satisfy the continuity of warping displacements. In particular, it is not easy to find the centers of the twist on the interface cross-sections. These were not found in previous studies.

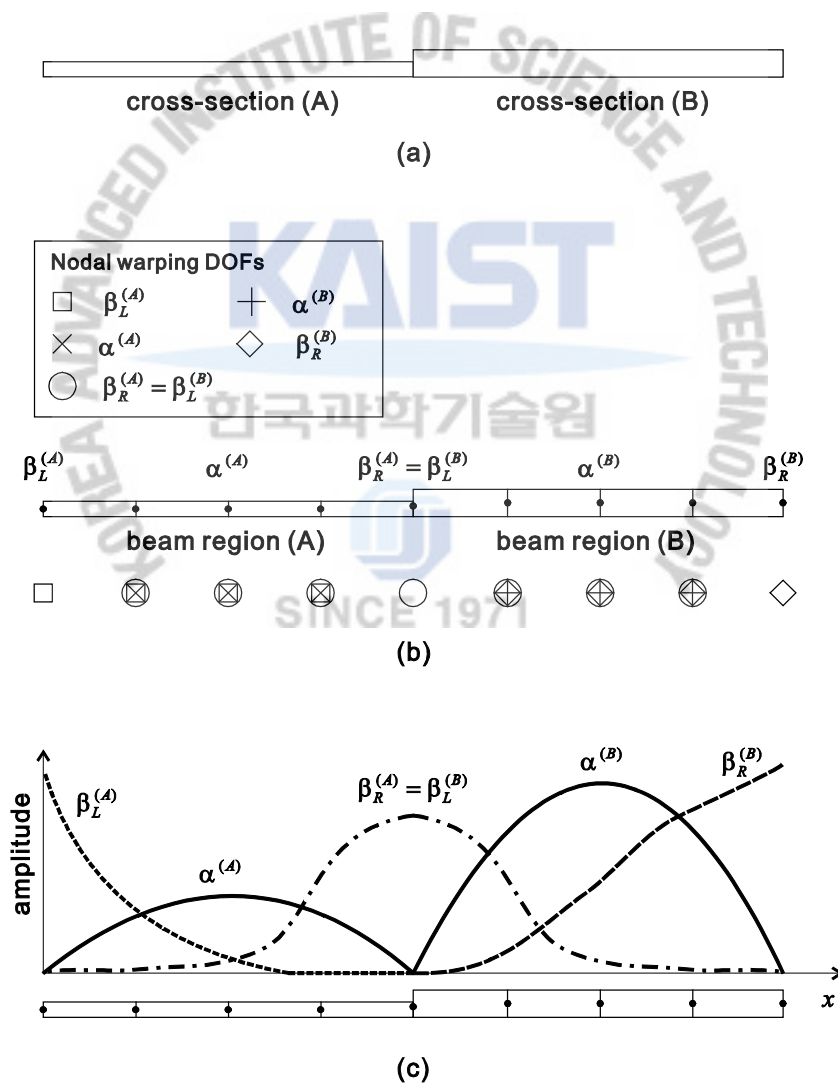


Figure 3-2. Warping DOFs used for a discontinuously varying cross-section beam. (a) A discontinuously varying cross-section beam, (b) Finite element model and warping DOF used at each nodes, (c) Individual amplitude of the basis warping functions along the beam length.

We here define three basis warping functions: one free warping function ($f_k^{(m)}$) and two interface warping functions ($f_L^{(m)}$ and $f_R^{(m)}$) at both beam ends. A combination of these three basis warping functions with the corresponding three warping DOFs (α_k , β_L^k and β_R^k) constructs the continuous warping displacement fields for discontinuously varying cross-section beams

$$\mathbf{u}_w^{(m)}(r, s, t) = \sum_{k=1}^q h_k(r) \left[f_k^{(m)}(s, t) \alpha_k + f_L^{(m)}(s, t) \beta_L^k + f_R^{(m)}(s, t) \beta_R^k \right] \mathbf{V}_r^k. \quad (3-1)$$

Therefore, in general at most three warping DOFs are required at each beam node.

To demonstrate how to set up the warping DOFs, we consider a beam with a discontinuously varying cross-section, as shown in Fig. 3-2(a). The beam consists of two regions with different cross-sections. Beam regions A and B have cross-sections A and B, respectively. Each region is modeled by four beam finite elements, as shown in Fig. 3-2(b). In each beam region, all of the warping DOFs (α , β_L and β_R) are set to be continuous. Each beam region has interfaces at the left and right ends; that is, free and constrained ends are also considered as interfaces. At each interface, two warping DOFs except for the warping DOF corresponding to the interface are set to be zero, as shown in Fig. 3-2(b). At the interface of both beam regions, the interface warping DOFs $\beta_R^{(A)} = \beta_L^{(B)}$ and the other DOFs are set to be zero. Therefore, the interface DOFs make the warping displacements continuous at the interfaces. Fig. 3-2(c) shows the possible distributions of the warping DOFs along the beam length.

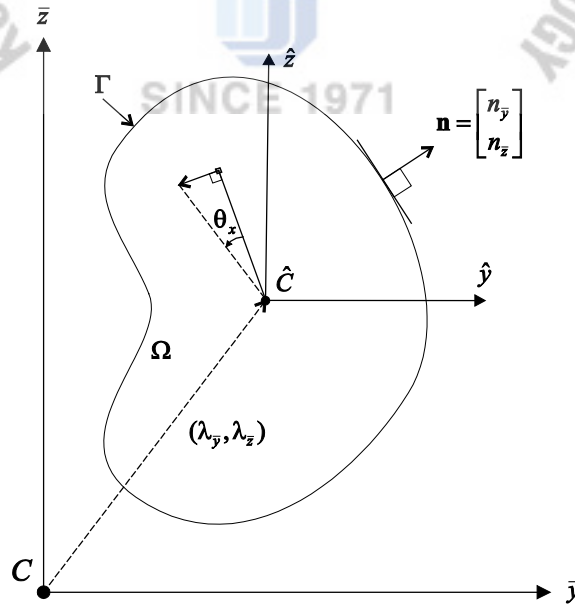


Figure 3-3. Twisting kinematics and twisting center.

3.2.2 Free Warping Function

In our previous study [50], to calculate free warping functions, the following three-step calculation is required as in Ref. [18]: In the first step, St. Venant equation is solved for a certain arbitrary coordinate system. In the second step, the twisting center is calculated using the warping function obtained in the first step. In the third step, the final warping function is obtained by the coordinate transformation of the warping function obtained in the first step using the twisting center calculated in the second step.

Here we present a newly developed single-step method to simultaneously calculate the free warping function and the corresponding twisting center in arbitrary beam cross-sections.

Let us consider the cross-sectional domain Ω defined in the cross-sectional Cartesian coordinates \bar{y} and \bar{z} with the origin C , as shown in Fig. 3-3. The position of the origin C can be arbitrarily chosen in the cross-section. The cross-sectional domain Ω is subjected to pure twisting kinematics about the twisting center \hat{C} , where bending and transverse shearing are not involved. Then, the displacement fields are obtained as

$$u = kf, \quad v = -\hat{z}\theta_x \quad \text{and} \quad w = \hat{y}\theta_x \quad \text{in } \Omega, \quad (3-2)$$

where $k = \partial\theta_x/\partial x$, $f(\hat{y}, \hat{z})$ is the warping function corresponding to the twisting center and \hat{y} and \hat{z} are the coordinates in the cross-sectional Cartesian coordinate system defined at the twisting center \hat{C} .

Note that in general the position of the twisting center $(\lambda_{\bar{y}}, \lambda_{\bar{z}})$ is unknown. After the warping function corresponding to the origin C is obtained, the twisting center can be calculated, and then the correct warping function corresponding to the twisting center \hat{C} can be obtained through a transformation procedure, as in Refs. [18, 50]. However, in the method proposed in this study, the warping function and the twisting center are obtained at the same time. This is a very important feature in obtaining the interface warping functions.

The displacement field in Eq. (3-2) results in the transverse shear stress fields

$$\tau_{x\hat{y}} = Gk \left(\frac{\partial f}{\partial \hat{y}} - \hat{z} \right) \quad \text{and} \quad \tau_{x\hat{z}} = Gk \left(\frac{\partial f}{\partial \hat{z}} + \hat{y} \right) \quad \text{in } \Omega, \quad (3-3)$$

in which G is the shear modulus. Note that other stresses are zero.

By applying Eq. (3-3) to the local equilibrium equations [18, 50], the well-known St. Venant equations are obtained

$$G \left(\frac{\partial^2 f}{\partial \hat{y}^2} + \frac{\partial^2 f}{\partial \hat{z}^2} \right) = 0 \quad \text{in } \Omega, \quad n_{\bar{y}} \frac{\partial f}{\partial \hat{y}} + n_{\bar{z}} \frac{\partial f}{\partial \hat{z}} = n_{\bar{y}} \hat{z} - n_{\bar{z}} \hat{y} \quad \text{on } \Gamma, \quad (3-4)$$

where $(n_{\bar{y}}, n_{\bar{z}})$ is the vector normal to the cross-sectional boundary, see Fig. 3-3.

The variational formulation can be easily derived with the variation of the warping function δf ,

$$\int_{\Omega} G \left(\frac{\partial f}{\partial \hat{y}} \frac{\partial \delta f}{\partial \hat{y}} + \frac{\partial f}{\partial \hat{z}} \frac{\partial \delta f}{\partial \hat{z}} \right) d\Omega = \int_{\Gamma} G (n_{\bar{y}} \hat{z} - n_{\bar{z}} \hat{y}) \delta f d\Gamma. \quad (3-5)$$

Using the relation between the two cross-sectional Cartesian coordinate systems denoted as (\bar{y}, \bar{z}) and (\hat{y}, \hat{z}) , $\hat{y} = \bar{y} - \lambda_{\bar{y}}$ and $\hat{z} = \bar{z} - \lambda_{\bar{z}}$, in Eq. (3-5), we obtain

$$G \int_{\Omega} \left(\frac{\partial f}{\partial \bar{y}} \frac{\partial \delta f}{\partial \bar{y}} + \frac{\partial f}{\partial \bar{z}} \frac{\partial \delta f}{\partial \bar{z}} \right) d\Omega + G \lambda_{\bar{z}} \int_{\Gamma} (n_{\bar{y}} \delta f) d\Gamma - G \lambda_{\bar{y}} \int_{\Gamma} (n_{\bar{z}} \delta f) d\Gamma = G \int_{\Gamma} (n_{\bar{y}} \bar{z} - n_{\bar{z}} \bar{y}) \delta f d\Gamma. \quad (3-6)$$

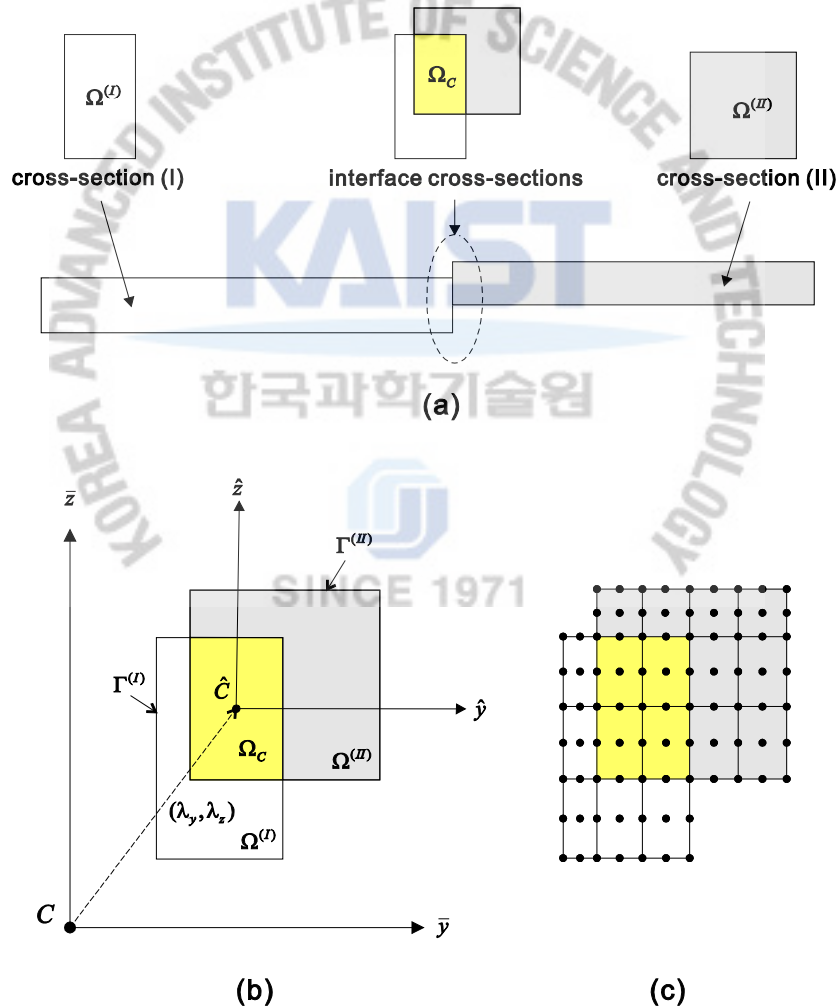


Figure 3-4. Cross-sections of a discontinuously varying cross-section beam. (a) Cross-sections (I) and (II), and their interface Ω_c , (b) Interconnected domain and twisting center, (c) Cross-sectional meshes used at the interface.

Since the pure twisting kinematics does not produce bending moments in the cross-section, the zero bending moment condition $M_{\bar{z}} = M_{\bar{y}} = 0$ gives

$$G \int_{\Omega} (\bar{y} - \bar{y}_{ave}) f \delta f d\Omega = 0 \quad \text{and} \quad G \int_{\Omega} (\bar{z} - \bar{z}_{ave}) f \delta f d\Omega = 0 \quad (3-7)$$

with the location of the cross-sectional centroid being

$$\bar{y}_{ave} = \frac{\int_{\Omega} \bar{y} d\Omega}{\int_{\Omega} d\Omega} \quad \text{and} \quad \bar{z}_{ave} = \frac{\int_{\Omega} \bar{z} d\Omega}{\int_{\Omega} d\Omega} . \quad (3-8)$$

In order to discretize the three equations in Eqs. (3-6) and (3-7), the warping function is interpolated as in Eq. (2-9). Applying the standard procedure of the finite element method, the matrix equations are obtained

$$\begin{bmatrix} \mathbf{GK} & \mathbf{GN}_{\bar{y}} & -\mathbf{GN}_{\bar{z}} \\ \mathbf{GH}_{\bar{y}} & \mathbf{0} & \mathbf{0} \\ \mathbf{GH}_{\bar{z}} & \mathbf{0} & \mathbf{0} \end{bmatrix} \begin{bmatrix} \mathbf{F} \\ \lambda_{\bar{z}} \\ \lambda_{\bar{y}} \end{bmatrix} = \begin{bmatrix} \mathbf{GB} \\ 0 \\ 0 \end{bmatrix} \quad \text{in } \Omega , \quad (3-9)$$

where \mathbf{F} is the vector of the unknown nodal warping values, \mathbf{K} , $\mathbf{N}_{\bar{y}}$, and $\mathbf{N}_{\bar{z}}$ are the matrices obtained from the left-hand side of Eq. (3-6), \mathbf{B} is the vector obtained from the right-hand side of Eq. (3-6), and $\mathbf{H}_{\bar{y}}$ and $\mathbf{H}_{\bar{z}}$ are the matrices obtained from Eq. (3-7). Solving Eq. (3-9), we can simultaneously calculate both the warping function and the corresponding twisting center.

3.2.3 Interface Warping Function

The warping functions and the position of the corresponding twisting center at interfaces have not been studied before. In this section, we present a method to calculate the interface warping functions and the corresponding twisting center by solving a set of coupled equations.

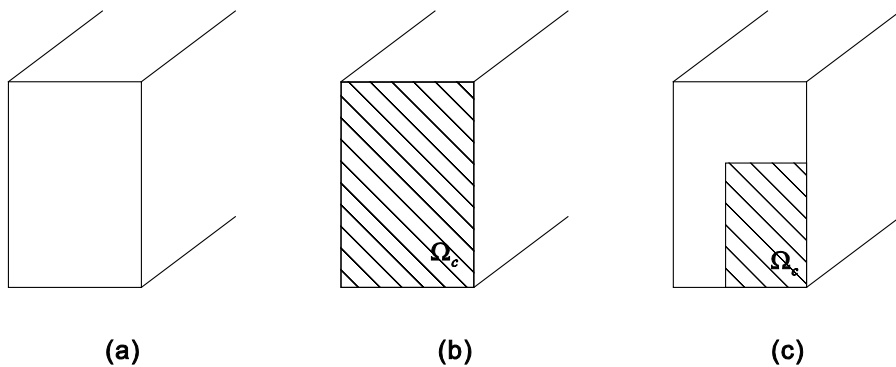


Figure 3-5. Three special cases for the interface warping functions. (a) Free interface, (b) Fully constrained interface, (c) Partially constrained interface.

Let us define the interface cross-sections, as shown in Fig. 3-4. The cross-sectional domains $\Omega^{(I)}$ and $\Omega^{(II)}$ have shear moduli G_1 and G_2 , respectively. Eq. (3-9) can be rewritten for each cross-sectional domain

$$\begin{bmatrix} G_1 \mathbf{K}^{(I)} & G_1 \mathbf{N}_{\bar{y}}^{(I)} & -G_1 \mathbf{N}_{\bar{z}}^{(I)} & \mathbf{L}^{(I)} \\ G_1 \mathbf{H}_{\bar{y}}^{(I)} & \mathbf{0} & \mathbf{0} & \mathbf{0} \\ G_1 \mathbf{H}_{\bar{z}}^{(I)} & \mathbf{0} & \mathbf{0} & \mathbf{0} \end{bmatrix} \begin{bmatrix} \mathbf{F}^{(I)} \\ \lambda_{\bar{z}} \\ \lambda_{\bar{y}} \\ \lambda \end{bmatrix} = \begin{bmatrix} G_1 \mathbf{B}^{(I)} \\ 0 \\ 0 \\ \mathbf{0} \end{bmatrix} \quad \text{for } \Omega^{(I)}, \quad (3-10)$$

$$\begin{bmatrix} G_2 \mathbf{K}^{(II)} & G_2 \mathbf{N}_{\bar{y}}^{(II)} & -G_2 \mathbf{N}_{\bar{z}}^{(II)} & -\mathbf{L}^{(II)} \\ G_2 \mathbf{H}_{\bar{y}}^{(II)} & \mathbf{0} & \mathbf{0} & \mathbf{0} \\ G_2 \mathbf{H}_{\bar{z}}^{(II)} & \mathbf{0} & \mathbf{0} & \mathbf{0} \end{bmatrix} \begin{bmatrix} \mathbf{F}^{(II)} \\ \lambda_{\bar{z}} \\ \lambda_{\bar{y}} \\ \lambda \end{bmatrix} = \begin{bmatrix} G_2 \mathbf{B}^{(II)} \\ 0 \\ 0 \\ \mathbf{0} \end{bmatrix} \quad \text{for } \Omega^{(II)}, \quad (3-11)$$

where $\mathbf{L}^{(I)}$ and $\mathbf{L}^{(II)}$, and λ are Boolean matrices and the Lagrange multiplier vector, respectively, to enforce the constraint condition such that the warping values in both cross-sectional domains should be equal in the interconnected area Ω_C

$$\begin{bmatrix} \mathbf{L}^{(IT)} & -\mathbf{L}^{(IIT)} \end{bmatrix} \begin{bmatrix} \mathbf{F}^{(I)} \\ \mathbf{F}^{(II)} \end{bmatrix} = [\mathbf{0}] \quad \text{for } \Omega_C. \quad (3-12)$$

Eqs. (3-10), (3-11), and (3-12) finally give a set of five coupled equations in a matrix form

$$\begin{bmatrix} G_1 \mathbf{K}^{(I)} & \mathbf{0} & G_1 \mathbf{N}_{\bar{y}}^{(I)} & -G_1 \mathbf{N}_{\bar{z}}^{(I)} & \mathbf{L}^{(I)} \\ \mathbf{0} & G_2 \mathbf{K}^{(II)} & G_2 \mathbf{N}_{\bar{y}}^{(II)} & -G_2 \mathbf{N}_{\bar{z}}^{(II)} & -\mathbf{L}^{(II)} \\ G_1 \mathbf{H}_{\bar{y}}^{(I)} & G_2 \mathbf{H}_{\bar{y}}^{(II)} & \mathbf{0} & \mathbf{0} & \mathbf{0} \\ G_1 \mathbf{H}_{\bar{z}}^{(I)} & G_2 \mathbf{H}_{\bar{z}}^{(II)} & \mathbf{0} & \mathbf{0} & \mathbf{0} \\ \mathbf{L}^{(IT)} & -\mathbf{L}^{(IIT)} & \mathbf{0} & \mathbf{0} & \mathbf{0} \end{bmatrix} \begin{bmatrix} \mathbf{F}^{(I)} \\ \mathbf{F}^{(II)} \\ \lambda_{\bar{z}} \\ \lambda_{\bar{y}} \\ \lambda \end{bmatrix} = \begin{bmatrix} G_1 \mathbf{B}^{(I)} \\ G_2 \mathbf{B}^{(II)} \\ 0 \\ 0 \\ \mathbf{0} \end{bmatrix}, \quad (3-13)$$

in which the first and second equations are St. Venant equations corresponding to the two different cross-sectional domains, the third and fourth equations correspond to the zero bending moment conditions in Eq. (3-7), and the last equation is the constraint equation that enforces the continuity of warping in the interconnected cross-sectional area.

Solving Eq. (3-13), we can calculate the interface warping functions, which are used as basis warping functions in the warping displacement model for discontinuously varying cross-section beams.

It is essential to note three special cases for the interface warping functions, as shown in Fig. 3-5.

- Free interface: At the interface, no connected cross-section exists. This means that warping is free and the interface warping function thus becomes equal to the free warping function. Therefore, the corresponding interface warping DOF can be condensed out by setting it to zero.
- Fully constrained interface: The whole interface cross-section is connected to a rigid wall. Thus, warping is fully constrained and the corresponding interface warping function vanishes. Therefore, the corresponding interface DOF needs to be removed by setting it to zero.

- Partially constrained interface: A part of the interface is connected with a rigid wall. To solve this case, Eq. (3-13) should be modified. The cross-sectional domain $\Omega^{(II)}$ is assumed to be rigid. Using the condition $G_2 \rightarrow \infty$ in Eq. (3-13), we then obtain

$$\begin{bmatrix} \mathbf{K}^{(I)} & \mathbf{0} & \mathbf{N}_{\bar{y}}^{(I)} & -\mathbf{N}_{\bar{z}}^{(I)} & \mathbf{L}^{(I)} \\ \mathbf{0} & \mathbf{K}^{(II)} & \mathbf{N}_{\bar{y}}^{(II)} & -\mathbf{N}_{\bar{z}}^{(II)} & \mathbf{0} \\ \mathbf{0} & \mathbf{H}_{\bar{y}}^{(II)} & \mathbf{0} & \mathbf{0} & \mathbf{0} \\ \mathbf{0} & \mathbf{H}_{\bar{z}}^{(II)} & \mathbf{0} & \mathbf{0} & \mathbf{0} \\ \mathbf{L}^{(I)T} & \mathbf{0} & \mathbf{0} & \mathbf{0} & \mathbf{0} \end{bmatrix} \begin{bmatrix} \mathbf{F}^{(I)} \\ \mathbf{F}^{(II)} \\ \lambda_{\bar{z}} \\ \lambda_{\bar{y}} \\ \lambda \end{bmatrix} = \begin{bmatrix} \mathbf{B}^{(I)} \\ \mathbf{B}^{(II)} \\ 0 \\ 0 \\ \mathbf{0} \end{bmatrix}. \quad (3-14)$$

Fig. 3-6 shows the DOFs used for the free-free, constrained-free, and constrained-constrained warping conditions. Finally, we note that when beams have a continuously varying cross-section, as shown in Fig. 3-1(a), two interface warping functions ($f_L^{(m)}$ and $f_R^{(m)}$) become equal to the free warping function ($f_k^{(m)}$). Therefore, the interface warping functions can be condensed out, and only the free warping function and the corresponding DOF are necessary in the beam element formulation.

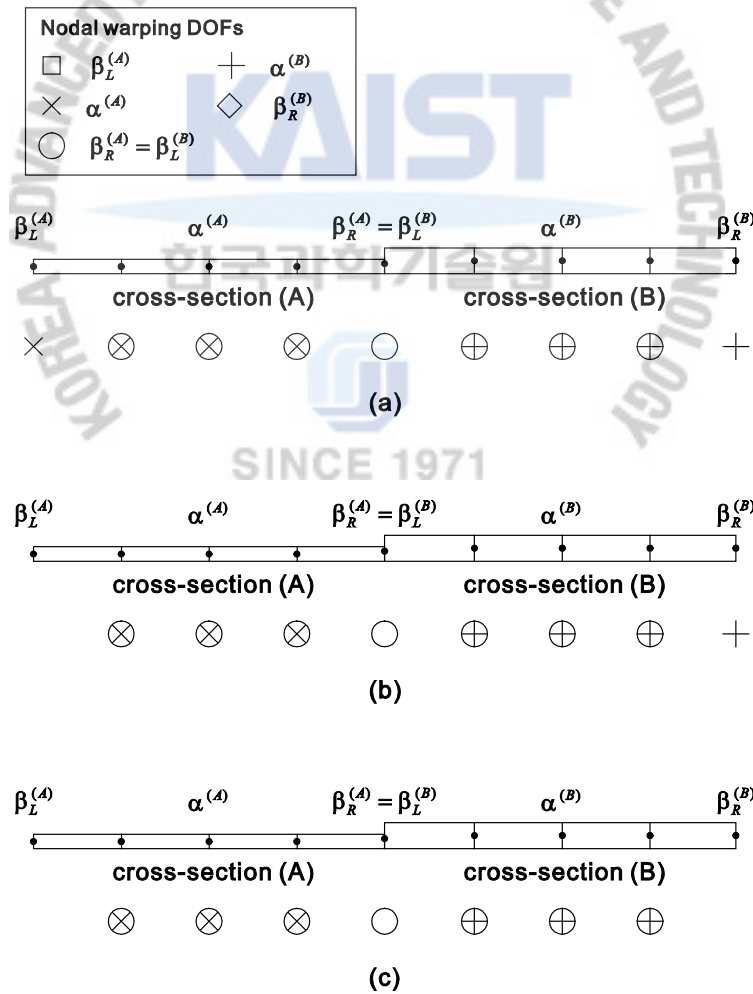


Figure 3-6. Nodal warping DOFs used for (a) free-free, (b) constrained-free, (c) constrained-constrained warping problems.

3.3 Numerical Studies

To verify the performance of the warping displacement model proposed in this study, we numerically solve three beam problems: a step varying rectangular cross-section problem, a discontinuously varying thin-walled cross-section problem, a partially constrained warping problem, and a curved beam problem with a discontinuously varying cross-section. The results are compared with reference solutions obtained by using refined solid and shell element models. In addition, the solutions of the beam element model with the warping displacement model in Eq. (2-13) are compared. Note that two-node linear beam finite elements are used for all of the beam models and that the well-known reduced integration is employed in order to avoid shear locking [3, 50]. A Young's modulus $E = 2.0 \times 10^{11} \text{ N/m}^2$ and a Poisson's ratio $\nu = 0$ are used for all of the beam problems considered in this section³.

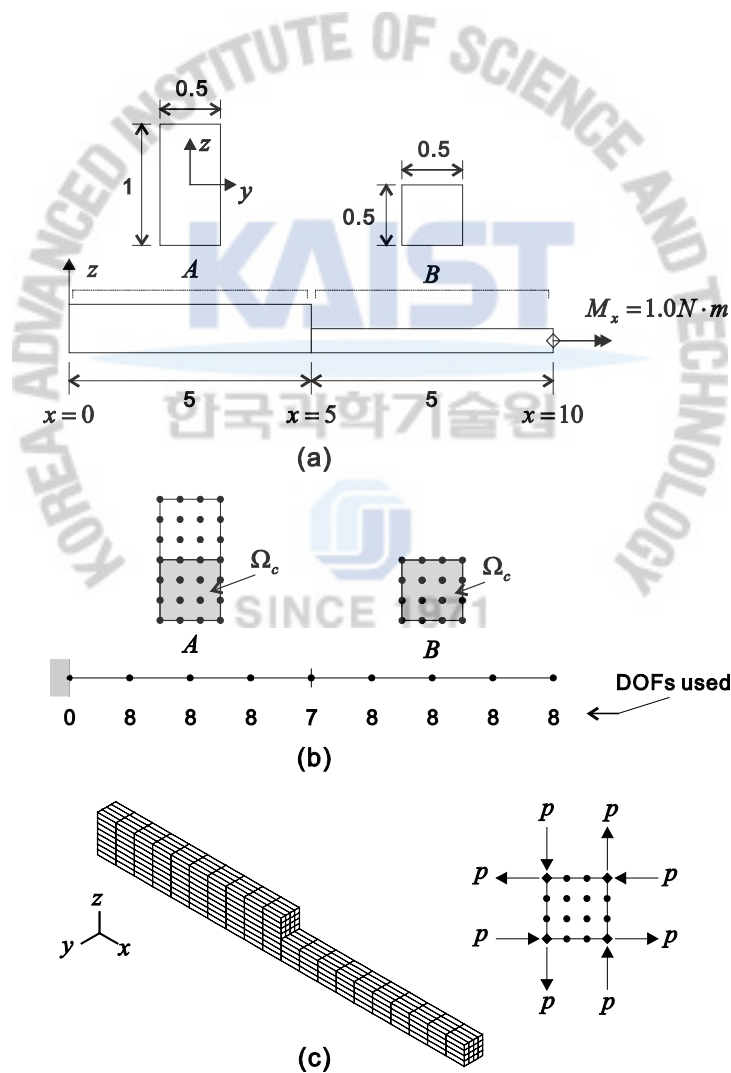


Figure 3-7. Step varying rectangular cross-section problem. (a) Problem description (unit: m), (b) Beam element model, cross-sectional mesh used and the number of each nodal DOFs used, (c) Solid element model used.

³ In order to avoid difficulties in specifying boundary conditions in equivalent shell and solid finite element models, zero Poisson's ratio is used.

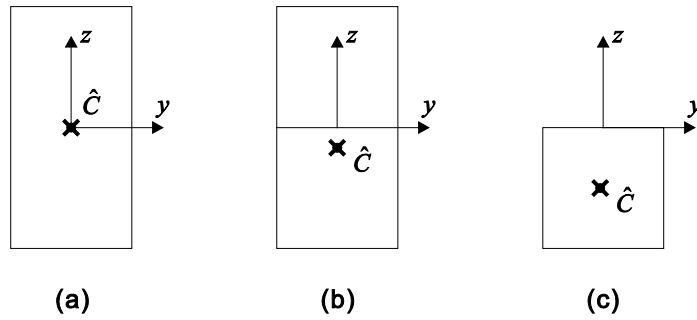


Figure 3-8. Twisting centers in the step varying rectangular cross-section problem. (a) $(\lambda_y, \lambda_z) = (0, 0)$ for the free warping function of cross-section A , (b) $(\lambda_y, \lambda_z) = (0, -0.0833)$ for the interface warping function at $x = 5m$, (c) $(\lambda_y, \lambda_z) = (0, -0.25)$ for the free warping function of cross-section B .

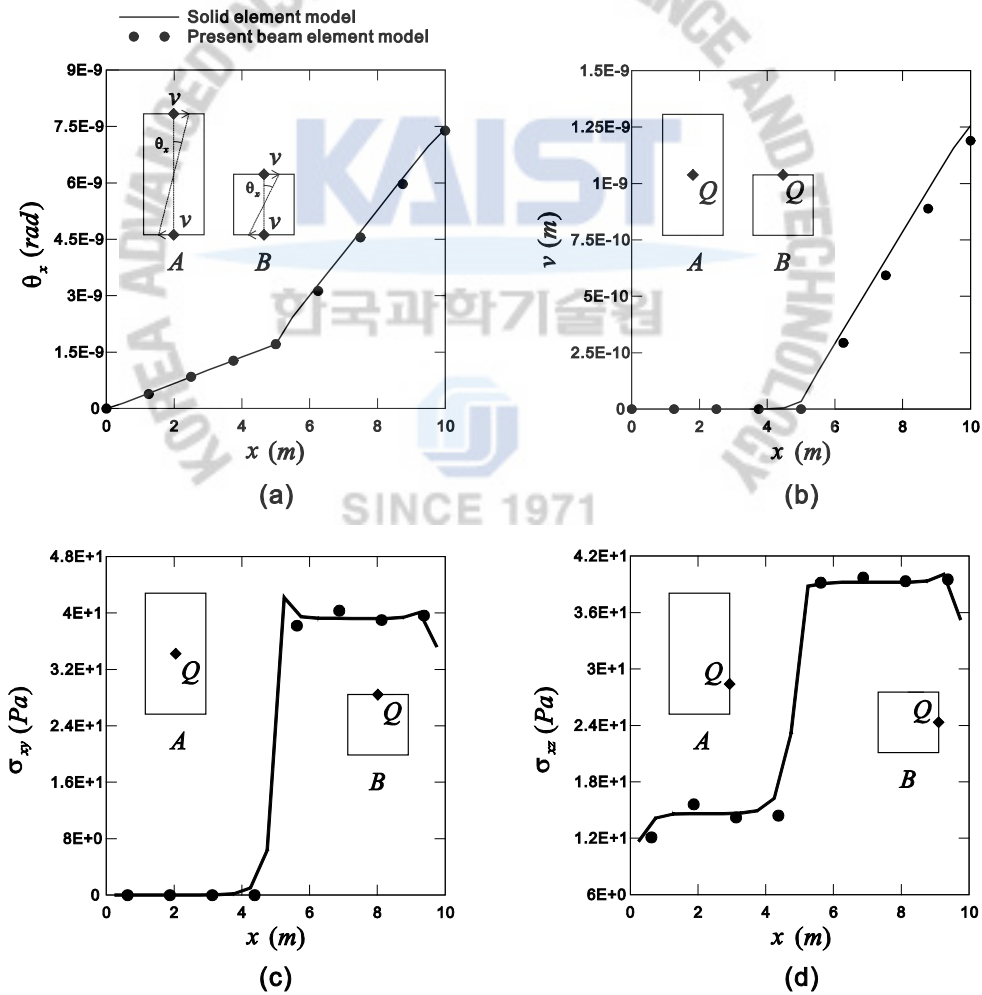


Figure 3-9. Numerical results along the beam length in the step varying rectangular cross-section problem. (a) Angle of twist, (b) Transverse displacement v at Q , (c) Shear stress σ_{xy} at Q , (d) Shear stress σ_{xz} at Q .

3.3.1 Step Varying Rectangular Cross-section Problem

We consider a step varying rectangular cross-section problem with two beam regions corresponding to two different cross-sections, A and B , as shown in Fig. 3-7(a). All of the displacements including warping are constrained at $x=0m$ and a torsional moment $M_x=1.0N \cdot m$ is applied at $x=10m$. The rectangular cross-section is discontinuous at $x=5m$. The beam problem is modeled by the proposed beam element, as shown in Fig. 3-7(b). The cross-sections A and B are discretized by two and one 16-node cubic cross-sectional elements, respectively, and have an interconnected area Ω_c at $x=5m$.

The beam region with cross-section A is modeled by four beam elements that have eight nodal DOFs $[u \ v \ w \ \theta_x \ \theta_y \ \theta_z \ \alpha^{(A)} \ \beta_R^{(A)}]^T$. The interface warping DOF $\beta_L^{(A)}$ is removed by setting $\beta_L^{(A)}=0$ because beam region A has a fully constrained interface at its left end ($x=0m$). The beam region with cross-section B is modeled by four beam elements with eight nodal DOFs $[u \ v \ w \ \theta_x \ \theta_y \ \theta_z \ \alpha^{(B)} \ \beta_R^{(B)}]^T$. Setting $\beta_R^{(B)}=0$, the interface warping DOF $\beta_L^{(B)}$ is condensed out because beam region B has a free interface at its right end. At $x=5m$, the interface warping function is shared through the continuity of interconnected DOFs ($\beta_R^{(A)}=\beta_L^{(B)}$) and $\alpha^{(A)}=\alpha^{(B)}=0$ at the interface node. The boundary condition $u=v=w=\theta_x=\theta_y=\theta_z=\alpha^{(A)}=\beta_R^{(A)}=0$ is applied at $x=0m$. The numbers of the nodal DOFs used are presented in Fig. 3-7(b).

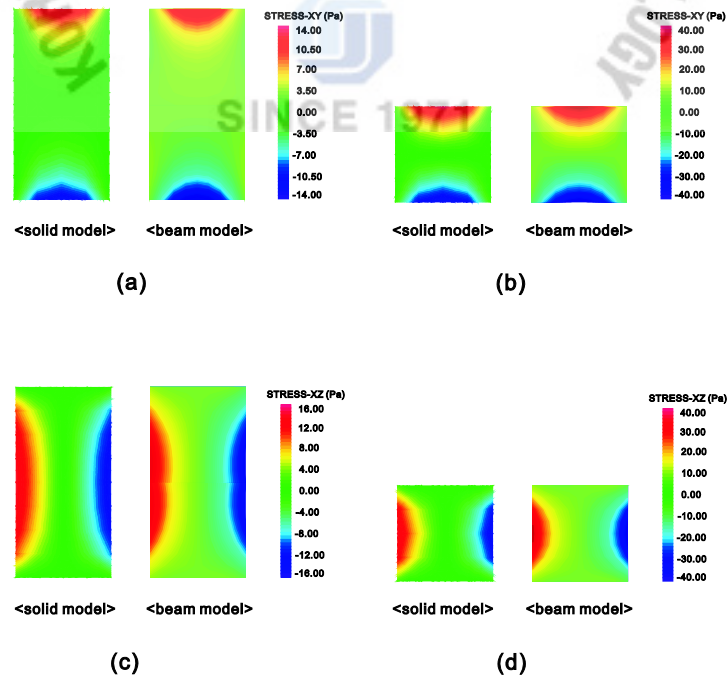


Figure 3-10. Transverse shear stresses in the cross-section for the step varying rectangular cross-section problem. (a) σ_{xy} at $x=2.5m$, (b) σ_{xy} at $x=7.5m$, (c) σ_{xz} at $x=2.5m$, (d) σ_{xz} at $x=7.5m$.

To calculate the reference solutions, 27-node quadratic solid finite elements are used, as shown in Fig. 3-7(c). In the solid element model, point loads ($p = 0.5N$) are applied to obtain the equivalent torsional moment $M_x = 1.0N \cdot m$ at $x = 10m$ and all DOFs are fixed at $x = 0m$.

Fig. 3-8 shows the positions of the twisting center for the free warping function of cross-sections A and B , and for the interface warping function at $x = 5m$. The variation of the twisting center along the beam length is automatically considered through the warping displacement field in Eq. (3-1).

Fig. 3-9 presents the numerical results along the beam length: showing the distribution of the angle of twist, displacement v , and transverse shear stresses σ_{xy} and σ_{xz} at point Q . Fig. 3-10 shows the distributions of transverse shear stresses σ_{xy} and σ_{xz} on the cross-sectional planes at $x = 2.5m$ and $x = 7.5m$. The numerical results demonstrate the excellent predictive capability of the warping displacement model proposed in this study. Note that the numbers of DOFs used are 63 and 4,680 in the beam and solid element models, respectively.

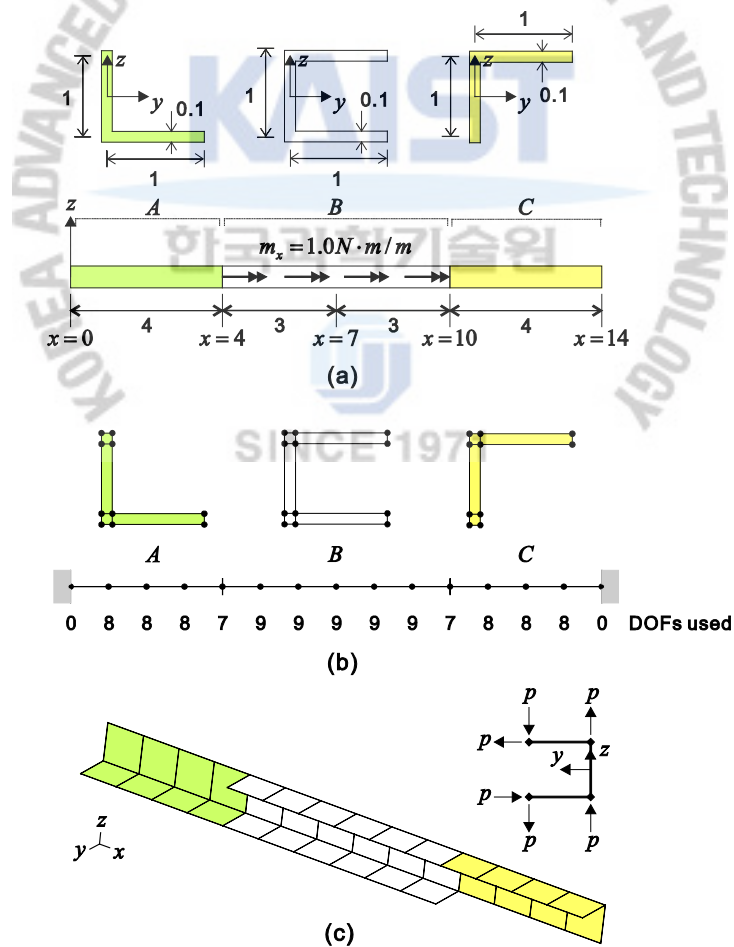


Figure 3-11. Discontinuously varying thin-walled cross-section beam problem. (a) Problem description (unit: m), (b) Beam element model, cross-sectional meshes used and the number of each nodal DOFs used, (c) Shell element model used.

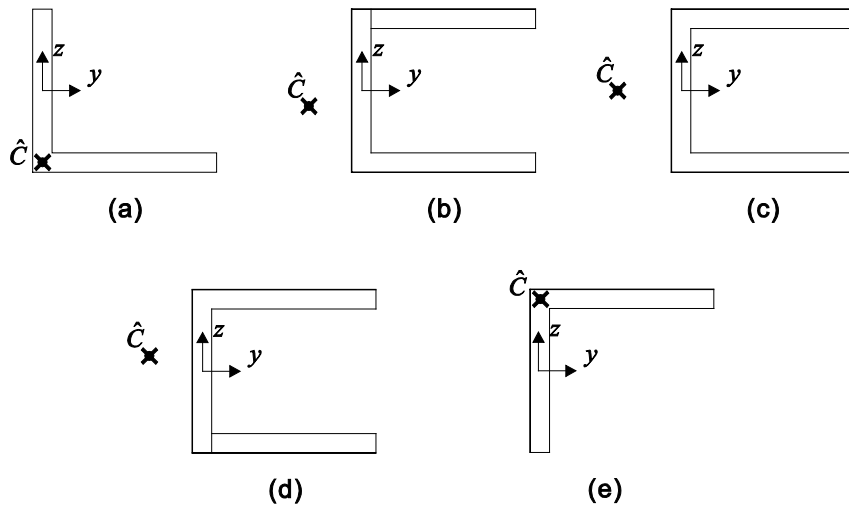


Figure 3-12. Twisting centers in the discontinuously varying thin-walled cross-section beam problem. (a) $(0.0037, -0.4952)$ for the free warping function of cross-section A , (b) $(-0.3584, -0.1037)$ for the interface warping function at $x = 4m$, (c) $(-0.4163, 0)$ for the free warping function of cross-section B , (d) $(-0.3584, 0.1037)$ for the interface warping function at $x = 10m$, (e) $(0.0037, 0.4952)$ for the free warping function of cross-section C .

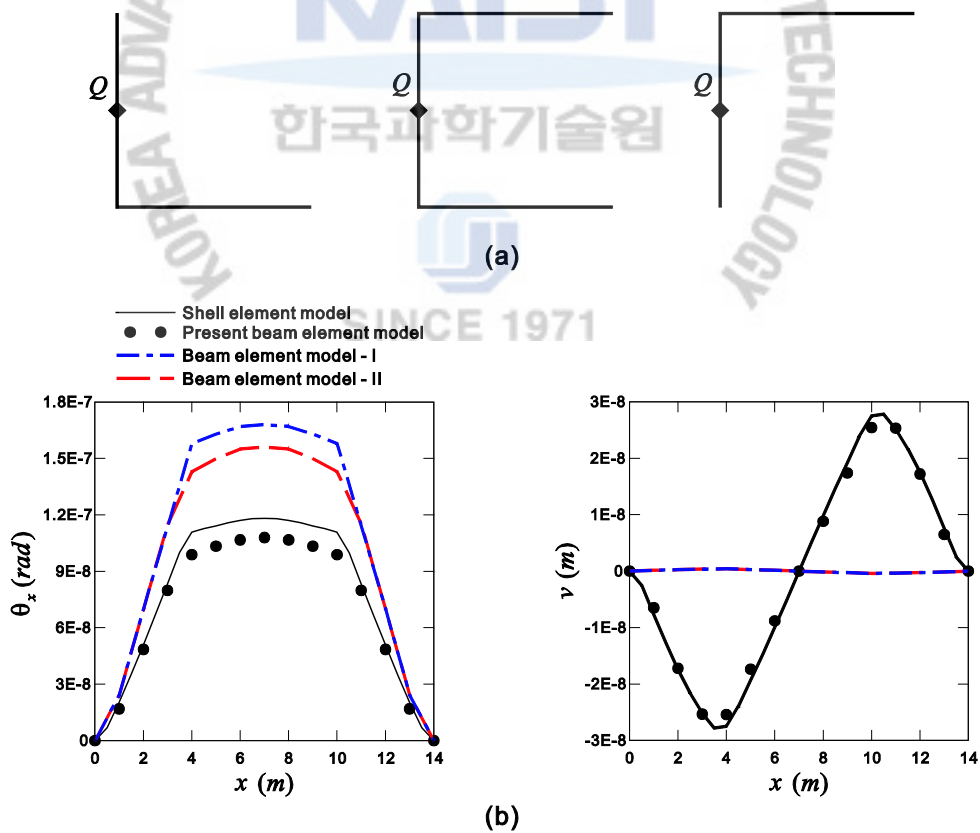


Figure 3-13. Angle of twist and displacement v along the beam length in the discontinuously varying thin-walled cross-section beam problem. (a) Sampling points Q in the cross-sections, (b) Angle of twist (left) and displacement v (right).

3.3.2 Discontinuously Varying Thin-walled Cross-section Problem

Let us consider a beam that consists of three beam regions corresponding to three different thin-walled cross-sections, A , $[u \ v \ w \ \theta_x \ \theta_y \ \theta_z \ \alpha^{(A)} \ \beta_R^{(A)}]^T$ and $\beta_L^{(A)}$, see Fig. 3-11(a). All displacements including warping are constrained at both ends (B and $x=0m$) and a distributed torsional moment $[u \ v \ w \ \theta_x \ \theta_y \ \theta_z \ \alpha^{(B)} \ \beta_L^{(B)} \ \beta_R^{(B)}]^T$ is applied at beam region B . The cross-section are discontinuous at $x=4m$ and $x=10m$. The physical problem is modeled by the proposed beam element model, as shown in Fig. 3-11(b). The cross-sections A , B and C are discretized by four-node linear cross-sectional elements, and the cross-sectional meshes are interconnected at $x=4m$ and $x=10m$.

Beam region A is modeled by four beam elements that have eight nodal DOFs $[u \ v \ w \ \theta_x \ \theta_y \ \theta_z \ \alpha^{(A)} \ \beta_R^{(A)}]^T$. The interface warping DOF $\beta_L^{(A)}$ is set to zero because the warping is fully constrained at $x=0m$. Beam region B is modeled by six beam elements with nine nodal DOFs $[u \ v \ w \ \theta_x \ \theta_y \ \theta_z \ \alpha^{(B)} \ \beta_L^{(B)} \ \beta_R^{(B)}]^T$. Beam region C is modeled by four beam elements with eight nodal DOFs $[u \ v \ w \ \theta_x \ \theta_y \ \theta_z \ \alpha^{(C)} \ \beta_L^{(C)}]^T$. The interface warping DOF $\beta_R^{(C)}$ is set to zero because the warping is fully constrained at $x=14m$. The interface warping functions are shared at $x=4m$ and $x=10m$ for the continuity of interconnected DOFs ($\beta_R^{(A)} = \beta_L^{(B)}$ and $\beta_R^{(B)} = \beta_L^{(C)}$) and $\alpha^{(A)} = \alpha^{(B)} = \alpha^{(C)} = 0$ at the interfaces. The boundary conditions $u = v = w = \theta_x = \theta_y = \theta_z = \alpha^{(A)} = \beta_R^{(A)} = 0$ and $u = v = w = \theta_x = \theta_y = \theta_z = \alpha^{(C)} = \beta_L^{(C)} = 0$ are applied at $x=0m$ and $x=14m$, respectively. The numbers of the nodal DOFs used are presented in Fig. 3-11(b).

To obtain the reference solutions, MITC9 shell finite elements are used in the shell element model shown in Fig. 3-11(c) [31-34]. Point loads ($p=1/3N/m$) are distributed along beam region B , which produces the equivalent distributed torsional moment $m_x=1.0N \cdot m/m$. Therefore, the torsion is non-uniform along beam region B .

Fig. 3-12 shows the positions of the twisting centers for the free warping functions in cross-sections A , B , and C and for the interface warping functions at $x=4m$ and $x=10m$. Fig. 3-13(b) presents the distributions of the angle of twist and displacement v along the beam length corresponding to point Q in Fig. 3-13(a). The present beam element model (total 113 DOFs) with the proposed warping displacement model gives an angle of twist very close to that of the reference shell element model (total 805 DOFs). The figure shows that

the transverse displacement of the present beam element model is also correctly calculated, because, in the beam element formulation, warping is fully coupled with stretching, shearing, and bending.

In Fig. 3-13(b), we also present the results when the continuity of warping is not properly considered. In the beam element models - I and II, only one warping function (the free warping function) and the corresponding warping DOF are employed. In the beam element model - I, the warping displacement field is not continuous at the interface cross-sections. Therefore, two independent warping DOFs are used at the interface cross-sections. In the beam element model - II, the warping DOFs are shared at the interface cross-section. Note that these two models are only available in most commercial FE software to consider the continuity of warping. Fig. 3-13(b) demonstrates the importance of the proper modeling of warping displacements. In particular, the displacement v could be incorrectly approximated when the modeling of warping displacements is not proper.

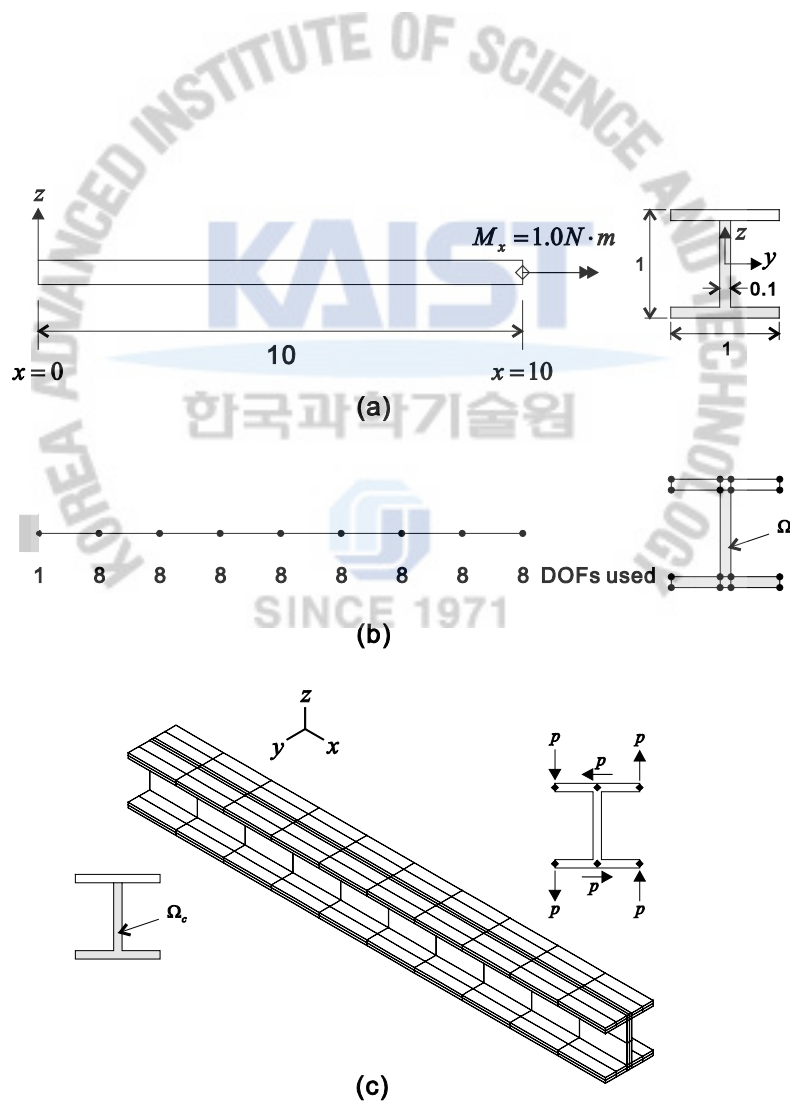


Figure 3-14. Partially constrained warping problem. (a) Problem description (unit: m), (b) Beam element model, cross-sectional mesh used, constrained warping area (shaded area) and the numbers of the nodal DOFs used, (c) Solid element model used.

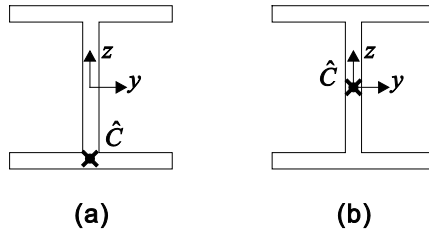


Figure 3-15. Twisting centers in the partially constrained warping problem. (a) $(\lambda_y, \lambda_z) = (0, -0.4369)$ for the interface warping function at $x = 0m$, (b) $(\lambda_y, \lambda_z) = (0, 0)$ for the free warping function.

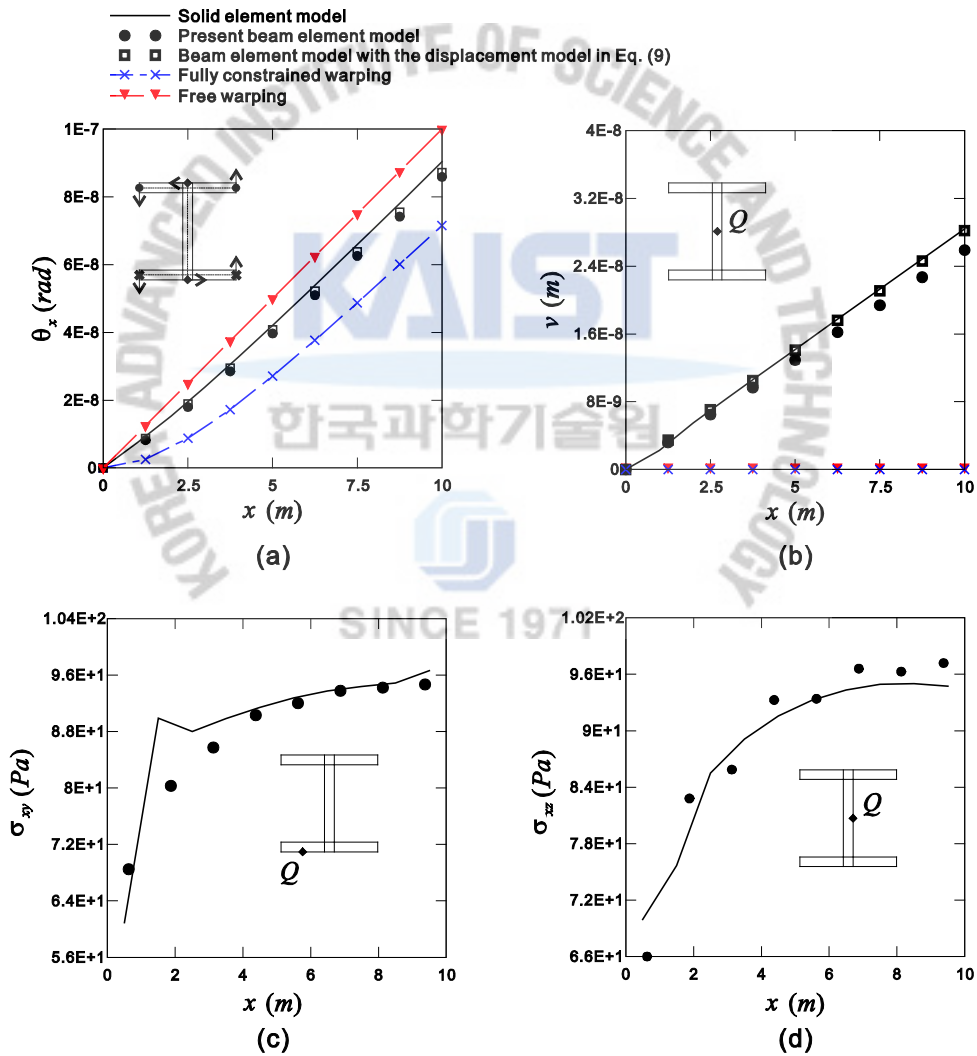


Figure 3-16. Numerical results of the partially constrained warping problem. (a) Angle of twist, (b) Displacement v at Q , (c) Shear stress σ_{xy} at Q , (d) Shear stress σ_{xz} at Q .

3.3.3 Partially Constrained Warping Problem

We consider a wide flange beam problem with a partially constrained warping condition as shown in Fig. 3-14 (a). At $x = 0m$, all displacements including warping are constrained only at the shaded area Ω_c in Figs. 3-14(a) and (b), and torsional moment $M_x = 1.0N \cdot m$ is applied at $x = 10m$.

The beam finite element model is shown in Fig. 3-14(b). The wide flange cross-section is discretized by seven four-node linear cross-sectional elements, and has a partially constrained interface at $x = 0m$. The beam is modeled by eight beam elements with eight nodal DOFs $[u \ v \ w \ \theta_x \ \theta_y \ \theta_z \ \alpha \ \beta_L]^T$. The interface warping DOF β_R is set to zero owing to the free interface at $x = 10m$. The boundary condition $u = v = w = \theta_x = \theta_y = \theta_z = \alpha = 0$ is applied at $x = 0m$. The numbers of the nodal DOFs used are presented in Fig. 3-14(b).

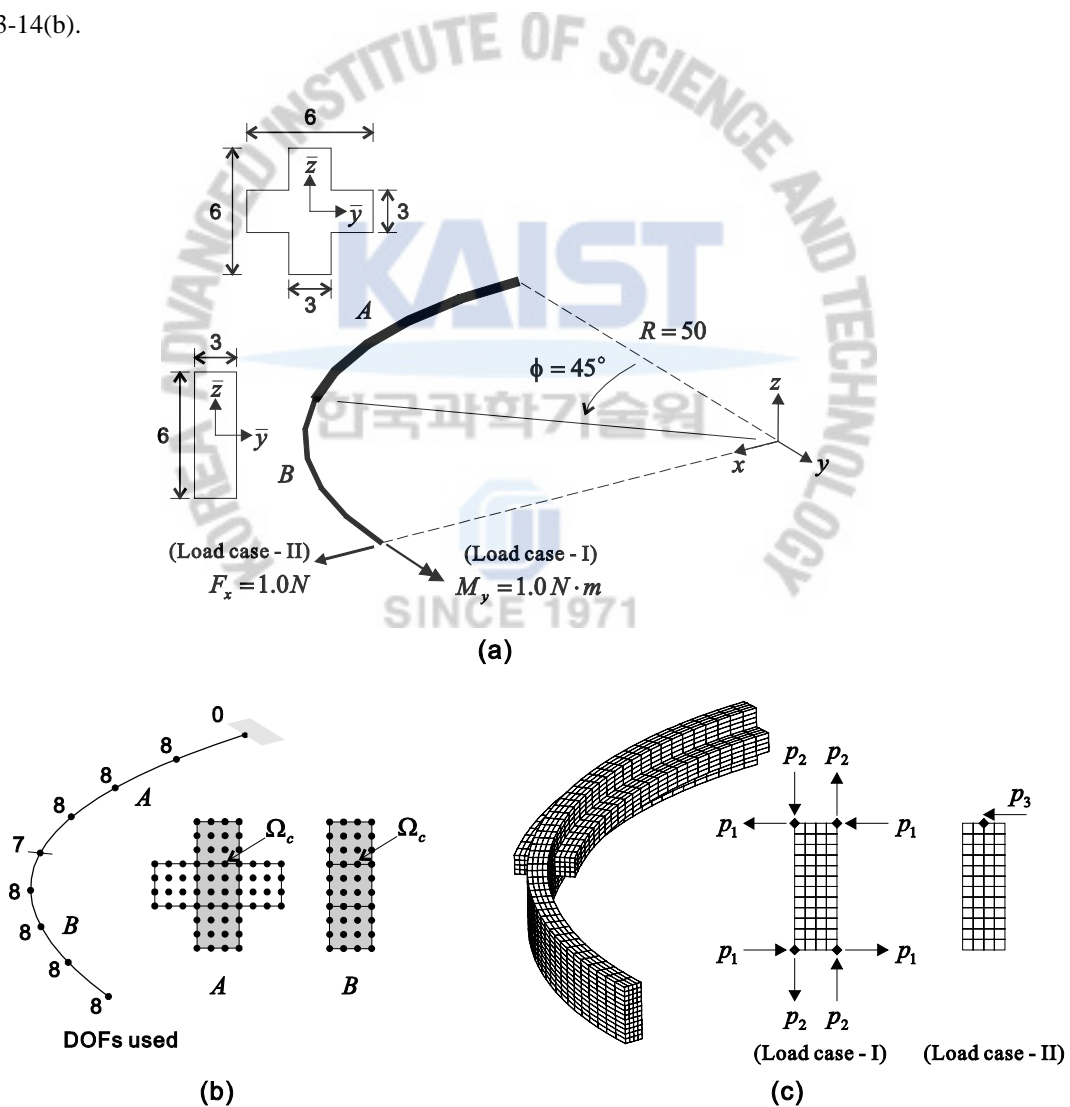


Figure 3-17. Curved beam problem. (a) Problem description (unit: m), (b) Beam element model, cross-sectional meshes used and the numbers of nodal DOFs used, (c) Solid element model used ($p_1 = 0.041667N$, $p_2 = 0.125N$, $p_3 = 1.0N$).

27-node solid finite elements are used to obtain reference solutions, see Fig. 3-14(c). Point loads ($p = 1/3N$) are applied in the solid element model for the equivalent torsional moment $M_x = 1.0N \cdot m$, and all DOFs corresponding to the shaded area Ω_c are fixed at $x = 0m$.

Fig. 3-15 shows the positions of the twisting centers for the interface warping function at $x = 0m$ and the free warping function of the wide flange cross-section. Fig. 3-16 presents the angle of twist, displacement v , and transverse shear stresses σ_{xy} and σ_{xz} at point Q along the beam length. The results of the beam element model (total 65 DOFs) with the proposed warping displacement model are compared with those the reference solid element model (total 8,880 DOFs) and the beam element model (total 174 DOFs) with the warping displacement model in Eq. (2-13), which uses 16 warping DOFs at each beam node in this beam problem.

The results of the two beam element models show good agreement with the reference solution calculated by the solid element model. The numbers of DOFs used show the effectiveness of the present beam model. We show the results for free and fully constrained warping cases. As expected, the angle of twist of the partially constrained case exists between those of both cases. While the displacement v of the free and fully constrained warping cases is zero, the partially constrained warping case results in non-zero displacement v . This indicates that the twisting centers are properly considered in the present warping displacement model.

3.3.4 Curved Beam Problem with a Discontinuously Varying Cross-section

We consider a curved beam problem with discontinuously varying cross-sections: from the cross-shaped cross-section A to the rectangular cross-section B as shown in Fig. 3-17(a).

The cross-section discontinuously varies from A to B at $\varphi = 45^\circ$. All displacements including warping are constrained at $\varphi = 0^\circ$ and two load cases are considered:

- (Load case - I) A torsional moment $M_y = 1.0N \cdot m$ is applied at $\varphi = 90^\circ$.
- (Load case - II) An eccentric shear force $F_x = 1.0N$ is applied at $\varphi = 90^\circ$.

As shown in Fig. 3-17(b), the cross-sections A and B are discretized by 16-node cubic cross-sectional elements with an interconnected domain Ω_c at $\varphi = 45^\circ$. Beam region A is modeled by four beam elements with eight nodal DOFs $[u \ v \ w \ \theta_x \ \theta_y \ \theta_z \ \alpha^{(A)} \ \beta_R^{(A)}]^T$. The interface warping DOF $\beta_L^{(A)}$ is set to zero due to the fully constrained interface at $\varphi = 0^\circ$. Beam region B is modeled by four beam elements with eight nodal DOFs $[u \ v \ w \ \theta_x \ \theta_y \ \theta_z \ \alpha^{(B)} \ \beta_L^{(B)}]^T$. The interface warping DOF $\beta_R^{(B)}$ is set to zero due to the free interface at $\varphi = 90^\circ$. The continuity of the warping displacement is ensured by the condition

$\beta_R^{(A)} = \beta_L^{(B)}$ at $\varphi = 45^\circ$. The boundary condition $u = v = w = \theta_x = \theta_y = \theta_z = \alpha^{(A)} = \beta_R^{(A)} = 0$ is used at $\varphi = 0^\circ$. The numbers of the nodal DOFs used are presented in Fig. 3-17(b).

To obtain the reference solutions, 27-node solid elements are used, as shown in Fig. 3-17(c). In the solid element model, point loads ($p_1 = 0.041667N$ and $p_2 = 0.125N$) are applied for load case - I and a point load ($p_3 = 1.0N$) is applied for load case - II at $\varphi = 90^\circ$. All DOFs are fixed at $\varphi = 0^\circ$.

Fig. 3-18 shows the angle of twist and displacement v at point Q along the beam length. The results of the beam element model (total 69 DOFs) with the proposed warping displacement model show good agreement with those of the reference solid element model (total 85,536 DOFs). It is very difficult to calculate the response of this curved beam problem accurately without properly considering the flexure-torsion coupling effect.

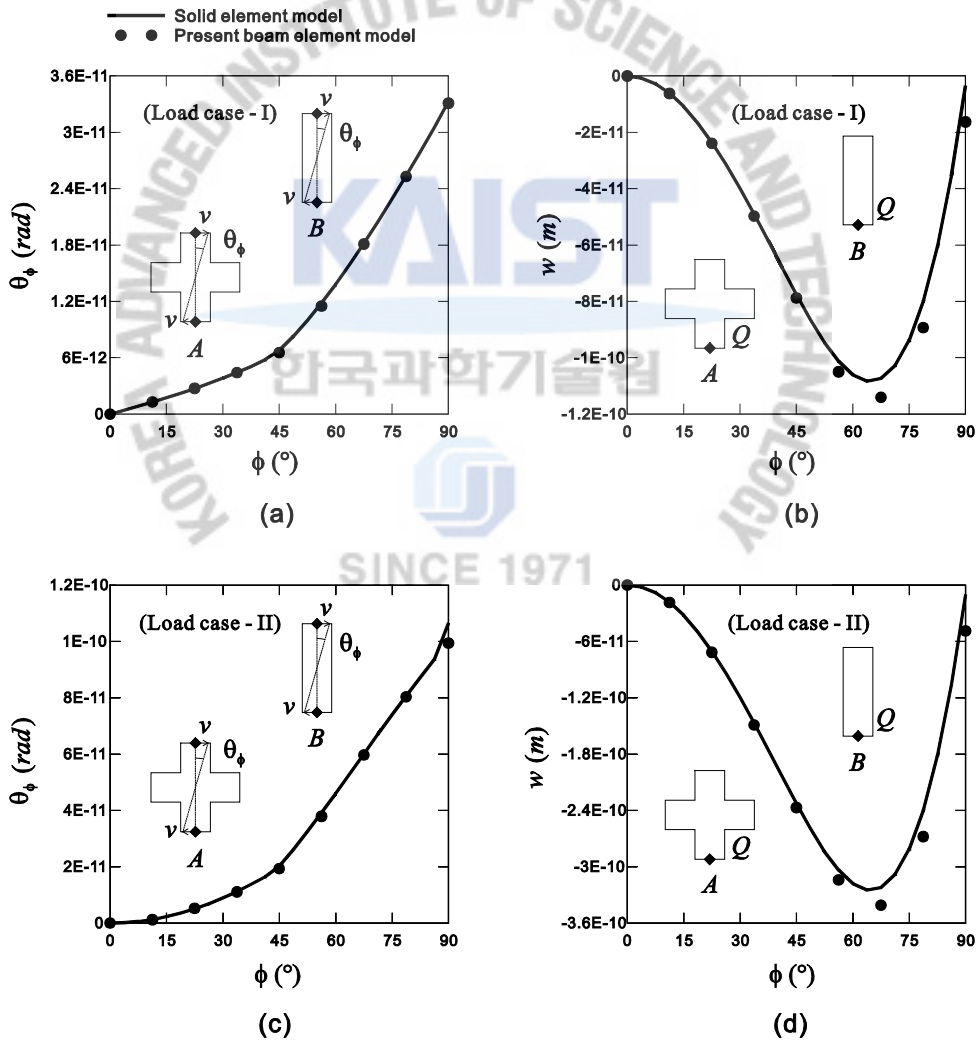


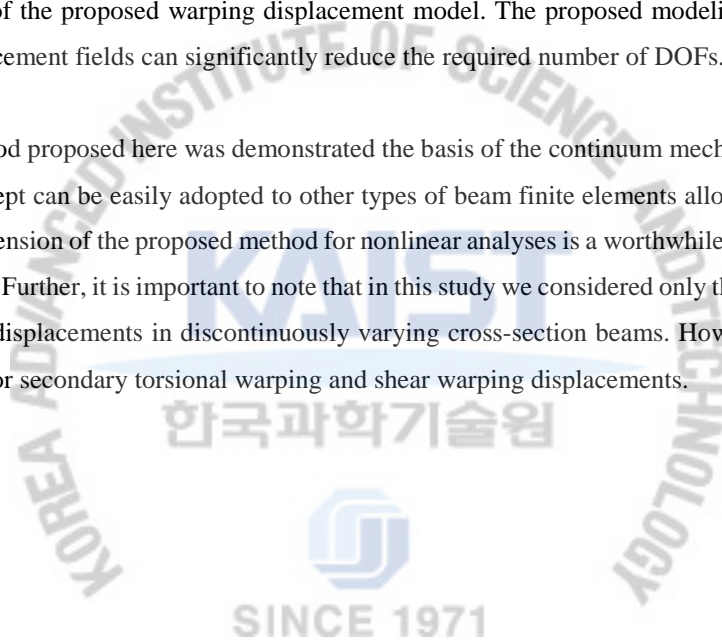
Figure 3-18. Numerical results of the curved beam problem along the beam length. (a) Angle of twist θ_ϕ for the load case - I, (b) Displacement w for the load case - I, (c) Angle of twist θ_ϕ for the load case - II, (d) Displacement w for the load case - II.

3.4 Concluding Remarks

In this chapter, we proposed a new modeling method to construct continuous warping displacement fields for beams with discontinuously varying arbitrary cross-sections. The warping displacement is represented by a combination of three basis warping functions (one free warping function and two interface warping functions) accompanying the corresponding three warping DOFs that are interpolated along the beam length. We also introduced a new numerical method that calculates the free warping functions and the twisting centers simultaneously. Using this method and Lagrange multipliers, a set of coupled equations was formulated to obtain interface warping functions.

All of the methods proposed in this study can be generally used for beams with arbitrary cross-sections including solid and thin and thick-walled cross-sections. We presented three numerical examples to show the feasibility and effectiveness of the proposed warping displacement model. The proposed modeling method to construct the warping displacement fields can significantly reduce the required number of DOFs.

Although the method proposed here was demonstrated the basis of the continuum mechanics based beam finite elements, the concept can be easily adopted to other types of beam finite elements allowing warping displacements. A direct extension of the proposed method for nonlinear analyses is a worthwhile topic for future studies, as in Refs. [25-27]. Further, it is important to note that in this study we considered only the continuity of primary torsional warping displacements in discontinuously varying cross-section beams. However, the same method can be employed for secondary torsional warping and shear warping displacements.



Chapter 4. General Nonlinear Formulation of Continuum Mechanics Based Beam

In this chapter, we present a geometric and material nonlinear formulation of continuum mechanics based beam elements, in which fully coupled 3-D behaviors among stretching, bending, shearing, twisting and warping are considered [52].

4.1 Large displacement kinematics

The continuum mechanics based beam elements are degenerated from assemblages of 3D solid finite elements [50]. In this section, the large displacement kinematics of the continuum mechanics based beams is presented. In the following formulations, a superscript (or subscript) t is employed to denote time; however, in the static nonlinear analyses considered in this study, t is a dummy variable that indicates the load levels and incremental variables rather than the actual time as in dynamic analyses [3].

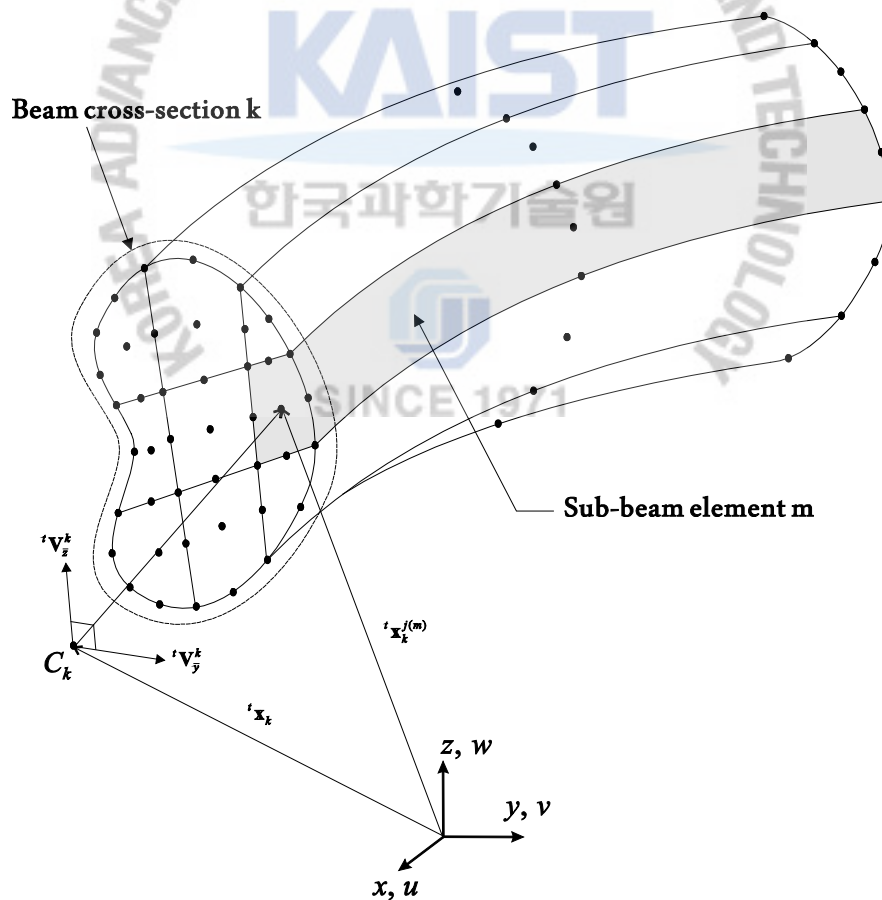


Figure 4-1. A 3-node continuum mechanics based beam element with cross-sectional discretization in the configuration at time t . In this figure, the continuum mechanics based beam element consists of 9 sub-beams.

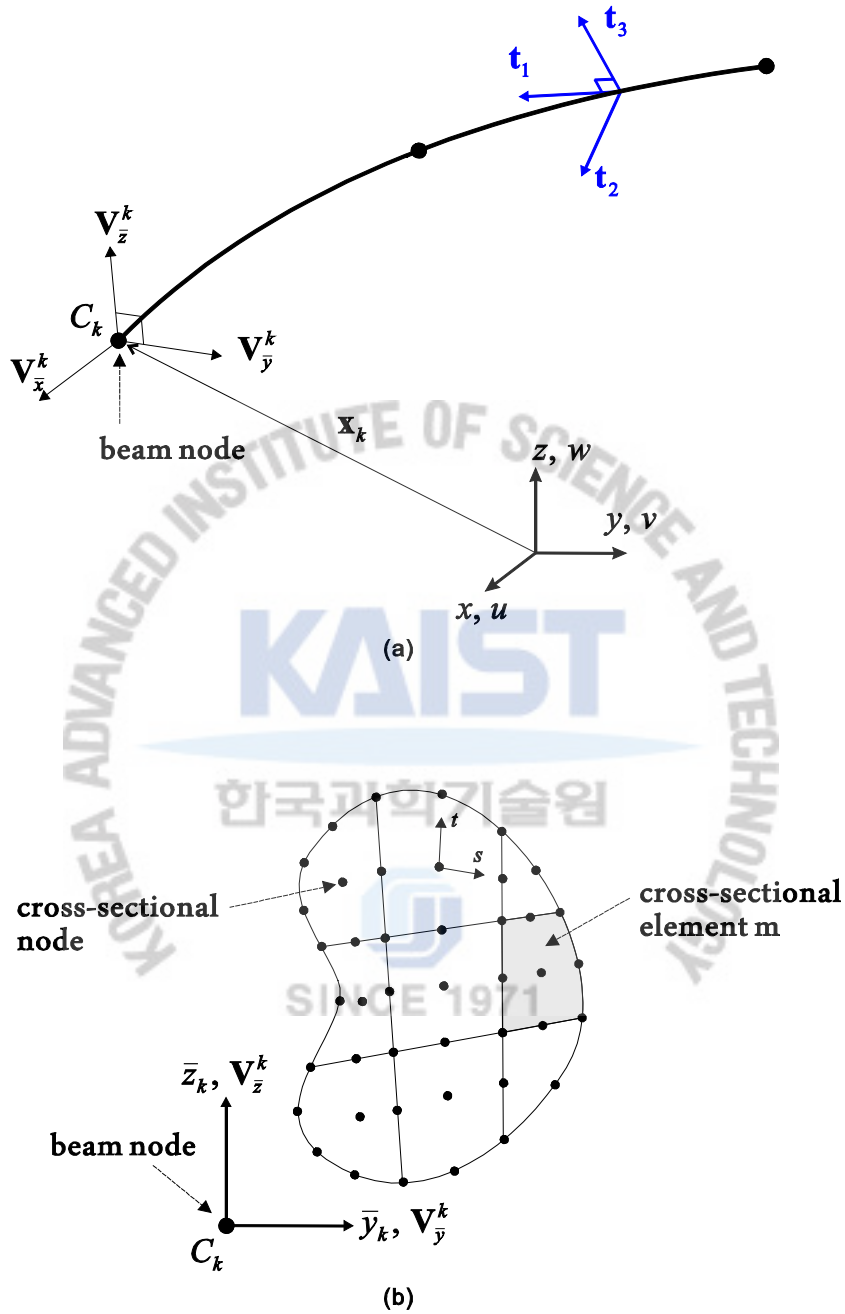


Figure 4-2. A continuum mechanics based beam element: (a) beam nodes and coordinate systems used in the beam element and (b) cross-sectional nodes and elements in the cross-sectional mesh.

Consider a q -node continuum mechanics based beam element that consists of n sub-beams in the configuration at time t , as depicted in Fig. 4-1. Allowing warping displacements, the geometry interpolation of the sub-beam m (shaded in Fig. 1) is given by

$${}^t \mathbf{x}^{(m)} = \sum_{k=1}^q h_k(r) {}^t \mathbf{x}_k + \sum_{k=1}^q h_k(r) \bar{y}_k^{(m)} {}^t \mathbf{V}_{\bar{y}}^k + \sum_{k=1}^q h_k(r) \bar{z}_k^{(m)} {}^t \mathbf{V}_{\bar{z}}^k + \sum_{k=1}^q h_k(r) f_k^{(m)} {}^t \alpha_k {}^t \mathbf{V}_{\bar{x}}^k, \quad (4-1)$$

in which ${}^t \mathbf{x}^{(m)}$ is the material position vector at time t , $h_k(r)$ is the 1D shape function at beam node k , ${}^t \mathbf{x}_k$ is the position of beam node k at time t , ${}^t \mathbf{V}_{\bar{x}}^k$, ${}^t \mathbf{V}_{\bar{y}}^k$, and ${}^t \mathbf{V}_{\bar{z}}^k$ are the unit director vectors at time t and are normal to each other, $\bar{y}_k^{(m)}$ and $\bar{z}_k^{(m)}$ denote the position in the beam cross-section at beam node k , $f_k^{(m)}$ is the warping function at beam node k , and ${}^t \alpha_k$ is the corresponding warping degree of freedom at beam node k at time t ; see Refs. [50, 51] for the detailed derivation of Eq. (4-1). Note that this type of warping model has an intrinsic drawback, that is, the inter-elemental continuity of warping cannot be properly satisfied at nodes where multiple elements are connected and an angle between adjacent elements is not small, see Ref. [53] and therein.

In the continuum mechanics based beam element, a beam cross-section is modeled using a cross-sectional mesh, which is defined using cross-sectional nodes and elements, as seen in Fig. 4-2. Considering the p -node cross-sectional element m (shaded in Fig. 4-2) that corresponds to the sub-beam m , the position and warping functions at beam node k are given by

$$\bar{y}_k^{(m)} = \sum_{j=1}^p h_j(s,t) \bar{y}_k^{j(m)}, \quad \bar{z}_k^{(m)} = \sum_{j=1}^p h_j(s,t) \bar{z}_k^{j(m)}, \quad f_k^{(m)} = \sum_{j=1}^p h_j(s,t) f_k^{j(m)}, \quad (4-2)$$

where $h_j(s,t)$ is the 2D shape function, $\bar{y}_k^{j(m)}$ and $\bar{z}_k^{j(m)}$ denote the position of the cross-sectional node j , and $f_k^{j(m)}$ is the warping value at cross-sectional node j . Note that the number of cross-sectional elements is equal to the number of sub-beams.

In order to represent the material position in the beam cross-section at beam node k , the cross-sectional Cartesian coordinate system is defined using the director vectors ${}^t \mathbf{V}_{\bar{y}}^k$ and ${}^t \mathbf{V}_{\bar{z}}^k$, and the origin C_k . Note that the position of beam node k , ${}^t \mathbf{x}_k$ is located at the origin C_k . The warping director ${}^t \mathbf{V}_{\bar{x}}^k$ in Eq. (4-1) denotes the warping direction at beam node k at time t and is calculated using ${}^t \mathbf{V}_{\bar{x}}^k = {}^t \mathbf{V}_{\bar{y}}^k \times {}^t \mathbf{V}_{\bar{z}}^k$. The warping values are pre-calculated through solving the St. Venant equations using the finite element procedure with the given cross-sectional meshes, see Refs. [50, 51] for more detailed discussions of this method.

For the sub-beam m , the incremental displacement is obtained from the configurations at time t and $t + \Delta t$, as follows

$${}_0 \mathbf{u}^{(m)} = {}^{t+\Delta t} \mathbf{x}^{(m)} - {}^t \mathbf{x}^{(m)}. \quad (4-3)$$

Using Eq. (4-1) in Eq. (4-3), the interpolation of the incremental displacement is obtained by

$$\begin{aligned} {}_0\mathbf{u}^{(m)} = & \sum_{k=1}^q h_k(r) {}_0\mathbf{u}_k + \sum_{k=1}^q h_k(r) \bar{y}_k^{(m)} ({}^{t+\Delta t}\mathbf{V}_{\bar{y}}^k - {}^t\mathbf{V}_{\bar{y}}^k) + \sum_{k=1}^q h_k(r) \bar{z}_k^{(m)} ({}^{t+\Delta t}\mathbf{V}_{\bar{z}}^k - {}^t\mathbf{V}_{\bar{z}}^k) \\ & + \sum_{k=1}^q h_k(r) f_k^{(m)} ({}^{t+\Delta t}\alpha_k {}^{t+\Delta t}\mathbf{V}_{\bar{x}}^k - {}^t\alpha_k {}^t\mathbf{V}_{\bar{x}}^k), \end{aligned} \quad (4-4)$$

4)

where ${}_0\mathbf{u}_k$ is the incremental nodal displacement at beam node k from time t to $t + \Delta t$.

For the parametrization of finite rotations [54-57], the well-known Rodrigues formula is used, as follows

$$\mathbf{R}({}_0\boldsymbol{\theta}^k) = \mathbf{I} + \frac{\sin {}_0\theta^k}{{}_0\theta^k} \hat{\mathbf{R}}({}_0\boldsymbol{\theta}^k) + \frac{1 - \cos {}_0\theta^k}{{}_0\theta^{k2}} \hat{\mathbf{R}}({}_0\boldsymbol{\theta}^k)^2 \quad (4-5)$$

with ${}_0\boldsymbol{\theta}^k = [{}_0\theta_x^k \quad {}_0\theta_y^k \quad {}_0\theta_z^k]^T$, ${}_0\theta^k = \sqrt{{}_0\theta_x^{k2} + {}_0\theta_y^{k2} + {}_0\theta_z^{k2}}$,

$$\hat{\mathbf{R}}({}_0\boldsymbol{\theta}^k) = \begin{bmatrix} 0 & -{}_0\theta_z^k & {}_0\theta_y^k \\ {}_0\theta_z^k & 0 & -{}_0\theta_x^k \\ -{}_0\theta_y^k & {}_0\theta_x^k & 0 \end{bmatrix}, \quad (4-6)$$

where ${}_0\theta_x^k$, ${}_0\theta_y^k$, and ${}_0\theta_z^k$ are the incremental Eulerian angles from time t to $t + \Delta t$, and $\hat{\mathbf{R}}$ is the skew-symmetric matrix operator.

Then, the director vectors at time $t + \Delta t$ are defined as

$${}^{t+\Delta t}\mathbf{V}_{\bar{x}}^k = \mathbf{R}({}_0\boldsymbol{\theta}^k) {}^t\mathbf{V}_{\bar{x}}^k, \quad {}^{t+\Delta t}\mathbf{V}_{\bar{y}}^k = \mathbf{R}({}_0\boldsymbol{\theta}^k) {}^t\mathbf{V}_{\bar{y}}^k, \quad \text{and} \quad {}^{t+\Delta t}\mathbf{V}_{\bar{z}}^k = \mathbf{R}({}_0\boldsymbol{\theta}^k) {}^t\mathbf{V}_{\bar{z}}^k. \quad (4-7)$$

Using Eq. (4-7) in Eq. (4-4), we can obtain the following

$$\begin{aligned} {}_0\mathbf{u}^{(m)} = & \sum_{k=1}^q h_k(r) {}_0\mathbf{u}_k + \sum_{k=1}^q h_k(r) \bar{y}_k^{(m)} (\mathbf{R}({}_0\boldsymbol{\theta}^k) - \mathbf{I}) {}^t\mathbf{V}_{\bar{y}}^k + \sum_{k=1}^q h_k(r) \bar{z}_k^{(m)} (\mathbf{R}({}_0\boldsymbol{\theta}^k) - \mathbf{I}) {}^t\mathbf{V}_{\bar{z}}^k \\ & + \sum_{k=1}^q h_k(r) f_k^{(m)} ({}_0\alpha_k \mathbf{R}({}_0\boldsymbol{\theta}^k) + {}^t\alpha_k (\mathbf{R}({}_0\boldsymbol{\theta}^k) - \mathbf{I})) {}^t\mathbf{V}_{\bar{x}}^k, \end{aligned} \quad (4-8)$$

in which ${}_0\alpha_k$ is the incremental warping degree of freedom at beam node k .

Applying the Taylor expansion to Eq. (4-5), the finite rotation tensor $\mathbf{R}({}_0\boldsymbol{\theta}^k)$ can be represented using a polynomial function with respect to the incremental Eulerian angle vector ${}_0\boldsymbol{\theta}^k$

$$\mathbf{R}({}_0\boldsymbol{\theta}^k) = \mathbf{I} + \hat{\mathbf{R}}({}_0\boldsymbol{\theta}^k) + \frac{1}{2!} \hat{\mathbf{R}}({}_0\boldsymbol{\theta}^k)^2 + \frac{1}{3!} \hat{\mathbf{R}}({}_0\boldsymbol{\theta}^k)^3 + \frac{1}{4!} \hat{\mathbf{R}}({}_0\boldsymbol{\theta}^k)^4 + \dots \quad (4-9)$$

Substituting Eq. (4-9) into Eq. (4-8) and using the second order approximation for the finite rotation, the incremental displacement in Eq. (4-8) becomes

$${}_0\mathbf{u}^{(m)} \approx {}_0\mathbf{u}_1^{(m)} + {}_0\mathbf{u}_2^{(m)} \quad (4-10)$$

with

$$\begin{aligned}
{}_0\mathbf{u}_1^{(m)} &= \sum_{k=1}^q h_k(r) {}_0\mathbf{u}_k + \sum_{k=1}^q h_k(r) \bar{y}_k^{(m)} \hat{\mathbf{R}}({}_0\boldsymbol{\theta}^k) {}^t\mathbf{V}_{\bar{y}}^k + \sum_{k=1}^q h_k(r) \bar{z}_k^{(m)} \hat{\mathbf{R}}({}_0\boldsymbol{\theta}^k) {}^t\mathbf{V}_{\bar{z}}^k \\
&+ \sum_{k=1}^q h_k(r) f_k^{(m)} [{}_0\alpha_k \mathbf{I} + {}^t\alpha_k \hat{\mathbf{R}}({}_0\boldsymbol{\theta}^k)] {}^t\mathbf{V}_{\bar{x}}^k, \tag{4-11}
\end{aligned}$$

$$\begin{aligned}
{}_0\mathbf{u}_2^{(m)} &= \frac{1}{2} \sum_{k=1}^q h_k(r) \bar{y}_k^{(m)} \hat{\mathbf{R}}({}_0\boldsymbol{\theta}^k) {}^2 {}^t\mathbf{V}_{\bar{y}}^k + \frac{1}{2} \sum_{k=1}^q h_k(r) \bar{z}_k^{(m)} \hat{\mathbf{R}}({}_0\boldsymbol{\theta}^k) {}^2 {}^t\mathbf{V}_{\bar{z}}^k \\
&+ \sum_{k=1}^q h_k(r) f_k^{(m)} [{}_0\alpha_k \hat{\mathbf{R}}({}_0\boldsymbol{\theta}^k) + \frac{1}{2} {}^t\alpha_k \hat{\mathbf{R}}({}_0\boldsymbol{\theta}^k) {}^2] {}^t\mathbf{V}_{\bar{x}}^k, \tag{4-12}
\end{aligned}$$

in which ${}_0\mathbf{u}_1^{(m)}$ and ${}_0\mathbf{u}_2^{(m)}$ are the linear and quadratic parts, respectively, in the incremental displacement.

In the incremental displacement in Eq. (4-10), seven DOFs (three translations, three rotations, and one warping DOF) are employed at beam node k using the nodal DOFs vector:

$${}_0\mathbf{U}_k = [{}_0u_k \quad {}_0v_k \quad {}_0w_k \mid {}_0\theta_x^k \quad {}_0\theta_y^k \quad {}_0\theta_z^k \mid {}_0\alpha_k]^T, \tag{4-13}$$

and the DOFs vector of the q -node beam element is as follows

$${}_0\mathbf{U} = [{}_0\mathbf{U}_1^T \quad {}_0\mathbf{U}_2^T \quad \dots \quad {}_0\mathbf{U}_q^T]^T. \tag{4-14}$$

Then, ${}_0\mathbf{u}_1^{(m)}$ is represented in terms of the nodal DOFs vector

$${}_0\mathbf{u}_1^{(m)} = [{}^{\mathbf{L}}_1^{(m)} \quad {}^{\mathbf{L}}_2^{(m)} \quad \dots \quad {}^{\mathbf{L}}_q^{(m)}] {}_0\mathbf{U} = {}^{\mathbf{L}}_0^{(m)} {}_0\mathbf{U} \tag{4-15}$$

with

$${}^{\mathbf{L}}_k^{(m)} = h_k(r) \left[\mathbf{I} - \left(\bar{y}_k^{(m)} \hat{\mathbf{R}}({}^t\mathbf{V}_{\bar{y}}^k) + \bar{z}_k^{(m)} \hat{\mathbf{R}}({}^t\mathbf{V}_{\bar{z}}^k) + f_k^{(m)} {}^t\alpha_k \hat{\mathbf{R}}({}^t\mathbf{V}_{\bar{x}}^k) \right) f_k^{(m)}(s, t) {}^t\mathbf{V}_{\bar{x}}^k \right]. \tag{4-16}$$

Also, ${}_0\mathbf{u}_2^{(m)}$ is given by

$${}_0\mathbf{u}_2^{(m)} = \begin{bmatrix} {}_0u_2^{(m)} \\ {}_0v_2^{(m)} \\ {}_0w_2^{(m)} \end{bmatrix} = \frac{1}{2} \begin{bmatrix} {}_0\mathbf{U}_1^T \mathbf{Q}_1^{(m)} {}_0\mathbf{U} \\ {}_0\mathbf{U}_2^T \mathbf{Q}_2^{(m)} {}_0\mathbf{U} \\ {}_0\mathbf{U}_3^T \mathbf{Q}_3^{(m)} {}_0\mathbf{U} \end{bmatrix} \tag{4-17}$$

$$\text{with } {}_i\mathbf{Q}^{(m)} = [{}_i\mathbf{Q}_1^{(m)} \quad {}_i\mathbf{Q}_2^{(m)} \quad \dots \quad {}_i\mathbf{Q}_q^{(m)}], \quad i = 1, 2, 3, \tag{4-18}$$

in which

$${}_i\mathbf{Q}_k^{(m)} = h_k(r) \begin{bmatrix} \mathbf{0} & \mathbf{0} & \mathbf{0} \\ \mathbf{0} & \bar{y}_k^{(m)} \boldsymbol{\Psi}_i({}^t\mathbf{V}_{\bar{y}}^k) + \bar{z}_k^{(m)} \boldsymbol{\Psi}_i({}^t\mathbf{V}_{\bar{z}}^k) + f_k^{(m)} {}^t\alpha_k \boldsymbol{\Psi}_i({}^t\mathbf{V}_{\bar{x}}^k) & -f_k^{(m)} \hat{\mathbf{R}}_i({}^t\mathbf{V}_{\bar{x}}^k) \\ \mathbf{0} & -f_k^{(m)} \hat{\mathbf{R}}_i({}^t\mathbf{V}_{\bar{x}}^k) & \mathbf{0} \end{bmatrix} \tag{4-19}$$

with

$$\boldsymbol{\Psi}_1(\mathbf{x}) = \frac{1}{2} \begin{bmatrix} 0 & x_2 & x_3 \\ x_2 & -2x_1 & 0 \\ x_3 & 0 & -2x_1 \end{bmatrix}, \quad \boldsymbol{\Psi}_2(\mathbf{x}) = \frac{1}{2} \begin{bmatrix} -2x_2 & x_1 & 0 \\ x_1 & 0 & x_3 \\ 0 & x_3 & -2x_2 \end{bmatrix}, \quad \boldsymbol{\Psi}_3(\mathbf{x}) = \frac{1}{2} \begin{bmatrix} -2x_3 & 0 & x_1 \\ 0 & -2x_3 & x_2 \\ x_1 & x_2 & 0 \end{bmatrix}, \tag{4-20}$$

$$\text{and } \hat{\mathbf{R}}_1(\mathbf{x}) = [0 \quad -x_3 \quad x_2], \hat{\mathbf{R}}_2(\mathbf{x}) = [x_3 \quad 0 \quad -x_1], \text{ and } \hat{\mathbf{R}}_3(\mathbf{x}) = [-x_2 \quad x_1 \quad 0]. \quad (4-21)$$

The variations of the incremental displacements are given by:

$$\delta_0 \mathbf{u}_1^{(m)} = \mathbf{L}^{(m)} \delta_0 \mathbf{U} \quad \text{and} \quad \delta_0 \mathbf{u}_2^{(m)} = \begin{bmatrix} \delta_0 u_2^{(m)} \\ \delta_0 v_2^{(m)} \\ \delta_0 w_2^{(m)} \end{bmatrix} = \begin{bmatrix} \delta_0 \mathbf{U}^T \mathbf{Q}^{(m)} \mathbf{U} \\ \delta_0 \mathbf{U}^T \mathbf{Q}^{(m)} \mathbf{U} \\ \delta_0 \mathbf{U}^T \mathbf{Q}^{(m)} \mathbf{U} \end{bmatrix}. \quad (4-22)$$

4.2 Green-Lagrange strain

The covariant Green-Lagrange strain tensor ${}^t \mathcal{E}_{ij}^{(m)}$ for the sub-beam m at the configuration at time t , referred to the configuration at time 0 , is defined as follows

$${}^t \mathcal{E}_{ij}^{(m)} = \frac{1}{2} ({}^t \mathbf{g}_i^{(m)} \cdot {}^t \mathbf{g}_j^{(m)} - {}^0 \mathbf{g}_i^{(m)} \cdot {}^0 \mathbf{g}_j^{(m)}) \quad \text{with} \quad {}^t \mathbf{g}_i^{(m)} = \frac{\partial {}^t \mathbf{x}^{(m)}}{\partial r_i}, \quad (4-23)$$

in which $r_1 = 1$, $r_2 = 2$, and $r_3 = 3$. Since cross-sectional deformations are not allowed in Timoshenko beam theory, in the beam formulation, only five strain components (${}^t \mathcal{E}_{11}^{(m)}$, ${}^t \mathcal{E}_{12}^{(m)}$, ${}^t \mathcal{E}_{21}^{(m)}$, ${}^t \mathcal{E}_{13}^{(m)}$, and ${}^t \mathcal{E}_{31}^{(m)}$) are considered; that is, $(i, j) \in \{(1,1), (1,2), (2,1), (1,3), (3,1)\}$. The other strain components (${}^t \mathcal{E}_{22}^{(m)}$, ${}^t \mathcal{E}_{33}^{(m)}$, ${}^t \mathcal{E}_{23}^{(m)}$, and ${}^t \mathcal{E}_{32}^{(m)}$) are zero. It is important to note that, when the covariant base vector ${}^t \mathbf{g}_i^{(m)}$ is calculated, the warping effect in the geometry interpolation in Eq. (4-1) should be considered. Otherwise, the Wagner strain term cannot be correctly included in the beam formulation, see Appendix A.

The local Green-Lagrange strain tensor ${}^t \bar{\mathcal{E}}_{ij}^{(m)}$ defined in the local Cartesian coordinate system in Fig. 4-2(a) is calculated using the following equation:

$${}^t \bar{\mathcal{E}}_{ij}^{(m)} ({}^0 \mathbf{t}_i \otimes {}^0 \mathbf{t}_j) = {}^t \bar{\mathcal{E}}_{kl}^{(m)} ({}^0 \mathbf{g}^k \otimes {}^0 \mathbf{g}^l), \quad (4-24)$$

where the base vectors for the local Cartesian coordinate system are given by:

$${}^0 \mathbf{t}_1 = h_k(r) {}^0 \mathbf{V}_{\bar{x}}^k, \quad {}^0 \mathbf{t}_2 = h_k(r) {}^0 \mathbf{V}_{\bar{y}}^k \quad \text{and} \quad {}^0 \mathbf{t}_3 = h_k(r) {}^0 \mathbf{V}_{\bar{z}}^k. \quad (4-25)$$

Here, the five non-zero components in the local Green-Lagrange strain tensor are also considered: ${}^t \bar{\mathcal{E}}_{11}^{(m)}$,

${}^t \bar{\mathcal{E}}_{12}^{(m)}$, ${}^t \bar{\mathcal{E}}_{21}^{(m)}$, ${}^t \bar{\mathcal{E}}_{13}^{(m)}$, and ${}^t \bar{\mathcal{E}}_{31}^{(m)}$. In Eq. (4-24), the contravariant base vectors ${}^0 \mathbf{g}^i$ are calculated using

$${}^0 \mathbf{g}^i \cdot {}^0 \mathbf{g}_j = \delta_j^i, \quad (4-26)$$

in which δ_j^i denotes the Kronecker delta ($\delta_j^i = 1$ if $i = j$, and 0 otherwise).

Substituting Eq. (4-1) into Eq. (4-23), the incremental covariant Green-Lagrange strain for the sub-beam m is derived as follows

$${}^0 \mathcal{E}_{ij}^{(m)} = {}^{t+\Delta t} \mathcal{E}_{ij}^{(m)} - {}^t \mathcal{E}_{ij}^{(m)} = \frac{1}{2} ({}^t \mathbf{g}_j^{(m)} \cdot {}^0 \mathbf{u}_{,i}^{(m)} + {}^t \mathbf{g}_i^{(m)} \cdot {}^0 \mathbf{u}_{,j}^{(m)} + {}^0 \mathbf{u}_{,i}^{(m)} \cdot {}^0 \mathbf{u}_{,j}^{(m)}) \quad \text{with} \quad {}^0 \mathbf{u}_{,i}^{(m)} = \frac{\partial {}^0 \mathbf{u}^{(m)}}{\partial r_i}. \quad (4-27)$$

Retaining only the strain terms up to the quadratic order with respect to the nodal DOFs through substituting Eq. (4-10) into Eq. (4-27), the incremental covariant Green-Lagrange strain can be decomposed into the following equation

$${}_0\boldsymbol{\varepsilon}_{ij}^{(m)} \approx {}_0e_{ij}^{(m)} + {}_0\eta_{ij}^{(m)} + {}_0\kappa_{ij}^{(m)} \quad (4-28)$$

with

$${}_0e_{ij}^{(m)} = \frac{1}{2}({}^t\mathbf{g}_j^{(m)} \cdot {}_0\mathbf{u}_{1,i}^{(m)} + {}^t\mathbf{g}_i^{(m)} \cdot {}_0\mathbf{u}_{1,j}^{(m)}), \quad {}_0\eta_{ij}^{(m)} = \frac{1}{2}{}_0\mathbf{u}_{1,i}^{(m)} \cdot {}_0\mathbf{u}_{1,j}^{(m)} \quad \text{and}$$

$${}_0\kappa_{ij}^{(m)} = \frac{1}{2}({}^t\mathbf{g}_j^{(m)} \cdot {}_0\mathbf{u}_{2,i}^{(m)} + {}^t\mathbf{g}_i^{(m)} \cdot {}_0\mathbf{u}_{2,j}^{(m)}), \quad (4-29)$$

where ${}_0e_{ij}^{(m)}$ and ${}_0\eta_{ij}^{(m)}$ denote the linear and nonlinear terms, respectively, due to the linear incremental displacement ${}_0\mathbf{u}_1^{(m)}$ in Eq. (4-11), and ${}_0\kappa_{ij}^{(m)}$ denotes the nonlinear term that results from the quadratic incremental displacement ${}_0\mathbf{u}_2^{(m)}$ in Eq. (4-12).

Note that Eqs. (4-28) and (4-29) contain all strain terms up to the quadratic order with respect to the nodal DOFs, which therefore leads to a complete expression of the tangent stiffness matrix.

Using Eqs. (4-15) and (4-17) in Eq. (4-29), the following relations between the incremental strains and incremental nodal displacements are obtained

$${}_0e_{ij}^{(m)} = \frac{1}{2}({}^t\mathbf{g}_j^{(m)} \cdot \mathbf{L}_{,i}^{(m)} + {}^t\mathbf{g}_i^{(m)} \cdot \mathbf{L}_{,j}^{(m)})_0 \mathbf{U} = \mathbf{B}_{ij}^{(m)}{}_0 \mathbf{U}, \quad (4-30a)$$

$${}_0\eta_{ij}^{(m)} = \frac{1}{2}{}_0 \mathbf{U}^T (\mathbf{L}_{,i}^{(m)T} \mathbf{L}_{,j}^{(m)})_0 \mathbf{U} = \frac{1}{2}{}_0 \mathbf{U}^T {}_1\mathbf{N}_{ij}^{(m)}{}_0 \mathbf{U}, \quad (4-30b)$$

$${}_0\kappa_{ij}^{(m)} = \frac{1}{2}{}_0 \mathbf{U}^T ({}^t\mathbf{g}_j^{(m)} \hat{\mathbf{Q}}_{,i}^{(m)} + {}^t\mathbf{g}_i^{(m)} \hat{\mathbf{Q}}_{,j}^{(m)})_0 \mathbf{U} = \frac{1}{2}{}_0 \mathbf{U}^T {}_2\mathbf{N}_{ij}^{(m)}{}_0 \mathbf{U}, \quad (4-30c)$$

$$\text{in which } \mathbf{L}_{,i}^{(m)} = \frac{\partial \mathbf{L}^{(m)}}{\partial r_i} \quad \text{and} \quad \hat{\mathbf{Q}}_{,i}^{(m)} = \begin{bmatrix} \frac{\partial {}_1\mathbf{Q}^{(m)}}{\partial r_i} & \frac{\partial {}_2\mathbf{Q}^{(m)}}{\partial r_i} & \frac{\partial {}_3\mathbf{Q}^{(m)}}{\partial r_i} \end{bmatrix}^T. \quad (4-31)$$

Using Eq. (4-24), the incremental covariant Green-Lagrange strains are transformed into the local Green-Lagrange strains, as follows

$${}_0\bar{e}_{ij}^{(m)} = \mathbf{B}_{ij}^{(m)}(\mathbf{t}_i \cdot \mathbf{g}^{k(m)})(\mathbf{t}_j \cdot \mathbf{g}^{l(m)})_0 \mathbf{U} = \bar{\mathbf{B}}_{ij}^{(m)}{}_0 \mathbf{U}, \quad (4-32a)$$

$${}_0\bar{\eta}_{ij}^{(m)} = \frac{1}{2}{}_0 \mathbf{U}^T {}_1\mathbf{N}_{ij}^{(m)}(\mathbf{t}_i \cdot \mathbf{g}^{k(m)})(\mathbf{t}_j \cdot \mathbf{g}^{l(m)})_0 \mathbf{U} = \frac{1}{2}{}_0 \mathbf{U}^T {}_1\bar{\mathbf{N}}_{ij}^{(m)}{}_0 \mathbf{U}, \quad (4-32b)$$

$${}_0\bar{\kappa}_{ij}^{(m)} = \frac{1}{2}{}_0 \mathbf{U}^T {}_2\mathbf{N}_{ij}^{(m)}(\mathbf{t}_i \cdot \mathbf{g}^{k(m)})(\mathbf{t}_j \cdot \mathbf{g}^{l(m)})_0 \mathbf{U} = \frac{1}{2}{}_0 \mathbf{U}^T {}_2\bar{\mathbf{N}}_{ij}^{(m)}{}_0 \mathbf{U}, \quad (4-32c)$$

and their variations are obtained as follows

$$\delta_0 \bar{e}_{ij}^{(m)} = \bar{\mathbf{B}}_{ij}^{(m)} \delta_0 \mathbf{U}, \quad \delta_0 \bar{\eta}_{ij}^{(m)} = \delta_0 \mathbf{U}^T {}_1\bar{\mathbf{N}}_{ij}^{(m)}{}_0 \mathbf{U} \quad \text{and} \quad \delta_0 \bar{\kappa}_{ij}^{(m)} = \delta_0 \mathbf{U}^T {}_2\bar{\mathbf{N}}_{ij}^{(m)}{}_0 \mathbf{U}. \quad (4-33)$$

4.3 Incremental Equilibrium Equation

The general nonlinear response is calculated using incremental equilibrium equations in which, when the configuration at time t is known, the principle of virtual work in the configuration at time $t + \Delta t$ is considered. Based on the total Lagrangian formulation, the tangent stiffness matrix and internal force vector are derived for the incremental equilibrium equations. A single beam element is considered in this derivation because the incremental equilibrium equations for an entire beam finite element model can be easily constructed using the direct stiffness procedure [3].

The total Lagrangian formulation for the continuum mechanics based beam is given by [3, 11]

$$\int_{0V} \bar{C}_{ijkl} \bar{e}_{ij} \delta_0 \bar{e}_{kl} d^0V + \int_{0V} {}^t\bar{S}_{ij} \delta_0 \bar{n}_{ij} d^0V + \int_{0V} {}^t\bar{S}_{ij} \delta_0 \bar{k}_{ij} d^0V = {}^{t+\Delta t}\mathfrak{R} - \int_{0V} {}^t\bar{S}_{ij} \delta_0 \bar{e}_{ij} d^0V, \quad (4-34)$$

in which 0V is the volume of the beam element at time 0 , ${}^{t+\Delta t}\mathfrak{R}$ is the external virtual work including the work due to the applied surface tractions and body forces, and \bar{C}_{ijkl} and ${}^t\bar{S}_{ij}$ denote the material law tensor and second Piola-Kirchhoff stress measured in the local Cartesian coordinate system, respectively.

As mentioned in the previous section, only five strain components (and corresponding stress components) are considered in the beam formulation (i.e. $(i, j) \in \{(1,1), (1,2), (2,1), (1,3), (3,1)\}$) and the material law tensor has only five non-zero components ($\bar{C}_{1111} = E$ and $\bar{C}_{1212} = \bar{C}_{2121} = \bar{C}_{1313} = \bar{C}_{3131} = G$) with Young's modulus E and shear modulus G .

Substituting Eqs. (4-32a), (4-32b), (4-32c), and (4-33) into Eq. (4-34), the following discretized equation is obtained

$$\begin{aligned} & \delta_0 \mathbf{U}^T \left[\sum_{m=1}^n \int_{0V^{(m)}} \bar{\mathbf{B}}_{ij}^{(m)T} \bar{C}_{ijkl} \bar{\mathbf{B}}_{kl}^{(m)} dV^{(m)} + \sum_{m=1}^n \int_{0V^{(m)}} {}_1\bar{\mathbf{N}}_{ij}^{(m)} {}^t\bar{S}_{ij} dV^{(m)} + \sum_{m=1}^n \int_{0V^{(m)}} {}_2\bar{\mathbf{N}}_{ij}^{(m)} {}^t\bar{S}_{ij} dV^{(m)} \right]_0 \mathbf{U} \\ & = \delta_0 \mathbf{U}^T {}^{t+\Delta t} \mathbf{R} - \delta_0 \mathbf{U}^T \left[\sum_{m=1}^n \int_{0V^{(m)}} \bar{\mathbf{B}}_{ij}^{(m)T} {}^t\bar{S}_{ij} dV^{(m)} \right], \end{aligned} \quad (4-35)$$

in which n is the number of sub-beams considered in the continuum mechanics based beam, ${}^0V^{(m)}$ is the volume of the sub-beam m at time 0 , and ${}^0V = \sum_{m=1}^n {}^0V^{(m)}$.

Finally, the linearized incremental equilibrium equations are obtained as follows

$${}^t\mathbf{K}_0 \mathbf{U} = {}^{t+\Delta t} \mathbf{R} - {}^t\mathbf{F} \quad \text{with} \quad {}^t\mathbf{K} = {}^t\mathbf{K}_L + {}^t_1\mathbf{K}_{NL} + {}^t_2\mathbf{K}_{NL}, \quad (4-36)$$

in which

$${}^t\mathbf{K}_L = \sum_{m=1}^n \int_{0V^{(m)}} \bar{\mathbf{B}}_{ij}^{(m)T} \bar{C}_{ijkl} \bar{\mathbf{B}}_{kl}^{(m)} dV^{(m)}, \quad (4-37a)$$

$${}^t_1 \mathbf{K}_{NL} = \sum_{m=1}^n \int_{0V^{(m)}_1} \bar{\mathbf{N}}_{ij}^{(m)T} {}^t_0 \bar{\mathbf{S}}_{ij} dV^{(m)}, \quad (4-37b)$$

$${}^t_2 \mathbf{K}_{NL} = \sum_{m=1}^n \int_{0V^{(m)}_2} \bar{\mathbf{N}}_{ij}^{(m)T} {}^t_0 \bar{\mathbf{S}}_{ij} dV^{(m)}, \quad (4-37c)$$

$${}^t_0 \mathbf{F} = \sum_{m=1}^n \int_{0V^{(m)}} \bar{\mathbf{B}}_{ij}^{(m)T} {}^t_0 \bar{\mathbf{S}}_{ij} dV^{(m)}. \quad (4-37d)$$

Note that, in Eq. (4-36), ${}^{t+\Delta t} \mathbf{R}$ is the external load vector and the tangent stiffness matrix ${}^t \mathbf{K}$ is symmetric and complete.

After solving Eq. (4-36) in each incremental step, the incremental displacement ${}^0 \mathbf{U}$ is obtained. Then, the position of beam node k and the warping degree of freedom at beam node k are additively updated, as follows

$${}^{t+\Delta t} {}^0 \mathbf{x}_k = {}^t {}^0 \mathbf{x}_k + \begin{bmatrix} {}^0 u_k \\ {}^0 v_k \\ {}^0 w_k \end{bmatrix}, \quad \text{and} \quad {}^{t+\Delta t} {}^0 \alpha_k = {}^t {}^0 \alpha_k + {}^0 \alpha_k, \quad (4-38)$$

and the director vectors are multiplicatively updated using Eq. (4-7).

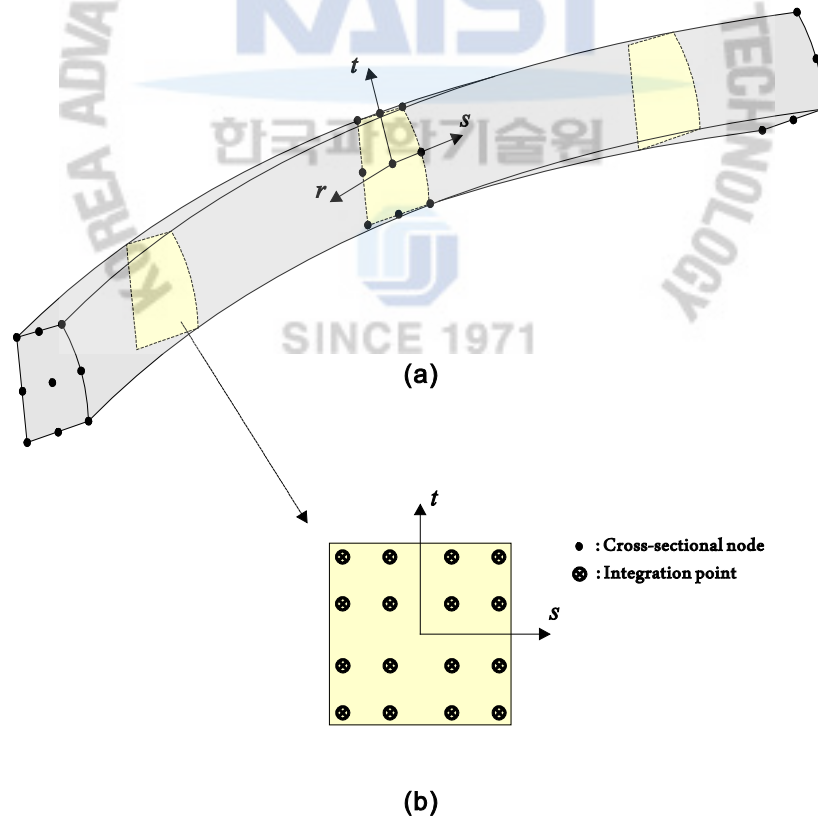


Figure 4-3. Gauss integration points in the sub-beam element m in Fig. 4-1: (a) sub-beam element m and (b) gauss integration points in beam cross-sections.

In order to avoid shear and membrane lockings, the well-known assumed strain scheme, namely the MITC (Mixed Interpolation of Tensorial Components) scheme, is adopted [25, 28]. Note that, compared with the reduced integration scheme, the MITC scheme enables better performance, particularly for complicated beam geometries. Therefore, the full Gauss integration is used to evaluate the stiffness matrices and internal force vector in Eqs. (4-37a), (4-37b), (4-37c), and (4-37d). For example, Fig. 4-3 illustrates the 3, 4, and 4 integration points in the r , s , and t directions, respectively, for the sub-beam element m in Fig. 4-1. That is, 3 integration points for the longitudinal direction and 4×4 integration points in the sub-beam cross-section are used, which will be referred as $3 \times 4 \times 4$ integration in the following sections.

4.4 Elastoplastic Material Model

In order to simulate the material nonlinearity, the three-dimensional von Mises plasticity model with the associated flow rule and linear isotropic hardening was implemented, see Ref. [57] and Appendix C. The constitutive equations for the three dimensional beam are derived from the beam state projected von Mises model. At each integration point, the constitutive equations are implicitly solved using the return mapping scheme. Note that the beam state projected plasticity model is equivalent to the three-dimensional model with the added beam state constraint.

The three-dimensional beam state constraint is characterized by the following constraints on the components of the second Piola-Kirchhoff stress tensor,

$$\bar{S}_{22} = \bar{S}_{33} = \bar{S}_{23} = \bar{S}_{32} = 0, \quad (4-39)$$

Firstly, we define trial components for initial guess at time t ,

$$\bar{\boldsymbol{\varepsilon}}_{ij}^{e \text{ trial}} = {}^t_0 \bar{\boldsymbol{\varepsilon}}_{ij}^e + {}_0 \bar{\boldsymbol{\varepsilon}}_{ij}, \quad \bar{\boldsymbol{\varepsilon}}_{ij}^{p \text{ trial}} = {}^t_0 \bar{\boldsymbol{\varepsilon}}_{ij}^p, \quad \bar{S}_{ij}^{\text{trial}} = \bar{C}_{ijkl} \boldsymbol{\varepsilon}_{kl}^{e \text{ trial}}, \quad (4-40)$$

where $\bar{\boldsymbol{\varepsilon}}_{ij}^{e \text{ trial}}$ and $\bar{\boldsymbol{\varepsilon}}_{ij}^{p \text{ trial}}$ are the trial components of the elastic and plastic strain tensor, ${}^t_0 \bar{\boldsymbol{\varepsilon}}_{ij}^e$ and ${}^t_0 \bar{\boldsymbol{\varepsilon}}_{ij}^p$ are the elastic and plastic strain components at the configuration at time t , referred to the configuration at time 0, ${}_0 \bar{\boldsymbol{\varepsilon}}_{ij}$ is the incremental strain components at time t , and $\bar{S}_{ij}^{\text{trial}}$ is the trial component of the second Piola-Kirchhoff stress tensor. Five strain and stress components are determined, that is $(i, j) \in \{(1,1), (1,2), (2,1), (1,3), (3,1)\}$.

For a conveniently compact representation of the formulation, the matrix notation is introduced here,

$$\bar{\boldsymbol{\varepsilon}}^{e \text{ trial}} = \begin{bmatrix} \bar{\boldsymbol{\varepsilon}}_{11}^{e \text{ trial}} \\ 2\bar{\boldsymbol{\varepsilon}}_{12}^{e \text{ trial}} \\ 2\bar{\boldsymbol{\varepsilon}}_{13}^{e \text{ trial}} \end{bmatrix}, \quad \bar{\mathbf{S}}^{\text{trial}} = \begin{bmatrix} \bar{S}_{11}^{\text{trial}} \\ \bar{S}_{12}^{\text{trial}} \\ \bar{S}_{13}^{\text{trial}} \end{bmatrix}. \quad (4-41)$$

The projection matrix is given by

$$\mathbf{P} = \begin{bmatrix} 2/3 & 0 & 0 \\ 0 & 2 & 0 \\ 0 & 0 & 2 \end{bmatrix}. \quad (4-42)$$

The implicit return mapping in the beam state projected condition consists in solving the following system of algebraic equations

$$\begin{cases} \bar{\mathbf{S}}_{n+1} = (\mathbf{C}^{-1} + \gamma_{n+1} \mathbf{P})^{-1} \mathbf{C}^{-1} \bar{\mathbf{S}}^{trial} \\ \bar{\boldsymbol{\varepsilon}}_{n+1}^p = \gamma_{n+1} \sqrt{\frac{3}{2}} \frac{\mathbf{P} \bar{\mathbf{S}}_{n+1}}{\sqrt{\bar{\mathbf{S}}_{n+1}^T \mathbf{P} \bar{\mathbf{S}}_{n+1}}} \\ \bar{\boldsymbol{\varepsilon}}_{n+1}^e = \bar{\boldsymbol{\varepsilon}}^{e\,trial} - \bar{\boldsymbol{\varepsilon}}_{n+1}^p \end{cases}, \quad (4-43)$$

where $\bar{\mathbf{S}}_{n+1}$ is the second Piola-Kirchhoff stress vector at time $n+1$, \mathbf{C} is the elastic material law matrix for beam, $\bar{\boldsymbol{\varepsilon}}_{n+1}^e$ and $\bar{\boldsymbol{\varepsilon}}_{n+1}^p$ is the elastic and plastic strain vector at time $n+1$, γ_{n+1} is the plastic multiplier at time $n+1$, and n is the pseudo time index for Newton iteration. Also, the initial value of $\bar{\boldsymbol{\varepsilon}}_{n+1}^e$ and $\bar{\mathbf{S}}_{n+1}$ are trial strain and stress value $\bar{\boldsymbol{\varepsilon}}^{e\,trial}$ and $\bar{\mathbf{S}}^{trial}$, and γ_{n+1} is zero.

For plasticity criteria, the projected version of the von Mises yield function can be defined as

$$\Phi = \sqrt{\frac{3}{2} \bar{\mathbf{S}}_{n+1}^T \mathbf{P} \bar{\mathbf{S}}_{n+1}} - \sigma_y(\gamma_{n+1}). \quad (4-44)$$

in which $\sigma_y(\gamma_{n+1})$ is the yield stress function according to the hardening rule. The projected yield function has values identical to those of the three dimensional von Mises function for stress states satisfying the three dimensional Timoshenko beam constraint.

The plastic multiplier is updated as following,

$$\dot{\gamma}_{n+1} = \dot{\gamma}_n - \frac{\Phi}{\Phi'}, \quad (4-45)$$

where Φ' is the differential of von Mises yield function corresponding to the plastic multiplier.

$\bar{\mathbf{S}}_{n+1}$, $\bar{\boldsymbol{\varepsilon}}_{n+1}^e$ and $\bar{\boldsymbol{\varepsilon}}_{n+1}^p$ is iteratively evaluated by Eq. (4-43) until Eq. (4-44) becomes zero with updating the plastic multiplier in Eq. (4-45). Note that, for the material nonlinear analyses, higher order Gauss integrations could be required for better accuracy.

4.5 Numerical Studies

In this section, we present several numerical examples to demonstrate the performance and modeling capabilities of the continuum mechanics based beam elements in nonlinear analyses. In this section, 2- and 3-node

continuum mechanics based beam elements are considered. The standard full Newton-Raphson iterative scheme is employed for the nonlinear solutions in all examples.

The results obtained using the proposed beam elements are compared with the reference solutions obtained from the beam, solid, and shell elements in ADINA [58] and the beam element in ANSYS (BEAM188) [59]:

- ADINA BEAM: The beam element in ADINA is formulated using the Euler beam theory with Hermitian polynomials. The Wagner strain term is explicitly contained in the beam formulation.
- BEAM188: BEAM188 in ANSYS is based on the Timoshenko beam theory. This beam element does not consider the Wagner strain effect [30].

Table 4-1. Large twisting analysis capability of the beam, shell, and solid element models in the numerical examples considered in this study (○: capable, X: incapable).

Beam problems	Solid element model (ADINA)	Shell element model (ADINA)	Beam element models		
			ADINA BEAM (ADINA)	BEAM188 (ANSYS)	Present beam
Cross-shaped cross-section beam problem (Section 4.4.5, Load Case II)	○	X	X	X	○
Twisted cantilever beam problem (Section 4.4.6, Load Case I)	○	○	X	X	○
Twisted cantilever beam problem (Section 4.4.6, Load Case II)	○	○	X	X	○
Twisted cantilever beam problem (Section 4.4.6, Load Case III)	X	X	X	X	○
Lateral post-buckling problem (Section 4.4.7)	○	○	○	X	○

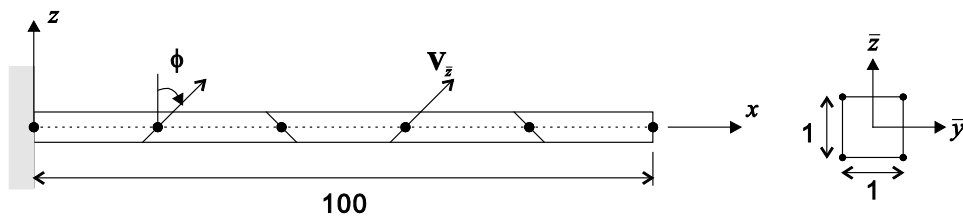


Figure 4-4. Patch test with distorted meshes ($\phi = s\pi/16$) and cross-sectional discretization.

Note that the large twisting problems considered here are mostly not easy to solve even though very fine solid and shell element models are used; see Table 4-1 for the large twisting capability of the beam, shell, and solid element models.

4.5.1 Patch Test

The mesh distortion is a serious problem in finite element analysis. Distorted elements may produce discretizations with inferior approximation properties leading to inaccurate or even invalid computational analyses. To undergo large deformation is one of various sources of mesh distortion. In other words, the performance of large deformation analysis is deeply associated with performance for distorted mesh. Through this patch test example, indirect proof of the superior nonlinear performance is presented.

A straight cantilever beam of $L = 100m$ is discretized by equidistant five 2-node beam elements with a distorted director vector $\mathbf{V}_{\bar{z}}$, as shown in Fig. 4-4. The distortion angle ($\varphi = s\pi/16$) is defined by distortion angle parameter s . We use one 4-node linear cross-sectional elements for discretizing the square cross-section shown in Fig. 4-4. The displacement boundary condition $u = v = w = \theta_x = \theta_y = \theta_z = \alpha = 0$ is applied at $x = 0m$. Two different load boundary conditions are considered at $x = 100m$ with single load step: (a) x -directional axial load ($F_x = 1000kN$) and (b) y -directional moment load ($M_y = 10kN \cdot m$). We consider the linear elastic material with Young's modulus $E = 2.0 \times 10^7 N/m^2$ and Poisson's ratio $\nu = 0$.

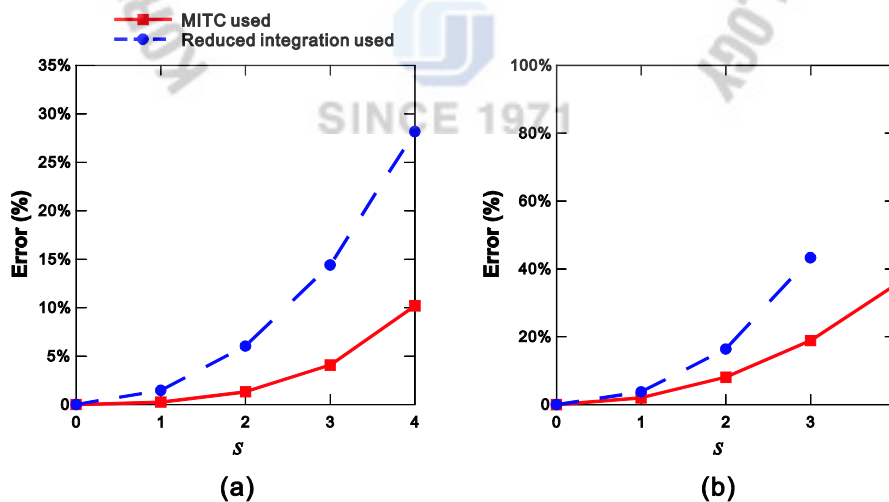


Figure 4-5. Relative errors for various distortion angle parameter s . (a) x -directional load $F_x = 1000kN$ is applied at end tip and the errors are evaluated according to the x -directional displacement u , (b) y -directional moment $M_y = 10kN \cdot m$ is applied at end tip and the errors are evaluated according to the y -directional displacement v .

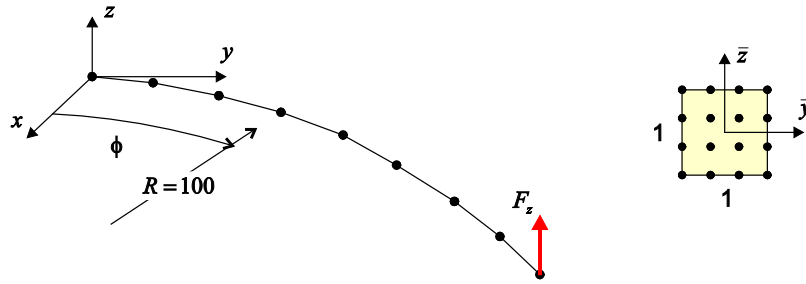


Figure 4-6. 45 degree bend beam problem with square cross-section and its discretization.

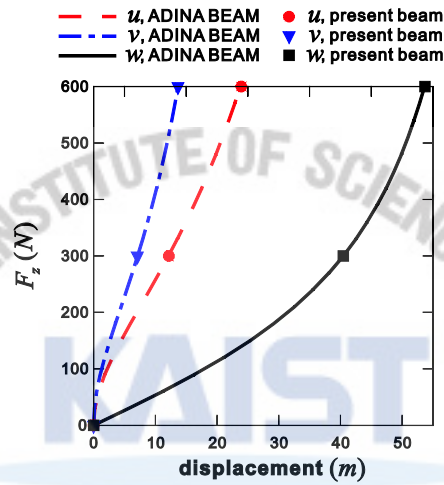


Figure 4-7. Load-displacement curves of free end tip in 45 degree bend beam problem.

Table 4-2. Free tip displacements when $F_z = 600N$ in the 45-degree bend beam problem.

	Displacements		
	u	v	w
Bathe and Bolourchi [8]	-13.4	-23.5	53.4
Simo and Vu-Quoc [16]	-13.49	-23.48	53.37
Dvorkin et al. [11]	-13.6	-23.5	53.3
Cardona and Geradin [10]	-13.74	-23.67	53.5
Ibrahimbegović et al. [55]	-13.668	-23.697	53.498
Jelenić and Crisfield [62]	-13.483	-23.479	53.371
Schulz and Filippou [60]	-13.53	-23.46	53.37
Ritto-Correa and Camotim [56]	-13.668	-23.696	53.498
Eight 2-node beam elements (present)	-13.659	-23.938	53.711
Four 3-node beam elements (present)	-13.729	-23.821	53.615

The relative errors of using reduced integration and MITC technique are compared according to the distortion angle parameter s in Fig. 4-5. The relative errors of Fig. 4-5 (a) are evaluated according to the x -directional displacement u at $x = 100m$ and The relative errors of Fig. 4-5 (b) are evaluated according to the y -directional displacement v at $x = 100m$. The reference is result of $s = 0$. The result of reduced integration used with $s = 4$ is not converged. Through the results, we can conclude that using MITC methods leads superior performance in distorted mesh problems, and also in large deformation problems. When the beams are modeled to ignore mesh distortion, the more robust performance can be possible. However it cannot be enforced in short or deep beam problems. Note that the present formulation is the closest to the model of 3-D solid elements, and also to have superior modeling capabilities.

4.5.2 45 Degree Bend Beam Problem

The classical benchmark problem proposed by Bathe and Bolourchi [8] is considered. A 45-degree circular cantilever beam with a radius of $R = 100$ has a square cross-section, as shown in Fig. 4-6. At $\varphi = 0^\circ$, the beam is fully clamped: $u = v = w = \theta_x = \theta_y = \theta_z = \alpha = 0$. The z -directional load $F_z = 600$ is applied at the free tip ($\varphi = 45^\circ$). The linear elastic material with Young's modulus $E = 1.0 \times 10^7$ and Poisson's ratio $\nu = 0$ is used. The beam is modeled using eight 2-node continuum mechanics based beam elements and the cross-section is discretized using one 16-node cubic cross-sectional element.

Fig. 4-7 illustrates the load-displacement curves calculated using the 2-node continuum mechanics based beams, and the results are compared with the reference solutions obtained from eight ADINA BEAMS with 20 incremental load steps. The present beam element provides good agreement even when only two incremental load steps are used. Table 4-2 lists the free tip displacements calculated using the 2- and 3-node continuum mechanics based beam elements compared with various previous results [8, 10, 11, 16, 55, 56, 60, 62].

4.5.3 Curved Beam Problem

The objective of this example is to verify superior modeling capabilities of the present beam finite element formulations. For this purpose, curved wide flange cross-section beam problems are proposed as shown in Fig. 4-8 (a). In order to investigate responses under the extreme condition, we discretize this problem by using eight 2-node beam elements and increase D/R ratios with fixed $R = 100m$ (that is, the beam becomes deeper). The thickness t is also increase proportional to the change of D . The wide flange cross-section is discretized by seven 2-node linear cross-sectional elements, as shown in Fig. 4-8 (a). The displacement boundary condition $u = v = w = \theta_x = \theta_y = \theta_z = \alpha = 0$ is applied at $\varphi = 0^\circ$. The load boundary condition z -directional concentrate load F_z is considered at end tip $\varphi = 90^\circ$. The magnitude of F_z is properly employed to demonstrate nonlinear effect in each D/R ratio: $F_z = 0.1N$ when $D/R = 0.01$, $F_z = 200N$ when $D/R = 0.05$,

$F_z = 5.0kN$ when $D/R = 0.1$, $F_z = 50kN$ when $D/R = 0.2$ and $F_z = 500kN$ when $D/R = 0.4$. We use the linear elastic material with Young's modulus $E = 1.0 \times 10^6 N/m^2$ and Poisson's ratio $\nu = 0$.

To obtain the reference solutions, 8-node 3-D solid elements are used with fine meshes and illustrated the case of $D/R = 0.1$ in Fig. 4-8(b). The same magnitude of F_z is applied at $\varphi = 90^\circ$ in the solid element model, and all DOFs are constrained at $\varphi = 0^\circ$. For comparison, 2-node ADINA BEAM element solutions are also calculated under same condition with present beam model in Fig. 4-8(a). It is representative solution of Hermitian polynomial-based elements.

Fig. 4-9 shows distributions of the displacements v and w along the beam length in the case of $D/R = 0.1$. The entire solutions of present beam model exhibit excellent accuracy compared with the solutions of the 3D-solid element model. On the other hand, ADINA BEAM element model is not enforced under these problem conditions.

The relative differences of using ADINA BEAM element and present beam element are compared according to the increase of D/R ratios in Fig. 4-10. The relative differences are evaluated according to the z -directional displacement w at $\varphi = 90^\circ$. Through the results, the excellent modeling capabilities of the present beam formulation is verified. Also, the stiffness matrix obtained by ADINA BEAM elements are non-symmetric condition, but present formulation gives symmetric stiffness matrix.

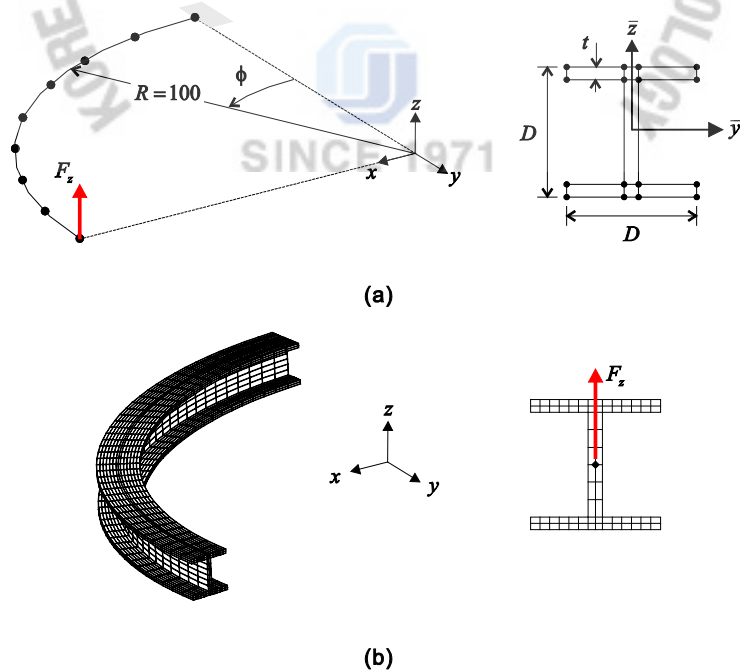


Figure 4-8. Curved deep beam problem for verifying modeling capabilities. (a) Dimensions, beam finite element model and cross-sectional discretization, (b) Solid finite element model.

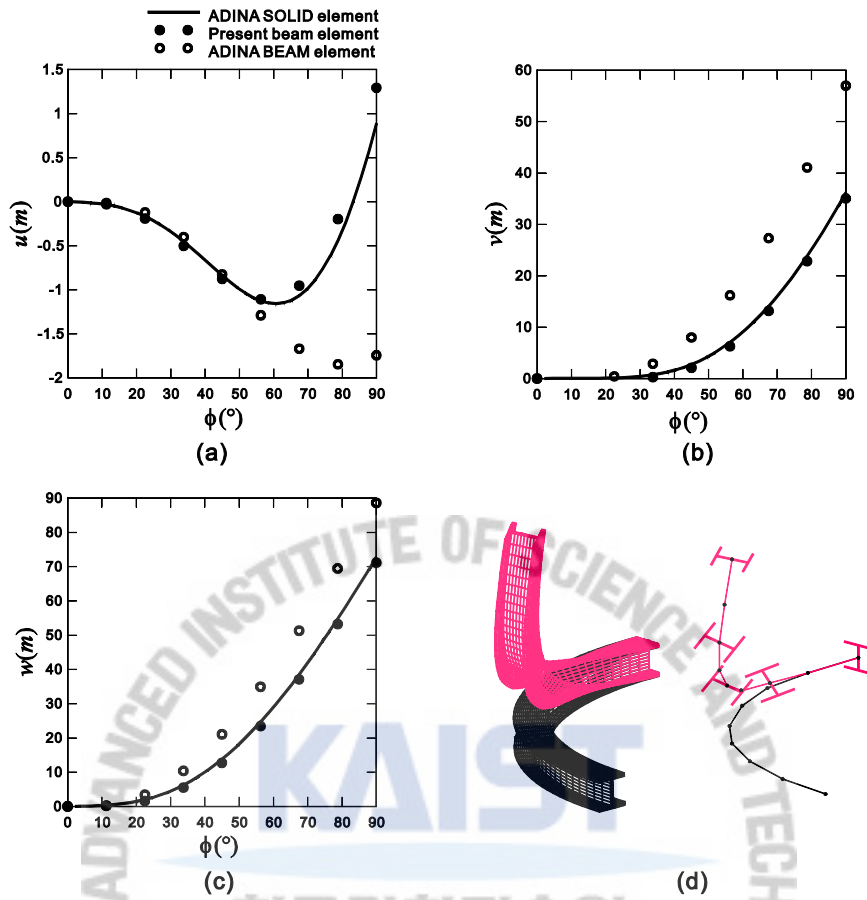


Figure 4-9. Numerical results of the curved deep beam problem along the beam length when $D/R = 0.1$. (a) Displacement u , (b) Displacement v , (c) Displacement w , (d) Associated deformed shape.

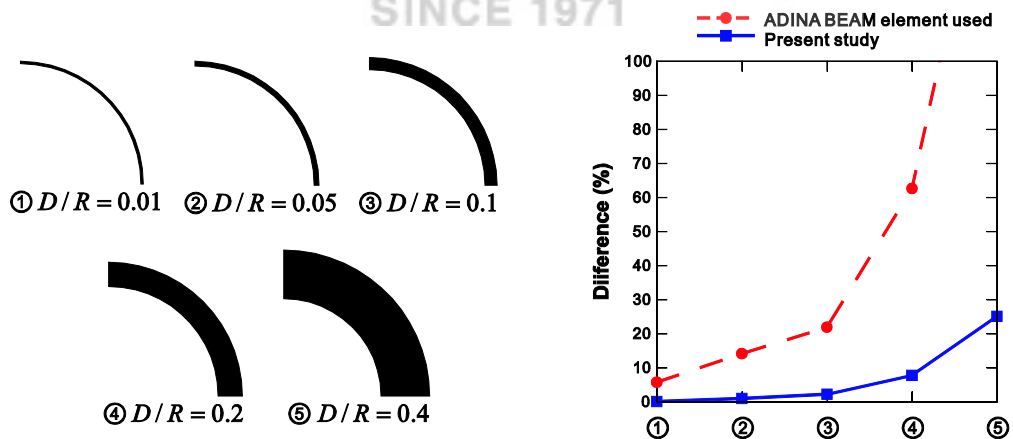


Figure 4-10. Relative difference at the loaded tip for curved deep beam problem according to the various D/R ratios.

4.5.4 Z-shaped Cross-Section Beam Problem

We consider the benchmark problem proposed by Wackerfuß and Gruttmann [47]. As shown in Fig. 4-11, a straight cantilever beam of $L = 1m$ is considered with a Z-shaped cross-section. The beam is modeled using two 2-node continuum mechanics based beam elements and the cross-section is discretized using seven 16-node cubic cross-sectional elements. The boundary condition $u = v = w = \theta_x = \theta_y = \theta_z = \alpha = 0$ is applied at $x = 0m$. The twist angle θ_x is prescribed at the free tip ($x = 1m$). The elastic-perfectly-plastic material ($E = 2.1 \times 10^{11} N/m^2$, $\nu = 0.3$, and yield stress $Y_0 = 2.4 \times 10^5 kN/m^2$) is used.

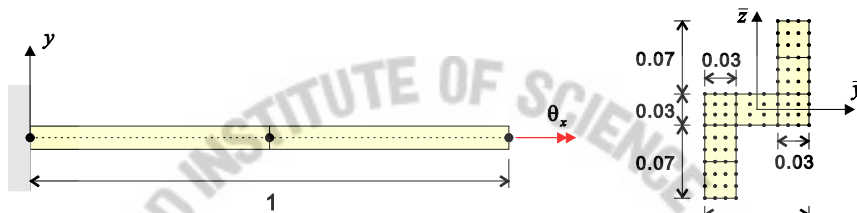


Figure 4-11. Z-shaped cross-section beam problem and its longitudinal and cross-sectional meshes (unit: m).

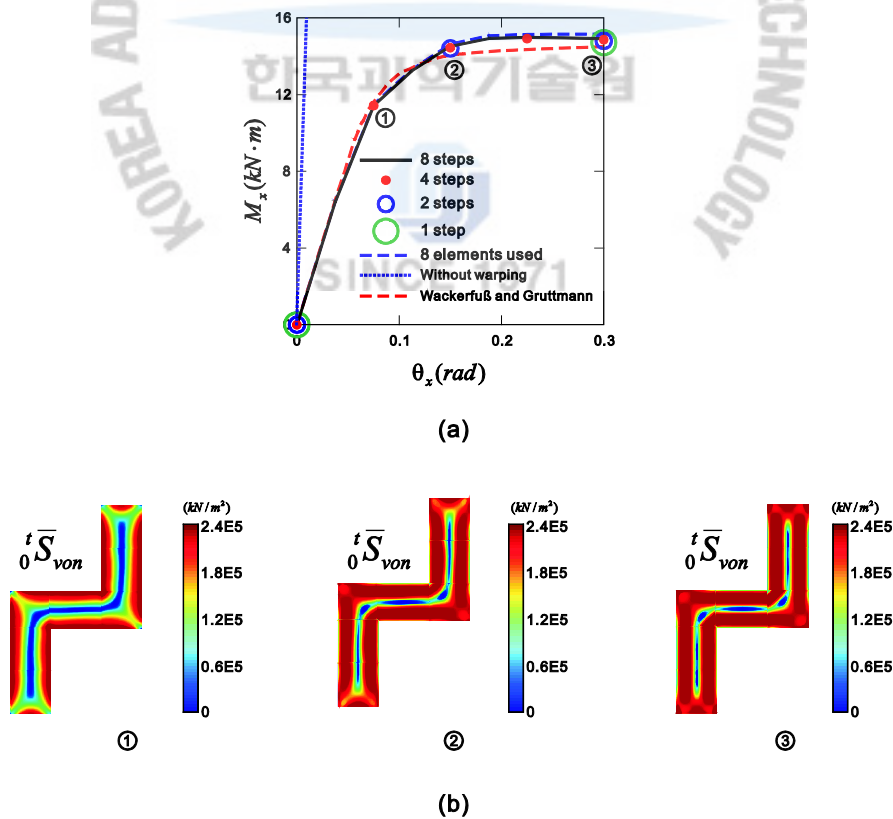


Figure 4-12. Numerical results in the Z-shaped cross-section beam problem: (a) load-displacement curves and (b) distributions of the von Mises stress obtained from the continuum mechanics based beam elements.

Fig. 4-12(a) displays the load-displacement curves calculated using two 2-node beam elements with four different incremental steps (1, 2, 4, and 8 incremental steps) and using eight 2-node beam elements with 8 incremental steps. The numerical results are in good agreement with the reference solution obtained by Wackerfuß and Gruttmann [47]. The almost full plastic state is reached with only a single incremental step. Fig. 4-12(b) illustrates the von Mises stress distributions on the cross-section at $x = 0.5m$ obtained from the continuum mechanics based beam elements. The propagation of the yield region is observed.

4.5.5 Cross-Shaped Cross-Section Beam Problem

We consider a straight cantilever beam with a length of $L = 1m$ and a cross-shaped cross-section, as shown in Fig. 4-13(a). The beam is modeled using five continuum mechanics based beam elements and the cross-section is discretized using five 16-node cubic cross-sectional elements. The boundary condition $u = v = w = \theta_x = \theta_y = \theta_z = \alpha = 0$ is applied at $x = 0m$. Two load cases are considered:

- Load Case I: The bending moment M_y is applied at the free tip ($x = 1m$).
- Load Case II: The twisting moment (torsion) M_x is applied at the free tip ($x = 1m$).

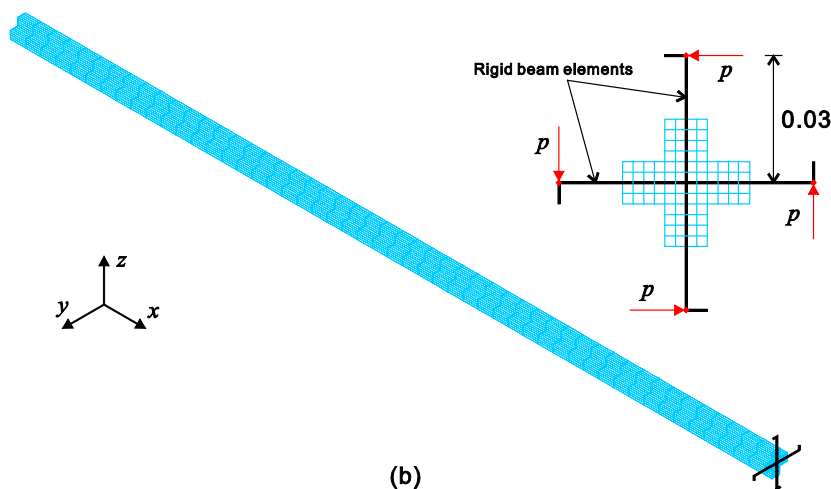
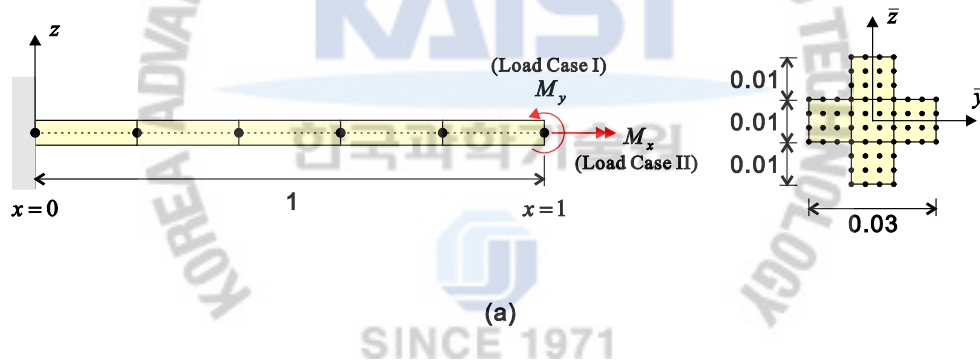


Figure 4-13. Cross-shaped cross-section beam problem (unit: m): (a) longitudinal and cross-sectional meshes used in the beam model (5 beam elements) and (b) solid element model used (4,000 solid elements).

To obtain the reference solution for Load Case II, four thousand 27-node solid elements are used in the solid element model presented in Fig. 4-13(b). In order to appropriately apply the twisting moment in the cross-section at the free tip, four rigid beam elements are also modeled and four point loads $p = M_x / (4 \times 0.03)$ are applied at the end tip of each rigid beam element, as seen in Fig. 4-13(b). All degrees of freedom are fixed at $x = 0m$.

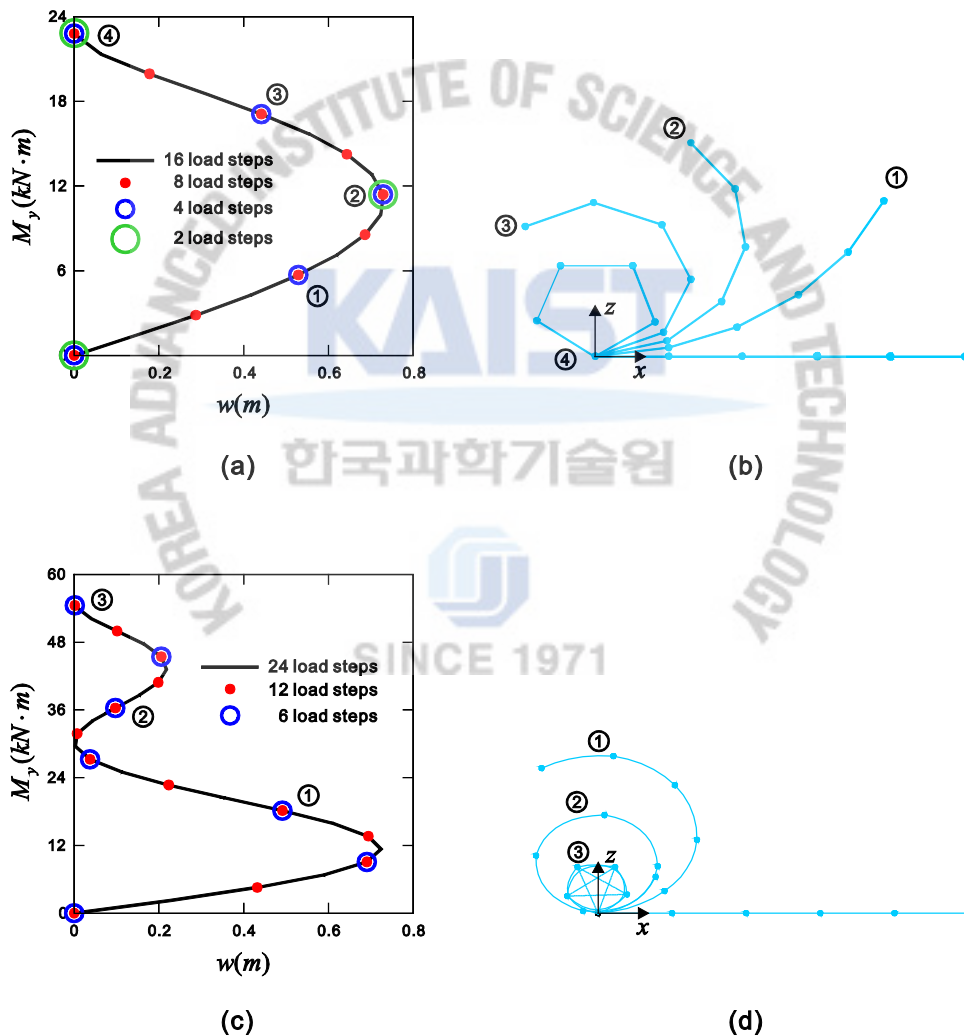


Figure 4-14. Numerical results for Load Case I in the cross-shaped cross-section beam problem: (a) and (b) load-displacement curves and deformed shapes, respectively, when five 2-node beam elements were used; and (c) and (d) load-displacement curves and deformed shapes, respectively, when five 3-node beam elements used. (Note: The center nodes of the 3-node beam elements are not plotted.)

Fig. 4-14 presents the responses calculated for Load Case I with the linear elastic material (Young's modulus $E = 2.0 \times 10^{11} \text{ N/m}^2$ and Poisson's ratio $\nu = 0$). Fig. 4-14(a) illustrates the load-displacement curves calculated using five 2-node beam elements with four different load steps (2, 4, 8, and 16 load steps), and Fig. 4-14(b) shows the corresponding deformed shapes. The tip rotation 2π can be reached using only two load steps. Fig. 4-14(c) shows the load-displacement curves obtained from five 3-node beam elements with three different load steps (6, 12, and 24 load steps), and the corresponding deformed shapes are presented in Fig. 4-14(d). The tip rotation 4π can be calculated using only 6 load steps.

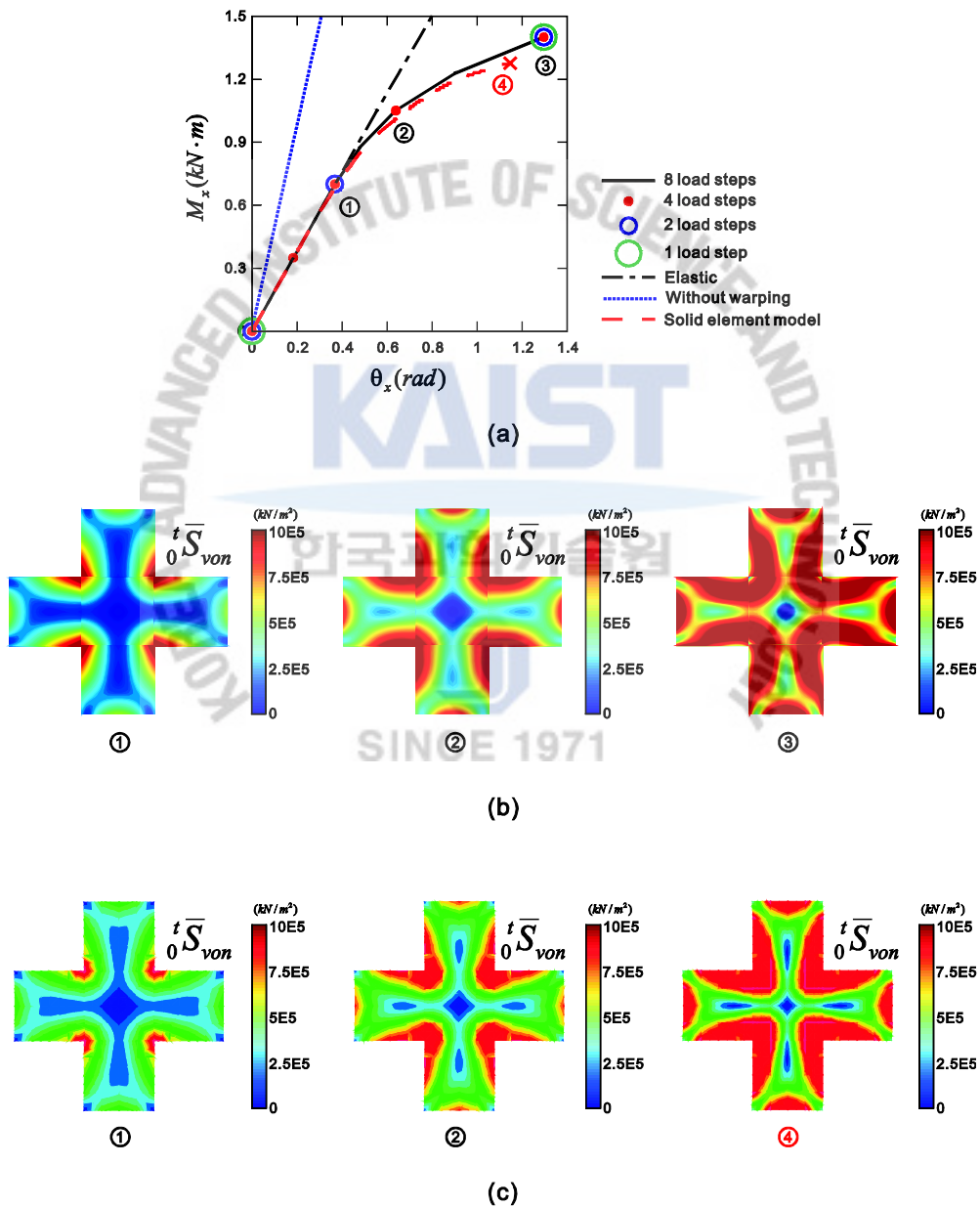


Figure 4-15. Numerical results for Load Case II in the cross-shaped cross-section beam problem (five 2-node beam elements): (a) load-displacement curves, (b) distributions of the von Mises stress obtained from the beam element model, and (c) distributions of the von Mises stress obtained from the solid element model.

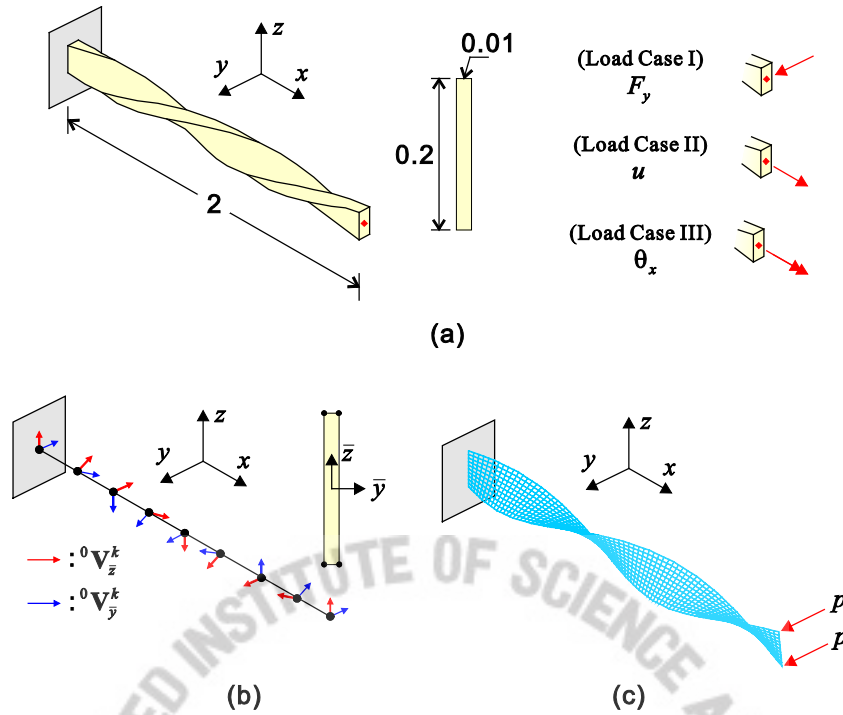


Figure 4-16. Twisted cantilever beam problem (unit: m): (a) problem description and (b) the longitudinal and cross-sectional meshes used (8 beam elements). The twisted geometry is modeled simply through changing the director vectors of the continuum mechanics based beams (${}^0V_y^k$ and ${}^0V_z^k$). (c) Shell element model (800 shell elements).

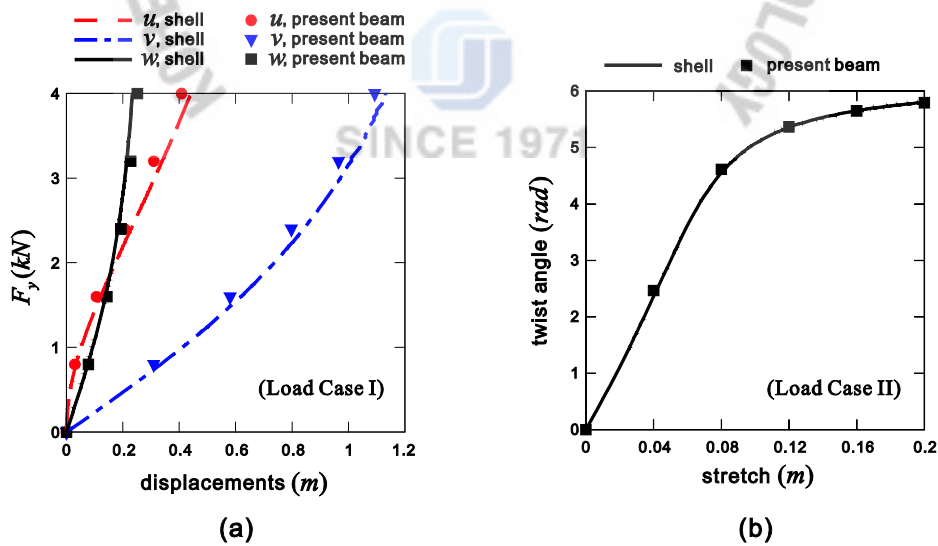


Figure 4-17. Numerical results in the twisted cantilever beam problem: (a) load-displacement curves at the free tip for Load Case I and (b) twist angle-stretch relationship for Load Case II when the prescribed displacement is applied.

Fig. 4-15 shows the responses obtained for Load Case II when the elastic-perfectly-plastic material ($E = 2.0 \times 10^{11} \text{ N/m}^2$, $\nu = 0$, and yield stress $Y_0 = 1.0 \times 10^6 \text{ kN/m}^2$) is used. Fig. 4-15(a) presents the load-displacement curves calculated using five 2-node beam elements (42 DOFs) with four different load steps (1, 2, 4, and 8 load steps). The almost full plastic state is reached with only a single load step. The reference solutions are obtained using four thousand 27-node solid elements (111,894 DOFs) with 800 load steps using ADINA. In the calculation of the reference solutions, the plastic response cannot be captured with 400 load steps, and the analysis with 800 load steps is also terminated early, as seen in Fig. 4-15(a). Figs. 4-15(b) and (c) display the von Mises stress distributions on the cross-section at $x = 0.5 \text{ m}$ in the beam and solid element models, respectively. It is observed that the yield region is propagating appropriately in the beam element model.



Figure 4-18. Deformed shapes for Load Case II in the twisted cantilever beam problem: (a) shell element model and (b) beam element model.

4.5.6 Twisted Cantilever Beam Problem

Consider the twisted cantilever beam with a thin rectangular cross-section as illustrated in Fig. 4-16(a). The beam length is $2m$ and the total twisted angle is 2π . The boundary condition $u = v = w = \theta_x = \theta_y = \theta_z = \alpha = 0$ is applied at $x = 0m$. The linear elastic material with Young's modulus $E = 2.0 \times 10^{11} N/m^2$ and Poisson's ratio $\nu = 0$ are used. The following three load cases are considered:

- Load Case I: The shear force F_y is applied at the free tip ($x = 2m$).
- Load Case II: The displacement u is prescribed at the free tip ($x = 2m$).
- Load Case III: The twist angle θ_x is prescribed at the free tip ($x = 2m$).

The twisted cantilever beam is modeled using eight 2-node beam elements, and the thin rectangular cross-section is discretized using one 4-node cross-sectional element, as seen in Fig. 4-16(b). In order to consider the twisted geometry, the director vectors are initially given as described in Fig. 4-16(b).

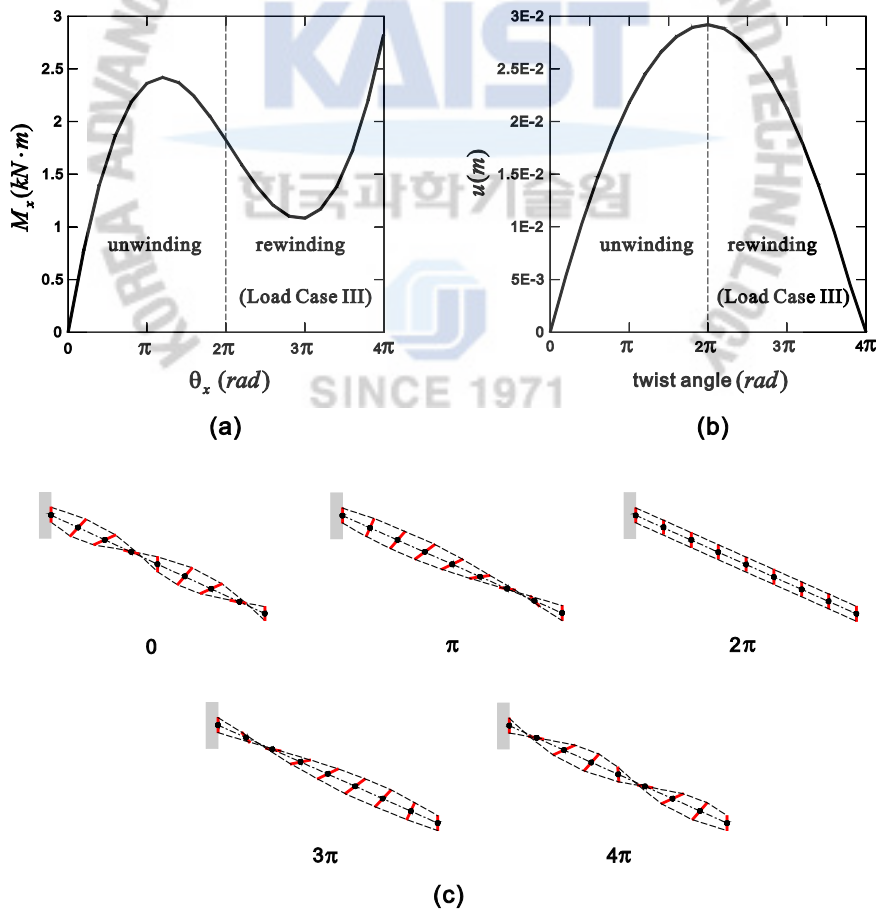


Figure 4-19. Numerical results for Load Case III in the twisted cantilever beam problem: (a) load-displacement curve between M_x and θ_x at the free tip, (b) relationship between u and θ_x at the free tip, and (c) deformed shapes when the twist angles at the free tip are 0 , π , 2π , 3π , and 4π .

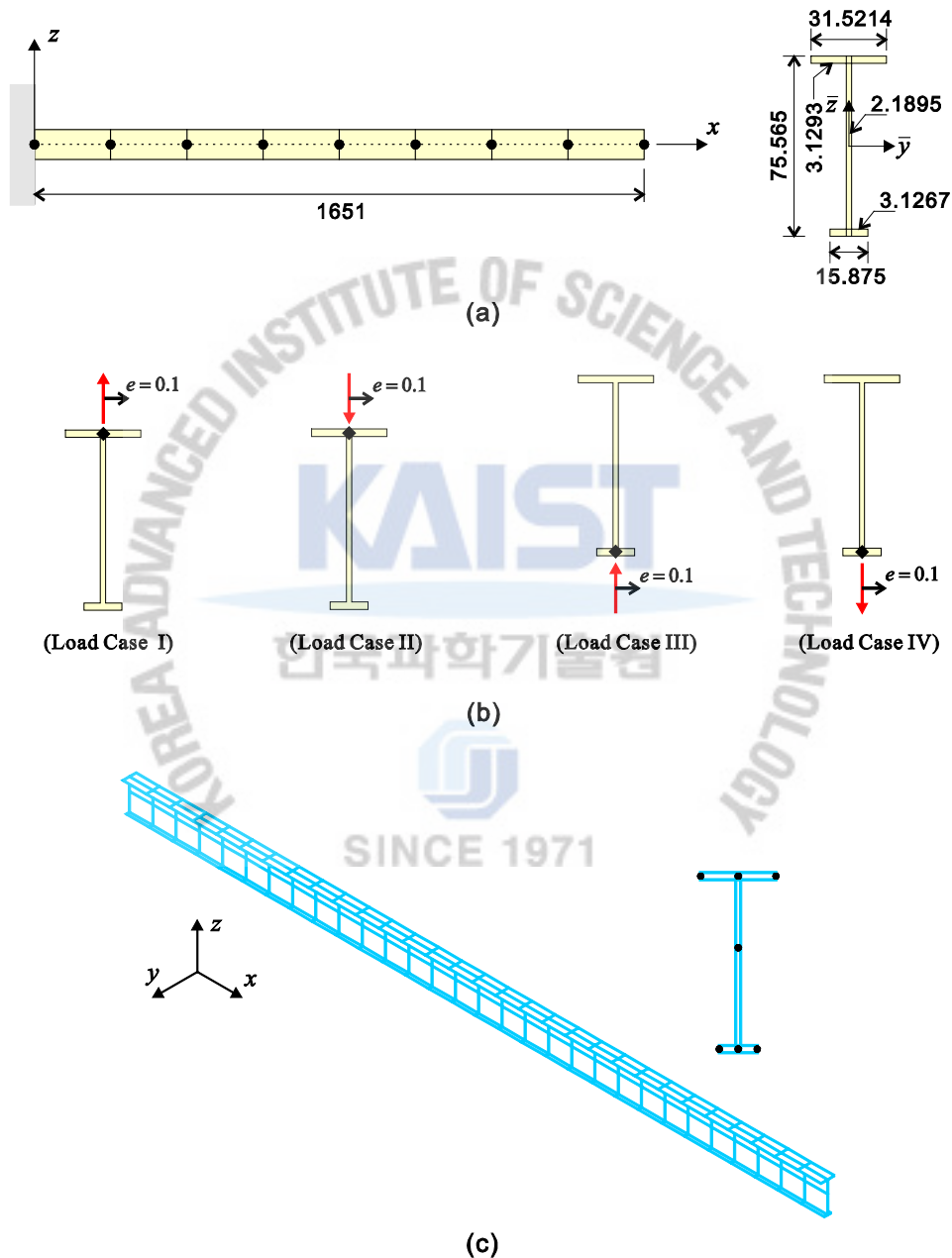


Figure 4-20. Lateral post-buckling analyses of a straight cantilever beam with a mono-symmetric I-section (unit: *mm*): (a) the longitudinal and cross-sectional meshes used (8 beam elements), (b) four load cases, and (c) shell element model (180 shell elements).

In order to obtain the reference solutions, the MITC4 shell elements (800 elements) are used in the shell element model presented in Fig. 4-16(c). Two point loads $p = 0.5F_y$ are applied at $x = 2m$ for Load Case I, and the prescribed displacement u is applied to all nodes at $x = 2m$ for Load Case II. All degrees of freedom are fixed at $x = 0m$.

Figs. 4-17(a) and (b) display the load-displacement curves for Load Case I and the twist angle-stretch relation for Load Case II. For Load Case II, Figs. 4-18(a) and (b) show the deformed shapes obtained from the shell element model and beam element model, respectively. The numerical results of the beam element model exhibit good agreement with the reference shell solutions. Note that, in order to obtain appropriate responses in this beam problem, the coupled behavior of stretching, bending, shearing, twisting, and warping should be correctly considered in the beam formulation.

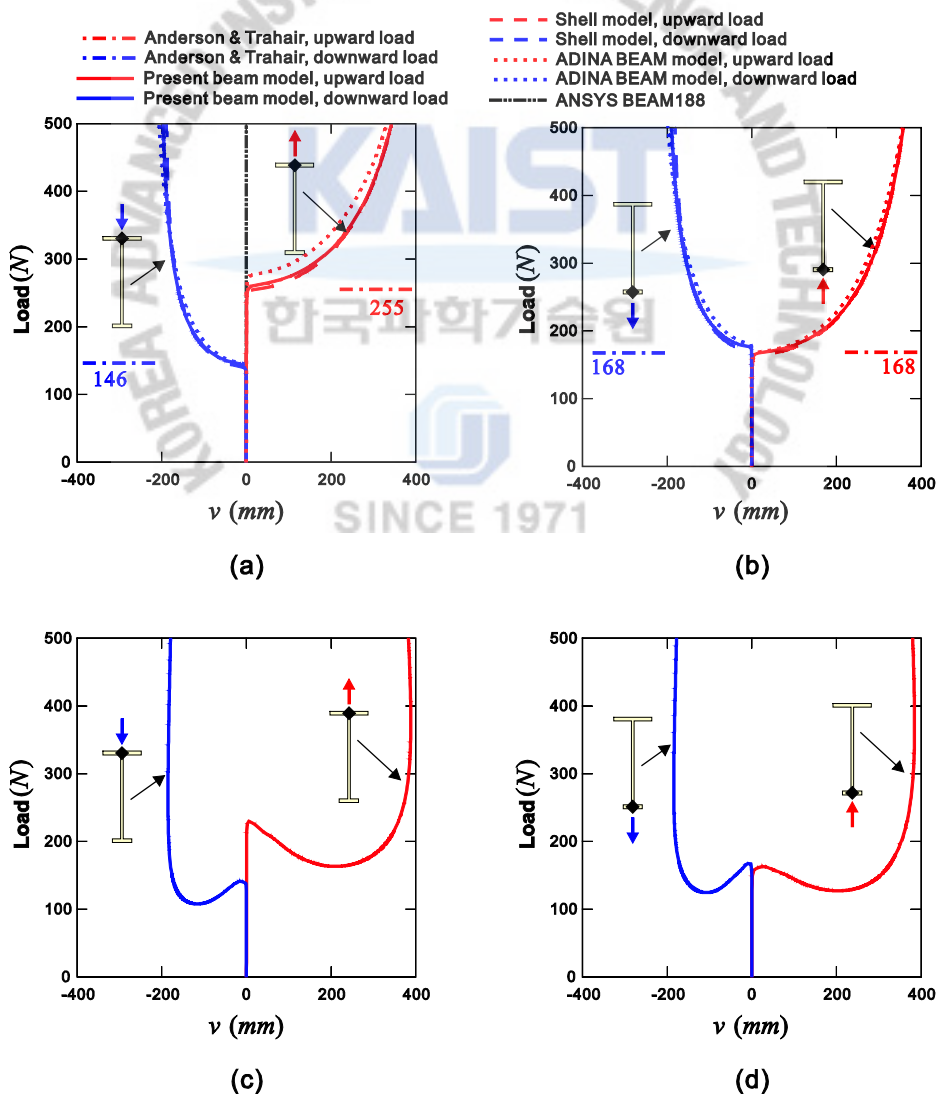


Figure 4-21. Lateral post-buckling responses for the four load cases in Fig. 15(b): (a) and (b) elastic material

used, and (c) and (d) elastoplastic material used.

For Load Case III, Figs. 4-19(a) and (b) present the torsional moment M_x and longitudinal displacement u at the free tip according to the twist angle at the free tip. The corresponding deformed shapes are plotted in Fig. 4-19(c). As the twist angle increases, the twisted beam is unwound from $\theta_x = 0$ to 2π , and then it is rewound from $\theta_x = 2\pi$ to 4π . It is very interesting to observe the snap through phenomenon in Fig. 4-19(a), and the lengthening and shortening due to the unwinding and rewinding in Fig. 4-19(b). Note that Load Case III cannot be analyzed using the solid and shell element models due to convergence problems. Further studies are required for understanding the numerical difficulty as well as the physical phenomenon.

4.5.7 Lateral post-buckling problem

Through lateral post-buckling analyses, this section demonstrates how well the present beam element captures the Wagner effect. As illustrated in Fig. 4-20(a), a straight cantilever beam of $L = 1651mm$ is considered with a mono-symmetric I-section, which was used in the lateral post-buckling experiment conducted by Anderson and Trahair [63]. Young's modulus E is $65.123 \times 10^3 N/mm^2$ and shear modulus G is $25.967 \times 10^3 N/mm^2$.

The boundary condition $u = v = w = \theta_x = \theta_y = \theta_z = \alpha = 0$ is applied at $x = 0mm$ and the following four load cases are considered, see Fig. 4-20(b):

- Load Case I: The upward direction load is applied at the upper flange at the free tip.
- Load Case II: The downward direction load is applied at the upper flange at the free tip.
- Load Case III: The upward direction load is applied at the lower flange at the free tip.
- Load Case IV: The downward direction load is applied at the lower flange at the free tip.

The loads are applied with the y -directional eccentricity of $e = 0.1mm$ for the consideration of imperfections.

The cantilever beam is modeled using eight 2-node beam elements and the mono-symmetric I-section is discretized using seven 16-node cubic cross-sectional elements as shown in Fig. 4-20(a). For each sub-beam element, $2 \times 4 \times 4$ integration is used. In order to obtain the reference solutions, the MITC4 shell elements (180 elements) are used in the shell element model, as shown in Fig. 4-20(c). In order to consider the load position and eccentricity, the rigid beam finite elements with a length of $0.1mm$ are inserted at the loaded tip. All degrees of freedom are fixed at $x = 0mm$.

Figs. 4-21(a) and (b) show the lateral post-buckling responses of the cantilever beam calculated for the four different load cases. Different bifurcation points are observed depending on the direction and position of the load application. To predict this interesting phenomenon accurately, it is important to include the Wagner strain in the beam formulation. Note that, in the present beam formulation, the Wagner strain is automatically considered without pre-calculating Wagner's coefficient and the buckling modes. The bifurcation points and load-

displacement curves calculated using the continuum mechanics based beam elements are in good agreement with the experimental results and reference shell solutions.

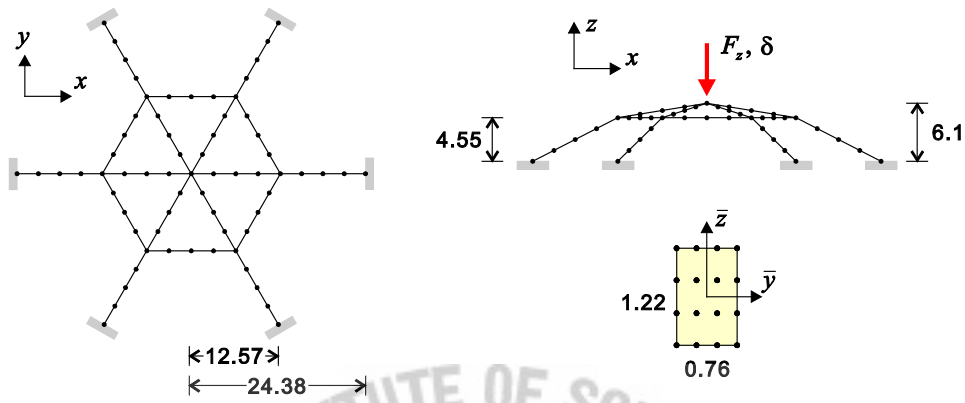


Figure 4-22. Framed dome problem and the finite element discretization using the continuum mechanics based beam elements.

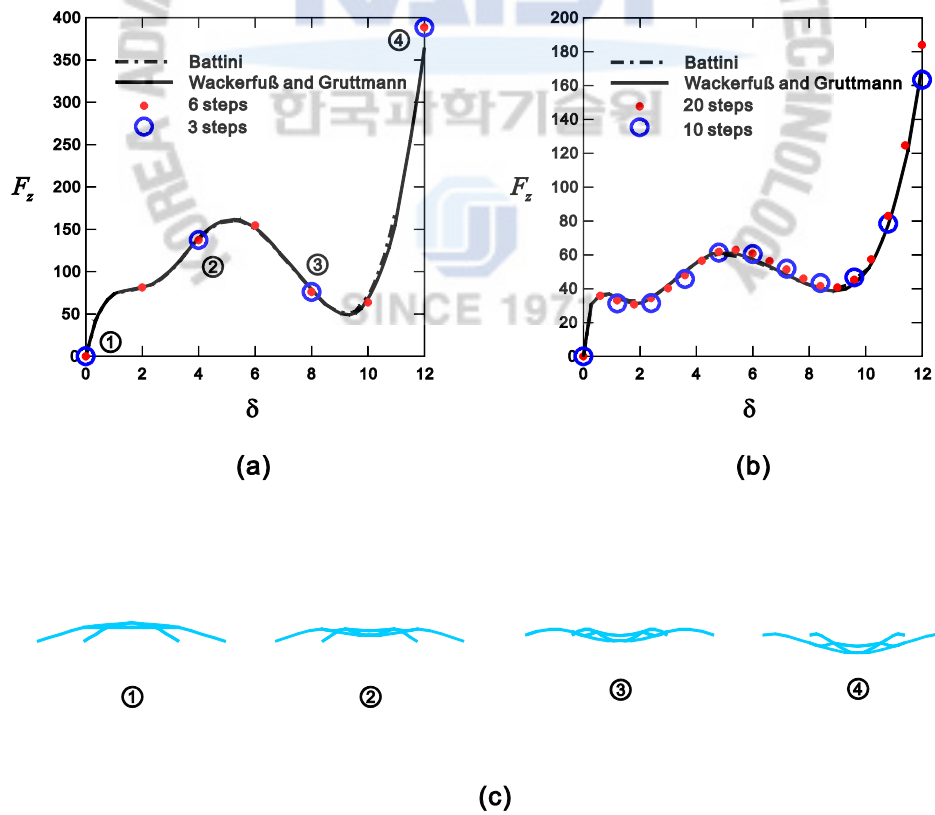


Figure 4-23. Numerical results of the framed dome problem: (a) load-displacement curves for the elastic analysis, (b) load-displacement curve for the elastoplastic analysis, and (c) deformed shapes.

For comparison, the same mesh is used for the calculations using ADINA BEAM and BEAM188. Since ADINA BEAM cannot consider the load position and eccentricity, rigid beam elements are additionally used at the loaded tip to model the eccentricity. ADINA BEAM captures the complicated bifurcations with acceptable accuracy but, as mentioned, additional modeling effort is necessary. BEAM188 in ANSYS cannot capture these complicated phenomena. Furthermore, Figs. 4-21(c) and (d) present the lateral post-buckling behaviors when elastoplastic material is used (Young's modulus $E = 65.123 \times 10^3 \text{ N/mm}^2$, shear modulus $G = 25.967 \times 10^3 \text{ N/mm}^2$, initial yield stress $Y_0 = 40 \text{ N/mm}^2$, and hardening modulus $H = 0.5E$).

4.5.8 Framed dome problem

Finally, a framed dome structure that consists of 18 beam members of a rectangular cross-section is considered as described in Fig. 4-22 [64, 65]. The boundary condition $u = v = w = \theta_x = \theta_y = \theta_z = \alpha = 0$ is applied at nodes on the gray colored areas in Fig. 17. The z -directional concentrate load F_z is applied at the top of the dome. We perform large displacement elastic and elastoplastic analyses. For the elastic analysis, Young's modulus $E = 20690$ and shear modulus $G = 8830$ are used. For the elastoplastic analyses, Young's modulus $E = 20690$, shear modulus $G = 8830$, initial yield stress $Y_0 = 60$, and hardening modulus $H = 0.25E$ are considered. Each beam member is modeled using four 2-node beam elements and the rectangular cross-section is discretized using one 16-node cubic cross-sectional element. The $2 \times 4 \times 4$ integration is used for each beam.

Figs. 4-23(a) and (b) illustrate the load-displacement curves calculated through incrementally controlling the vertical displacement δ with the elastic and elastoplastic materials. Fig. 4-23(c) shows the deformed shapes obtained from the elastic analysis. The numerical results are in good agreement with those obtained by Battini [64] and Wackerfuß and Gruttmann [65].

4.6 Concluding remarks

In this chapter, a nonlinear formulation of the continuum mechanics based beam elements was presented and their performance in general nonlinear analyses that focused on large twisting behaviors was demonstrated. Since the beam elements are derived from assemblages of 3D solid elements, they have inherently advanced modeling capabilities in the analysis of complicated 3D beam geometries including curved and twisted geometries, varying cross-sections, eccentricity, and arbitrary cross-sectional shapes [50, 51]. The total Lagrangian formulation was used to obtain the complete tangent stiffness matrix and internal load vector with the warping displacements.

The resulting formulation can consider the fully coupled nonlinear behaviors of bending, shearing, stretching, twisting, and warping. In particular, large twisting and lateral buckling behaviors can be accurately predicted and, in the beam formulation, the Wagner effect is implicitly included, unlike other beam elements. Through

various numerical examples, the strong modeling and predictive capabilities of the nonlinear formulation of the continuum mechanics based beam elements were demonstrated for general nonlinear analysis. The most valuable asset of the proposed beam elements is their excellent analysis capability in large twisting problems.



Chapter 5. Eigen Recomposition Method to Improve Nonlinear Performance

In this chapter, we present a new numerical method to improve nonlinear performance: the eigen recomposition. The superior nonlinear performance of proposed method is demonstrated through several numerical examples.

5.1 Motivation

The nonlinear analysis of finite elements is abundantly performed in various branches of engineering design and scientific research. In order to achieve a safer and more economical design for more complex system, there are continuous demands efficient, robust and reliable numerical tools for nonlinear analysis.

In general, the iterative solution procedure, for example full Newton method, enables to obtain the solution of the nonlinear equation. However, the use of the iterative scheme also yields stability, convergence and reliability problems. A slow convergence process and an amiss solution are often observed. Also, certain types of problems are shown upper bound of solution despite of numerous load steps. The efforts to overcome these difficulties can be classified by two approaches; develop finite element models and solution algorithm models.

For a long time, considerable efforts have been made regarding improvement of nonlinear finite element models [66, 67]. Although novel numerical methods are successfully introduced, limitations are still remained. Furthermore, all of these studies are only focused on non-vectorial nature of rotational variables. Thus, there is still a need for more insight of various perspective and clearer guidelines on the nonlinear analysis.

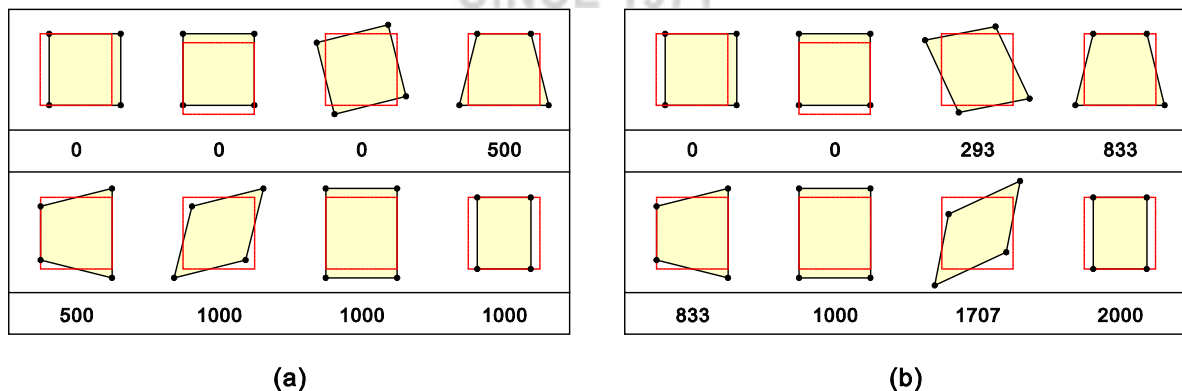


Figure 5-1. The eight eigenpairs for 2D plane stress element. (a) Basic eigenmodes, (b) eigenmodes subjected to the uniform stress distribution.

In general, the element subjected to the stress distribution shows stiffer behaviors. The consideration of this additional stiffness enables faster convergence. However, the stress distribution also makes critical problem by yielding parasitic stiffening. Fig. 5-1(a) shows eight eigenpairs of the 2D plane stress element without any stress distributions which consists of three rigid body, two bending, two stretching and a single shearing eigenvectors. Fig. 5-1(b) shows eight eigenpairs of the 2D plane stress element subjected to the constant x -directional normal stress distribution. As author's opinion, the ideal stiffening from stress distributions is to only increase the eigenvalues without distortion of the eigenvectors, and three rigid body modes are also remaining. However, the eigenpairs for rigid body rotation and shearing action, shown in Fig. 5-1(b), obviously display problems.

5.2 Stiffening of Rigid Body Rotation

In a geometrical nonlinear analysis, a deformation of the rigid body rotation generates parasitic strain energy in second order term like a 'locking phenomena', and the parasitic strain energy is governed by stress distributions. In other words, the eigenvalue of the rigid body rotation is no more zero energy, and developed by stress distributions. In order to identify and analysis the effects of stress distributions on the eigenpair of the rigid body rotation, we consider an internal virtual work of an isoparametric body subjected to the eigen deformation, as shown in Fig. 5-2.

Based on the total Lagrangian formulation, the increment of the internal virtual work $\delta\Pi$ is given by [ref],

$$\delta\Pi = \int_{0V} {}_0e_{ij} C_{ijkl} \delta {}_0e_{kl} d^0V + \int_{0V} {}_0^t S_{ij} \delta {}_0\eta_{ij} d^0V, \quad (5-1)$$

in which 0V is the initial area of the isoparametric body, ${}_0e_{ij}$ and ${}_0\eta_{ij}$ denote respectively the linear and nonlinear terms of incremental Green-Lagrange strain tensor, C_{ijkl} is the material law tensor, ${}_0^t S_{ij}$ is the second Piola-Kirchhoff stress measured, and the left δ denotes a variation.

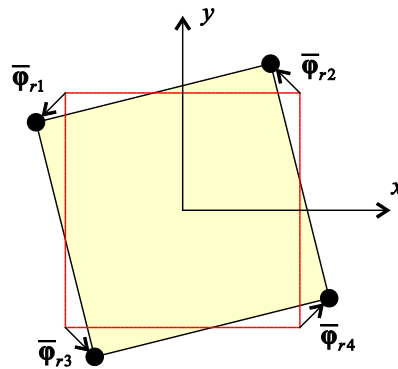


Figure 5-2. An isoparametric body subjected to the rigid body rotation.

Eq. (5-1) can be simplified under assumption of 2D plane stress condition with zero Poisson ratio,

$$\delta\Pi = \delta\Pi_{linear} + \delta\Pi_{nonlinear}$$

$$\text{with } \delta\Pi_{linear} = \int_{0V} E_0 e_{11} \delta_0 e_{11} + E_0 e_{22} \delta_0 e_{22} + 4G_0 e_{12} \delta_0 e_{12} d^0V,$$

$$\delta\Pi_{nonlinear} = \int_{0V} {}^iS_{11} \delta_0 \eta_{11} + {}^iS_{22} \delta_0 \eta_{22} + 2 {}^iS_{12} \delta_0 \eta_{12} d^0V, \quad (5-2)$$

where $\delta\Pi_{linear}$ is internal virtual work yielded by linear terms of Green-Lagrange strain, $\delta\Pi_{nonlinear}$ is internal virtual work yielded by nonlinear terms of Green-Lagrange strain and second Piola-Kirchhoff stress distributions, and E and G are respectively Young's modulus and shear modulus. Note that the stress distributions only have effects on nonlinear internal virtual work.

In order to calculate the internal virtual work for the rigid body rotation, the nodal eigen deformation vector $\bar{\varphi}_r$ is considered, as shown in Fig. 5-2.

$$\bar{\varphi}_r = [\bar{\varphi}_{r1} \quad \bar{\varphi}_{r2} \quad \bar{\varphi}_{r3} \quad \bar{\varphi}_{r4}]^T \quad \text{and} \quad \bar{\varphi}_r^T \bar{\varphi}_r = 1,$$

$$\text{with } \bar{\varphi}_{r1} = \frac{\sqrt{2}}{4} [-1 \quad -1], \quad \bar{\varphi}_{r2} = \frac{\sqrt{2}}{4} [-1 \quad 1], \quad \bar{\varphi}_{r3} = \frac{\sqrt{2}}{4} [1 \quad -1] \quad \text{and} \quad \bar{\varphi}_{r4} = \frac{\sqrt{2}}{4} [1 \quad 1]. \quad (5-3)$$

The eigen deformation field φ_r can be obtained from interpolation of the nodal eigen deformation vector,

$$\varphi_r = \mathbf{H} \bar{\varphi}_r, \quad (5-4)$$

where \mathbf{H} is the conventional interpolation matrix which consist of shape functions. Then, standard algebraic manipulations with Eq. (5-3) and (5-4) yield,

$$\varphi_r = [\varphi_{r1} \quad \varphi_{r2}]^T = \frac{\sqrt{2}}{4} [-y \quad x]^T. \quad (5-5)$$

Following the definition of Green-Lagrange strain, the linear and nonlinear strain terms for φ_r are denoted as,

$${}_0e_{11} = \delta_0 e_{11} = \frac{\partial \varphi_{r1}}{\partial x} = 0, \quad {}_0e_{22} = \delta_0 e_{22} = \frac{\partial \varphi_{r2}}{\partial y} = 0, \quad {}_0e_{12} = \delta_0 e_{12} = \frac{1}{2} \left(\frac{\partial \varphi_{r1}}{\partial y} + \frac{\partial \varphi_{r2}}{\partial x} \right) = 0, \quad (5-6)$$

$$\left(\begin{array}{l} \delta_0 \eta_{11} = \frac{\partial \varphi_{r1}}{\partial x} \frac{\partial \delta \varphi_{r1}}{\partial x} + \frac{\partial \varphi_{r2}}{\partial x} \frac{\partial \delta \varphi_{r2}}{\partial x} = \frac{1}{8} \\ \delta_0 \eta_{22} = \frac{\partial \varphi_{r1}}{\partial y} \frac{\partial \delta \varphi_{r1}}{\partial y} + \frac{\partial \varphi_{r2}}{\partial y} \frac{\partial \delta \varphi_{r2}}{\partial y} = \frac{1}{8} \\ \delta_0 \eta_{12} = \frac{1}{2} \left(\frac{\partial \varphi_{r1}}{\partial x} \frac{\partial \delta \varphi_{r1}}{\partial y} + \frac{\partial \delta \varphi_{r1}}{\partial x} \frac{\partial \varphi_{r1}}{\partial y} + \frac{\partial \varphi_{r2}}{\partial x} \frac{\partial \delta \varphi_{r2}}{\partial y} + \frac{\partial \delta \varphi_{r2}}{\partial x} \frac{\partial \varphi_{r2}}{\partial y} \right) = 0 \end{array} \right). \quad (5-7)$$

Substituting Eqs. (5-6) and (5-7) into Eq. (5-2), the internal virtual work for the rigid body rotation is finally obtained as a function of stress distributions,

$$\delta\Pi_{linear} \Big|_{\mathbf{u}=\varphi_r} = 0 \quad \text{and} \quad \delta\Pi_{nonlinear} \Big|_{\mathbf{u}=\varphi_r} = \frac{1}{8} \int_{0V} ({}^iS_{11} + {}^iS_{22}) d^0V. \quad (5-8)$$

The internal virtual work for the rigid body rotation should be zero in physically, but the parasitic strain energy is generated by nonlinear terms, as shown in Eq. (5-8). The tangent modulus for the rigid body rotation is to be stiff as the summation of internal stress ${}'_0S_{11}$ and ${}'_0S_{22}$ increases. It means that the global stiffness matrix has an accumulated error from the stress distributions in nonlinear analysis, and this accumulated error lead to an upper bound of nonlinear convergence.

5.3 Deficiency of Shear Eigenmode

As mentioned in introduction, 4-node 2D plane stress element has only one shear eigenvector, as shown in Fig. 5-3(a). In linear analysis context, the one shear eigenvector are sufficient to represent other shear deformation shapes like Fig. 5-3(b) and (c). However, in nonlinear analysis context, unfortunately the single shear eigenvector cannot represent other shear deformation shapes due to the difference of the strain energy. In order to investigate this deficiency problem, we consider internal virtual works of isoparametric body subjected to the three types of shear deformation φ_A , φ_B and φ_C .

The nodal eigen deformation vector $\bar{\varphi}_A$ is written by,

$$\bar{\varphi}_A = [\bar{\varphi}_{A1} \quad \bar{\varphi}_{A2} \quad \bar{\varphi}_{A3} \quad \bar{\varphi}_{A4}]^T \text{ and } \bar{\varphi}_A^T \bar{\varphi}_A = 1,$$

$$\text{with } \bar{\varphi}_{A1} = \frac{\sqrt{2}}{4} [1 \quad -1], \quad \bar{\varphi}_{A2} = \frac{\sqrt{2}}{4} [1 \quad 1], \quad \bar{\varphi}_{A3} = \frac{\sqrt{2}}{4} [-1 \quad -1] \text{ and } \bar{\varphi}_{A4} = \frac{\sqrt{2}}{4} [-1 \quad 1]. \quad (5-9)$$

The eigen deformation field for φ_A is derived from Eq. (5-4) and Eq. (5-9),

$$\varphi_A = [\varphi_{A1} \quad \varphi_{A2}]^T = \frac{\sqrt{2}}{4} [y \quad -x]^T. \quad (5-10)$$

Also, the shear deformation field φ_B and φ_C is obtained by using rigid body rotation field φ_r in Eq. (5-5),

$$\varphi_B = \varphi_A - \varphi_r = \frac{\sqrt{2}}{2} [y \quad 0]^T \text{ and } \varphi_C = \varphi_A + \varphi_r = \frac{\sqrt{2}}{2} [0 \quad x]^T. \quad (5-11)$$

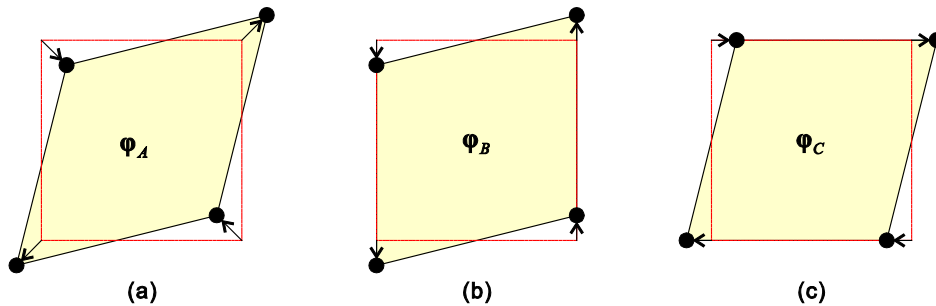


Figure 5-3. Isoparametric bodies subjected to the three types of shear deformation.

Following the Eqs. (5-6) and (5-7), the linear and nonlinear terms of the Green-Lagrange strain for $\boldsymbol{\varphi}_A$, $\boldsymbol{\varphi}_B$ and $\boldsymbol{\varphi}_C$ are denoted as,

$${}_0e_{11}^A = \delta_0 e_{11}^A = 0, \quad {}_0e_{22}^A = \delta_0 e_{22}^A = 0, \quad {}_0e_{12}^A = \delta_0 e_{12}^A = \frac{\sqrt{2}}{4}, \quad \delta_0 \eta_{11}^A = \frac{1}{8}, \quad \delta_0 \eta_{22}^A = \frac{1}{8}, \quad \delta_0 \eta_{12}^A = 0, \quad (5-12)$$

$${}_0e_{11}^B = \delta_0 e_{11}^B = 0, \quad {}_0e_{22}^B = \delta_0 e_{22}^B = 0, \quad {}_0e_{12}^B = \delta_0 e_{12}^B = \frac{\sqrt{2}}{4}, \quad \delta_0 \eta_{11}^B = 0, \quad \delta_0 \eta_{22}^B = \frac{1}{2}, \quad \delta_0 \eta_{12}^B = 0, \quad (5-13)$$

$${}_0e_{11}^C = \delta_0 e_{11}^C = 0, \quad {}_0e_{22}^C = \delta_0 e_{22}^C = 0, \quad {}_0e_{12}^C = \delta_0 e_{12}^C = \frac{\sqrt{2}}{4}, \quad \delta_0 \eta_{11}^C = \frac{1}{2}, \quad \delta_0 \eta_{22}^C = 0, \quad \delta_0 \eta_{12}^C = 0. \quad (5-14)$$

Substituting Eqs. (5-12), (5-13) and (5-14) into Eq. (5-2), the internal virtual works for three types of shear deformation are finally obtained as a function of stress distributions,

$$\left\{ \begin{array}{l} \delta \Pi_{linear} \Big|_{\mathbf{u}=\boldsymbol{\varphi}_A} = 2G, \quad \delta \Pi_{nonlinear} \Big|_{\mathbf{u}=\boldsymbol{\varphi}_A} = \frac{1}{8} \int_{0V} ({}_0^t S_{11} + {}_0^t S_{22}) d^0V \\ \delta \Pi_{linear} \Big|_{\mathbf{u}=\boldsymbol{\varphi}_B} = 2G, \quad \delta \Pi_{nonlinear} \Big|_{\mathbf{u}=\boldsymbol{\varphi}_B} = \frac{1}{2} \int_{0V} {}_0^t S_{22} d^0V \\ \delta \Pi_{linear} \Big|_{\mathbf{u}=\boldsymbol{\varphi}_C} = 2G, \quad \delta \Pi_{nonlinear} \Big|_{\mathbf{u}=\boldsymbol{\varphi}_C} = \frac{1}{2} \int_{0V} {}_0^t S_{11} d^0V \end{array} \right. \quad (5-15)$$

Here we should remind that 4-node 2D plane element has only one shear eigenvector. In other words, the superposition of two eigenvectors ($\boldsymbol{\varphi}_A$ and $\boldsymbol{\varphi}_C$) have to represent shear deformation $\boldsymbol{\varphi}_B$ and $\boldsymbol{\varphi}_C$. In linear analysis or nonlinear analysis without stress distributions, the shear deformations have same internal virtual works $2G$, and the representation is sufficient. However, when the internal virtual works become different each other by the effect of stress distributions, the two eigenvectors cannot represent them anymore. Consequently, the stress distributions yield the deficiency of the shear eigenvector.

5.4 Eigenvalue Analysis

In order to verify the analytical results and to extend the insight, we perform the eigenvalue analysis for plane stress elements. Now we use terms; total stiffness matrix, linear stiffness matrix and nonlinear stiffness matrix. The total stiffness matrix \mathbf{K} are obtained from the internal virtual work $\delta \Pi$ in Eq. (5-2), and the linear stiffness matrix \mathbf{K}_L and the nonlinear stiffness matrix \mathbf{K}_N respectively mean the linear and nonlinear component of internal virtual work, $\delta \Pi_{linear}$ and $\delta \Pi_{nonlinear}$.

We demonstrate eigenvalue analysis for the nonlinear stiffness matrix \mathbf{K}_N . Remind that stress distributions only have an effect on the nonlinear stiffness matrix \mathbf{K}_N . In other words, the eigenpairs of the linear stiffness matrix \mathbf{K}_L are not varied by stress distributions and already known in Fig.5-1. For that reason, to separately analyze the nonlinear stiffness matrix \mathbf{K}_N is more obvious for considering additional effects from the stress

distributions.

We consider a single 4-node plane stress element has isoparametric body. The free displacement boundary conditions are applied at all nodes. The linear elastic material with Young's modulus $E = 10^6$ and zero Poisson's ratio is used. The following three case of stress distributions are considered:

- The constant ${}^tS_{11} = 100000$ is applied on the whole area.
- The constant ${}^tS_{22} = 100000$ is applied on the whole area.
- The constant ${}^tS_{12} = 100000$ is applied on the whole area.

In order to investigate physical meaning of the results, we introduce the eigen decomposition of the linear and nonlinear stiffness matrix,

$$\mathbf{K}_L = \sum_{i=1}^8 \bar{\boldsymbol{\varphi}}_i \bar{\lambda}_i \bar{\boldsymbol{\varphi}}_i^T \quad \text{and} \quad \mathbf{K}_N = \sum_{i=1}^8 \boldsymbol{\varphi}_i \lambda_i \boldsymbol{\varphi}_i^T, \quad (5-16)$$

in which $\bar{\boldsymbol{\varphi}}_i$ and $\bar{\lambda}_i$ are the eigenpairs obtained from the linear stiffness matrix in Fig. 5-1, and $\boldsymbol{\varphi}_i$ and λ_i are the eigenpairs obtained from the nonlinear stiffness matrix in Fig. 5-4.

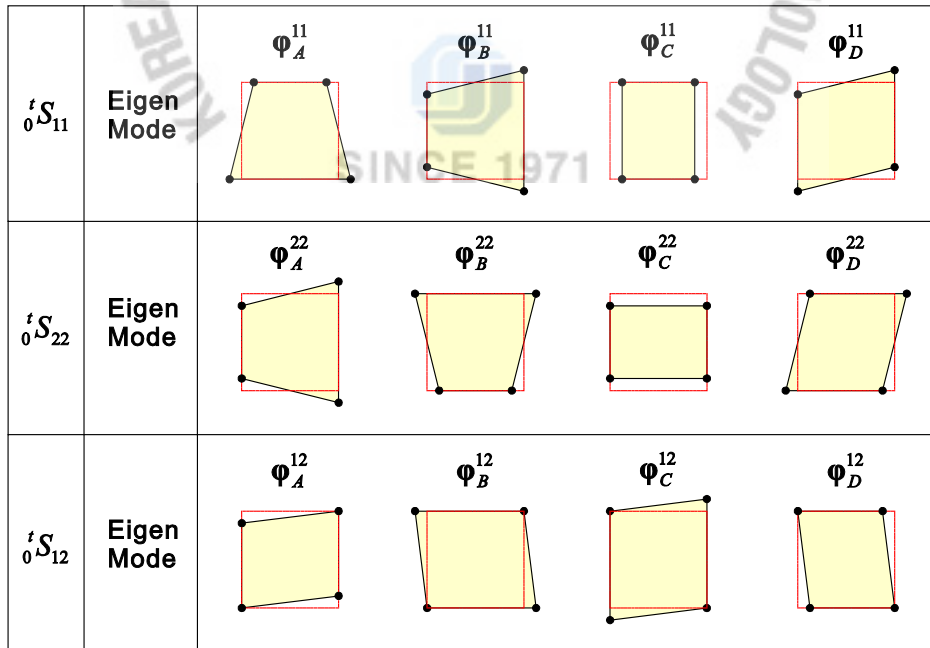


Figure 5-4. The numerical results of eigenvalue analysis for nonlinear stiffness matrix with respective stress component.

Fig. 5-4 displays the evaluated eigenpairs except the eigenpairs which have zero eigenvalue for each demonstrative condition. Let us consider the numerical results for ${}^tS_{11}$. We rewritten the total stiffness matrix \mathbf{K} by using Eq. (5-16) and numerical results,

$$\mathbf{K} = \sum_{i=1}^8 \bar{\varphi}_i \bar{\lambda}_i \bar{\varphi}_i^T + \varphi_A^{11} \lambda_A \varphi_A^{11T} + \varphi_B^{11} \lambda_B \varphi_B^{11T} + \varphi_C^{11} \lambda_C \varphi_C^{11T} + \varphi_D^{11} \lambda_D \varphi_D^{11T}. \quad (5-17)$$

We can easily know that the eigenmodes φ_A^{11} , φ_B^{11} and φ_C^{11} are superposed to the eigenmodes $\bar{\varphi}_4$, $\bar{\varphi}_5$, $\bar{\varphi}_6$ because they are individually same eigenvectors. In other words, the eigenmodes φ_A^{11} , φ_B^{11} and φ_C^{11} of the nonlinear stiffness matrix make the x -bending, y -bending and x -stretch actions stiffer. In order to investigate the role of φ_D^{11} , we split φ_D^{11} into two eigenvectors $\bar{\varphi}_3$ and $\bar{\varphi}_8$ by using Eq. (5-11),

$$\varphi_D^{11} = \bar{\varphi}_3 + \bar{\varphi}_8. \quad (5-18)$$

Then, the last term of Eq. (5-17) is denoted as,

$$\varphi_D^{11} \lambda_D \varphi_D^{11T} = \bar{\varphi}_3 \lambda_D \bar{\varphi}_3^T + \bar{\varphi}_8 \lambda_D \bar{\varphi}_8^T + \bar{\varphi}_3 \lambda_D \bar{\varphi}_8^T + \bar{\varphi}_8 \lambda_D \bar{\varphi}_3^T. \quad (5-19)$$

The component of the linear eigenvector $\bar{\varphi}_3 \lambda_D \bar{\varphi}_3^T$ makes the rigid body rotation action stiffer and the component of the linear eigenvector $\bar{\varphi}_8 \lambda_D \bar{\varphi}_8^T$ makes the shear action stiffer. The residual components $\bar{\varphi}_3 \lambda_D \bar{\varphi}_8^T$ and $\bar{\varphi}_8 \lambda_D \bar{\varphi}_3^T$ make following effects;

- Considering with analytical investigation in Section 3, they cause the deficiency of the shear eigenvector.
- The total stiffness matrix \mathbf{K} cannot be decomposed by linear eigenvectors $\bar{\varphi}_i$ due to the residual components $\bar{\varphi}_3 \lambda_D \bar{\varphi}_8^T$ and $\bar{\varphi}_8 \lambda_D \bar{\varphi}_3^T$. For that reason, they cause the distorted eigenvectors.

In summary, ${}^tS_{11}$ has the role to make the x -bending, y -bending, x -stretch, rigid body rotation and shear actions stiffer, and the components $\bar{\varphi}_3 \lambda_D \bar{\varphi}_3^T$, $\bar{\varphi}_3 \lambda_D \bar{\varphi}_8^T$ and $\bar{\varphi}_8 \lambda_D \bar{\varphi}_3^T$ in $\varphi_D^{11} \lambda_D \varphi_D^{11T}$ yield the drawbacks.

The roles of ${}^tS_{22}$ symmetrically same with ${}^tS_{11}$. Thus, we skip the consideration of the numerical results for ${}^tS_{22}$.

Consider the numerical results for ${}^tS_{12}$, in Fig. 5-4. We rewritten the total stiffness matrix \mathbf{K} by using Eq. (5-16) and numerical results,

$$\mathbf{K} = \sum_{i=1}^8 \bar{\varphi}_i \bar{\lambda}_i \bar{\varphi}_i^T + \varphi_A^{12} \lambda_A \varphi_A^{12T} + \varphi_B^{12} \lambda_B \varphi_B^{12T} + \varphi_C^{12} \lambda_C \varphi_C^{12T} + \varphi_D^{12} \lambda_D \varphi_D^{12T}. \quad (5-20)$$

The eigenvectors φ_A^{12} , φ_B^{12} , φ_C^{12} and φ_D^{12} can be decomposed by combinations of $\bar{\varphi}_3$, $\bar{\varphi}_6$, $\bar{\varphi}_7$, $\bar{\varphi}_8$ as Eq. (5-18). Then, the components of the linear eigenvectors $\bar{\varphi}_3 \bar{\varphi}_3^T$, $\bar{\varphi}_6 \bar{\varphi}_6^T$, $\bar{\varphi}_7 \bar{\varphi}_7^T$, $\bar{\varphi}_8 \bar{\varphi}_8^T$ and the residual components are obtained by similar expansion in Eq. (5-19). The components of the linear eigenvectors make effects

on the each action, the rigid body rotation, x -stretch, y -stretch and shear actions. The residual components cause the distorted eigenvectors.

5.5 Eigen Recomposition Method

Based on the studies in above sections, the nonlinear stiffness matrix \mathbf{K}_N has intrinsic drawbacks which have a bad effect on the nonlinear performance. In order to modify the drawbacks, we propose simple numerical method; eigen recomposition.

The incremental equilibrium equation can be stated as

$$(\mathbf{K}_L + \mathbf{K}_N)\mathbf{U} = \mathfrak{R} - \mathbf{F}, \quad (5-21)$$

in which \mathbf{U} is the nodal displacement vector, \mathfrak{R} is the external virtual work, and \mathbf{F} is internal force vector, as defined in Eq. (4-36).

The nonlinear stiffness matrix \mathbf{K}_N can be rewritten by using eigenvalue decomposition theorem,

$$\mathbf{K}_N = \sum_{i=1}^6 \lambda_i \boldsymbol{\varphi}_i \boldsymbol{\varphi}_i^T, \quad (5-22)$$

where λ_i and $\boldsymbol{\varphi}_i$ are exact eigenvalues and eigenvectors corresponding to the nonlinear stiffness matrix \mathbf{K}_N .

Here we define the assumed eigenvector $\bar{\boldsymbol{\varphi}}_i$ and the estimated eigenvalue $\bar{\lambda}_i$. In general, the assumed eigenvector cannot be predicted due to the mesh distortion. However, in case of 2D beam element, the assumed eigenvector can easily denoted as,

$$\bar{\boldsymbol{\varphi}}_1 = \begin{bmatrix} -\frac{\sqrt{2}}{2} & 0 & 0 & \frac{\sqrt{2}}{2} & 0 & 0 \end{bmatrix}^T, \quad \bar{\boldsymbol{\varphi}}_2 = \begin{bmatrix} 0 & 0 & -\frac{\sqrt{2}}{2} & 0 & 0 & \frac{\sqrt{2}}{2} \end{bmatrix}^T,$$

and $\bar{\boldsymbol{\varphi}}_3 = \begin{bmatrix} 0 & -\frac{1}{2} & \frac{1}{2} & 0 & \frac{1}{2} & \frac{1}{2} \end{bmatrix}^T,$ (5-23)

in which $\bar{\boldsymbol{\varphi}}_1$ is the assumed eigenvector corresponding to the stretch mode, $\bar{\boldsymbol{\varphi}}_2$ is the bending mode, and $\bar{\boldsymbol{\varphi}}_3$ is the shear mode. The assumed eigenvectors corresponding to the rigid body modes are not considered. Then the estimated eigenvalue $\bar{\lambda}_i$ is defined as

$$\bar{\lambda}_i = \bar{\boldsymbol{\varphi}}_i^T \mathbf{K}_N \bar{\boldsymbol{\varphi}}_i. \quad (5-24)$$

Finally, the recomposed nonlinear stiffness matrix $\bar{\mathbf{K}}_N$ is obtained by

$$\bar{\mathbf{K}}_N = \sum_{i=1}^8 \bar{\lambda}_i \bar{\boldsymbol{\varphi}}_i \bar{\boldsymbol{\varphi}}_i^T \quad \text{with} \quad \bar{\lambda}_i = \bar{\boldsymbol{\varphi}}_i^T \mathbf{K}_N \bar{\boldsymbol{\varphi}}_i, \quad (5-25)$$

and the modified incremental equilibrium equation is

$$(\mathbf{K}_L + \bar{\mathbf{K}}_N)\mathbf{U} = \mathfrak{R} - \mathbf{F}. \quad (5-26)$$

5.6 Numerical Studies

In this section, we present four numerical examples to demonstrate the performance of the eigen recomposition method: straight cantilever, right angle frame, portal frame, and offshore jacket problems. The standard full Newton-Raphson iterative scheme is used in all the examples and the following displacement criterion is used to test for convergence,

$$\frac{\|\mathbf{U}_0\|_2}{\|\mathbf{U}\|_2} \leq \varepsilon_d, \quad (5-27)$$

where \mathbf{U}_0 is an incremental displacement vector, \mathbf{U} is a total displacement vector, $\|\cdot\|_2$ is Euclidean norm, and ε_d is an error tolerance. We stop the iterations when $\varepsilon_d = 0.0001$.

5.6.1 Straight Cantilever Problem

We consider a straight cantilever beam with a length of $L = 100\text{cm}$ and a square cross-section, as shown in Fig. 5-5. The beam is modeled by using ten 2-node beam elements. The linear elastic material with Young's modulus $E = 2.0 \times 10^5 \text{N/cm}^2$ and Poisson's ratio $\nu = 0$ is used. The displacement boundary condition $u = w = \theta = 0$ is applied at $x = 0\text{cm}$. Two load cases are considered:

- Load Case I: The shear force F_z is applied at the free tip ($x = 100\text{cm}$).
- Load Case II: The bending moment M_y is applied at the free tip ($x = 100\text{cm}$).

Fig. 5-6(a) and (b) shows the numerical results for Load Case I. Fig. 5-6(a) displays the required number of Newton-Raphson iterations under the single load incremental step. It exhibits that the proposed method enhances the capacity of large load increments and reduces the required number of iterations. Fig. 5-6(b) displays the load-displacement curves. The reference is calculated by using 20 load incremental steps without the eigen recomposition method. The solution reliability of the proposed methods is observed.

Fig. 5-7(a) and (b) displays the numerical results for Load Case II. Fig. 5-7(a) shows the total number of Newton-Raphson iterations required under the five load incremental steps. The proposed method reduces the required number of iterations. Fig. 5-7(b) shows the load-displacement curves. The reference is calculated by using 20 load incremental steps without the eigen recomposition method. The solution reliability of the proposed methods is exhibited.

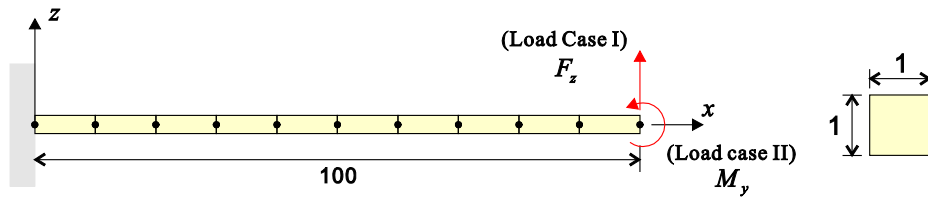


Figure 5-5. Straight cantilever problem with the beam element model (10 beam elements) and square cross-section (unit: *cm*).

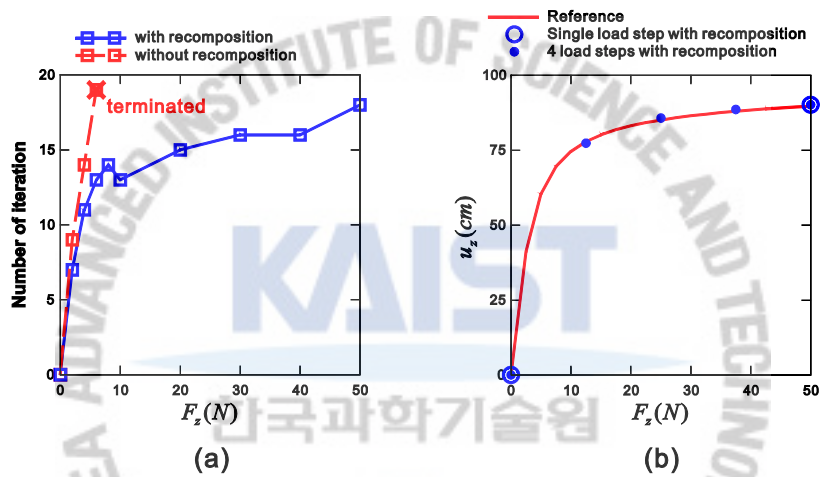


Figure 5-6. Numerical results for Load Case I in the straight cantilever problem: (a) number of iteration used according to the applied load, (b) load-displacement curves.

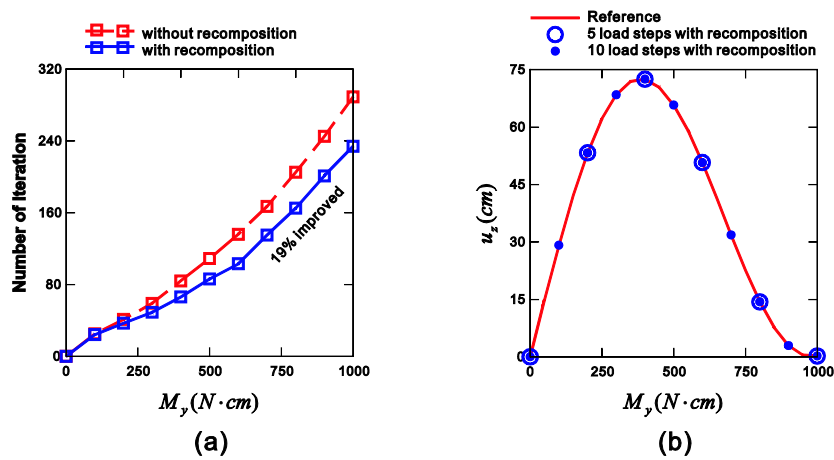


Figure 5-7. Numerical results for Load Case II in the straight cantilever problem: (a) number of iteration used according to the applied load, (b) load-displacement curves.

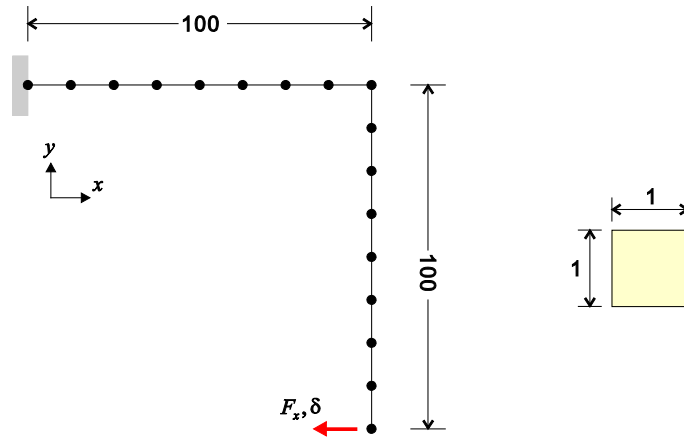


Figure 5-8. Right angle frame problem with the beam element model (16 beam elements) and square cross-section (unit: *cm*).

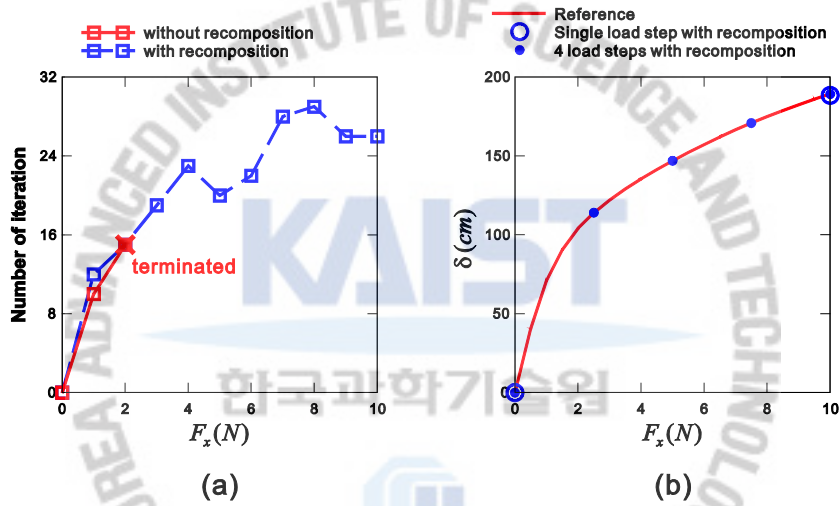


Figure 5-9. Numerical results in the right angle frame problem: (a) number of iteration used according to the applied load, (b) load-displacement curves.

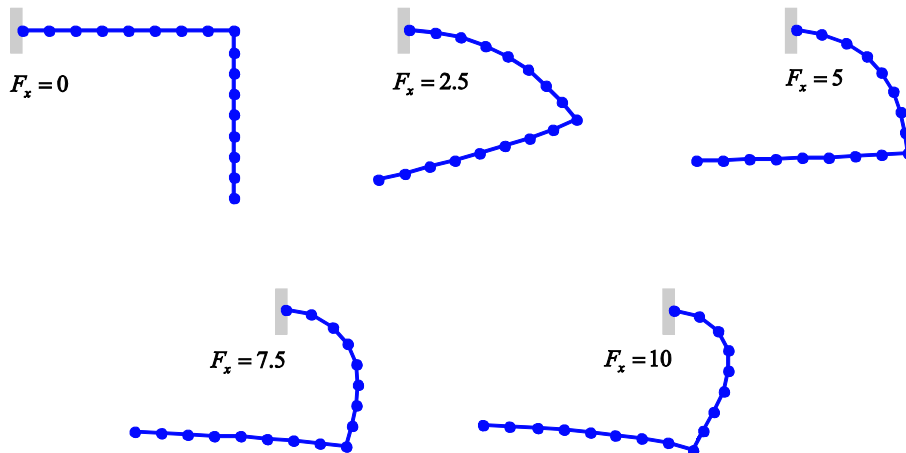


Figure 5-10. Deformed shapes in the right angle frame problem.

5.6.2 Right Angle Frame Problem

A right angle frame structure with square cross-section is considered as described in Fig. 5-8. The structure is modeled by using 16 beam elements. The linear elastic material with Young's modulus $E = 2.0 \times 10^5 N / cm^2$ and Poisson's ratio $\nu = 0$ is used. The displacement boundary condition $u = w = \theta = 0$ is applied at the node on the gray colored area in Fig. 5-8. The x -directional load F_x is applied at the end tip node.

Fig. 5-9(a) shows the required number of Newton-Raphson iterations under the single load incremental step. It exhibits that the proposed method enhances the capacity of large load increments and reduces the required number of iterations. Fig. 5-9(b) illustrates the load-displacement curves. The reference is calculated by using 20 load incremental steps without the eigen recomposition method. The solution reliability of the proposed methods is displayed. The corresponding deformed shapes are plotted in Fig. 5-10.

5.6.3 Portal Frame Problem

We consider a portal frame structure with rectangular cross-section, as shown in Fig. 5-11. The structure is modeled by using 24 beam elements. The linear elastic material with Young's modulus $E = 2.1 \times 10^7 N / cm^2$ and Poisson's ratio $\nu = 0.3$, and the cross-sectional shear correction factor $k = 5/6$ is used. The displacement boundary condition $u = w = \theta = 0$ is applied at the nodes on the gray colored area in Fig. 5-11. The y -directional concentrate load F_y is applied at the center of the structure.

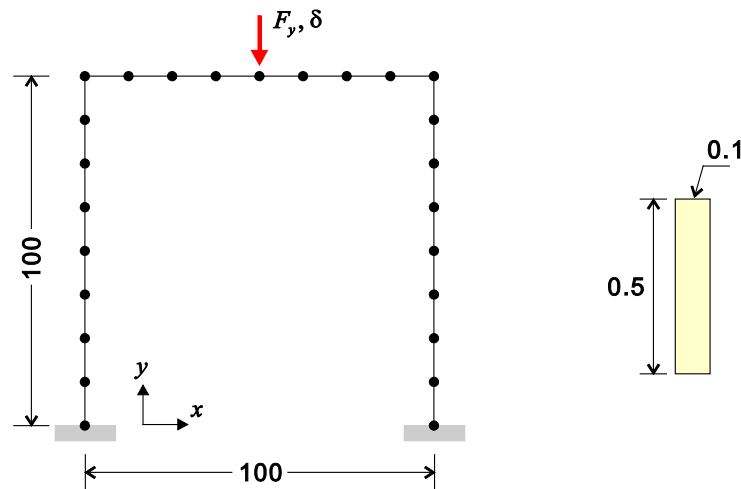


Figure 5-11. Portal frame problem with the beam element model (24 beam elements) and rectangular cross-section (unit: cm).

Fig. 5-12 illustrates the load-displacement curves calculated through incrementally controlling the vertical displacement δ . It exhibits that the proposed method works well in displacement control scheme. Also, the numerical results are in good agreement with results of the co-rotational formulation obtained by Li [68]. Note that the used beam model without proposed method cannot obtain the solution higher than $\delta = 40\text{cm}$ due to the convergence problems. The solution procedure terminates even though a lot of increment steps are used. This upper bound of the convergence can be broken by the proposed method. The corresponding deformed shapes are illustrated in Fig. 5-13.

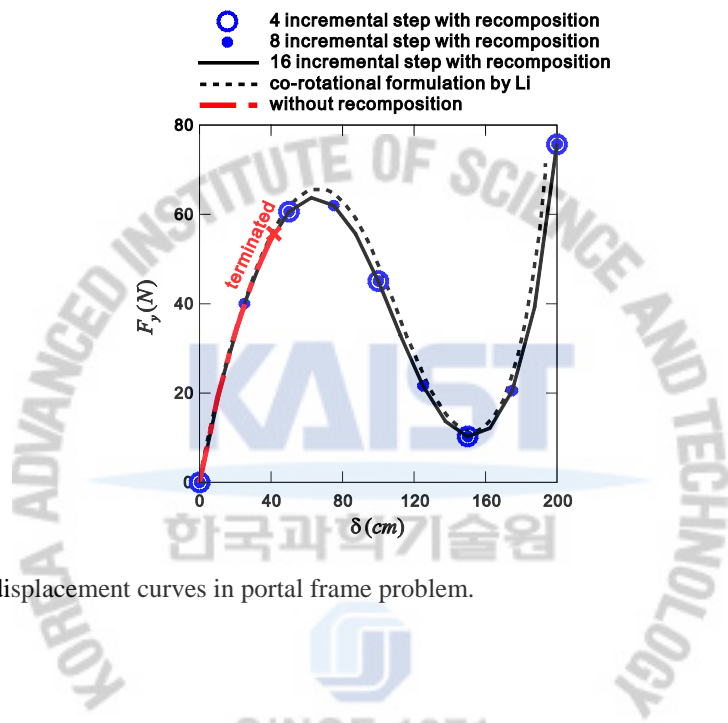


Figure 5-12. Load-displacement curves in portal frame problem.

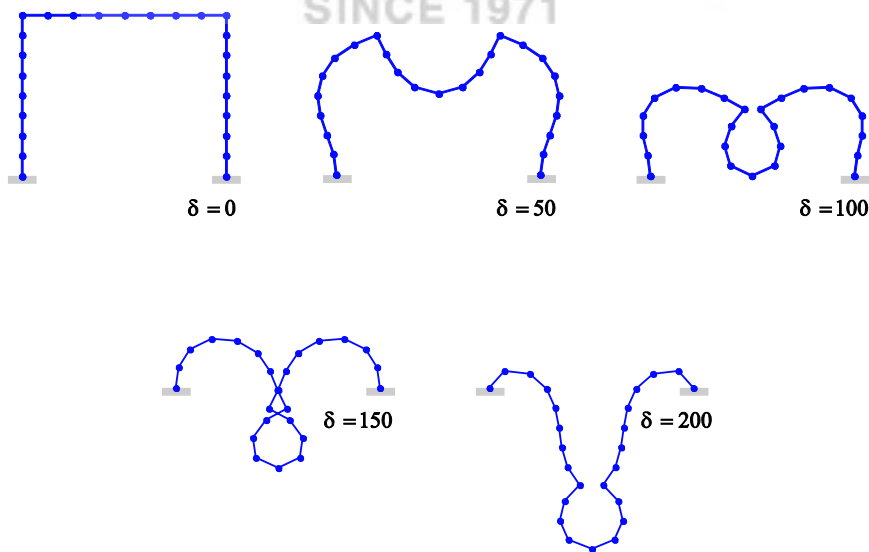


Figure 5-13. Deformed shapes in the portal frame problem.

5.6.4 Offshore Jacket Problem

Finally, an offshore jacket structure that consists of 22 beam members of a square cross-section is considered as described in Fig. 5-14. Each beam member is modeled by using four beam elements. The linear elastic material with Young's modulus $E = 2.0 \times 10^{11} \text{ N/m}^2$ and Poisson's ratio $\nu = 0.3$ is used. The displacement boundary condition $u = w = \theta = 0$ is applied at the node on the gray colored area in Fig. 5-14. The x -directional concentrate load F_x is applied at the center of the top beam member. The x -displacement δ_x at the node marked by the red dot is observed.

Fig. 5-15 displays the load-displacement curves calculated through controlling the displacement u_x . The eigen recomposition method enables to accurately predict the complicated buckling behaviors of the structure with only two incremental steps. The single incremental step can also give reasonable solution. Fig. 5-16 illustrates the deformed shapes obtained using 20 and 40 incremental steps without proposed method, and using single and two incremental steps with the proposed method.

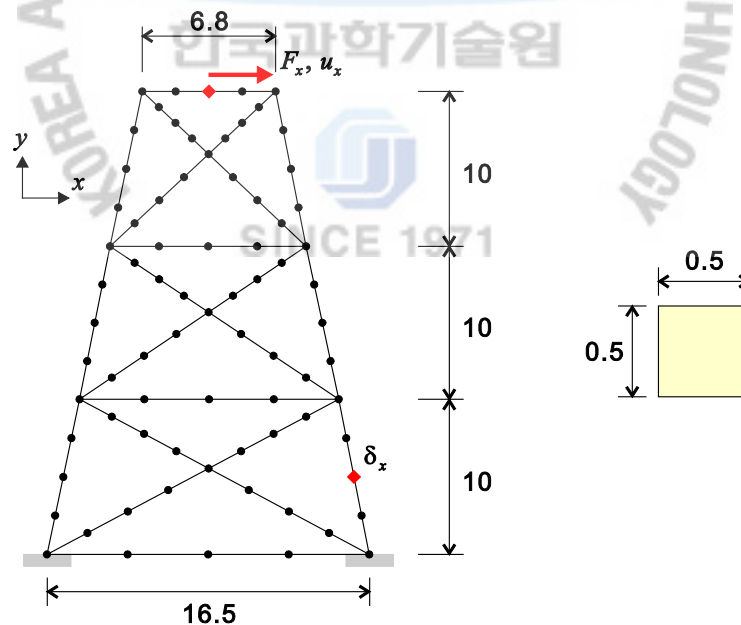


Figure 5-14. Offshore jacket problem with the beam element model (88 beam elements) and square cross-section (unit: m).

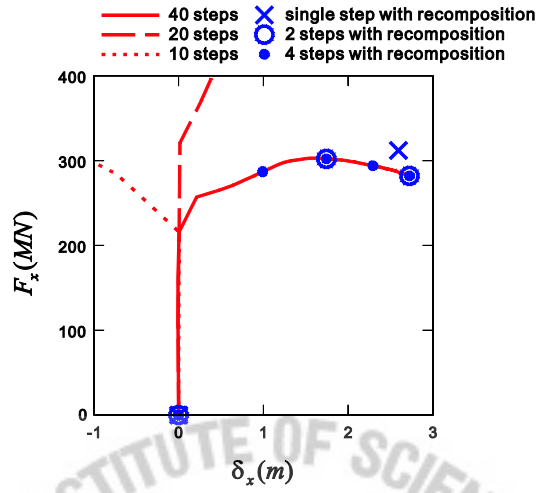


Figure 5-15. Load-displacement curves in the offshore jacket problem.

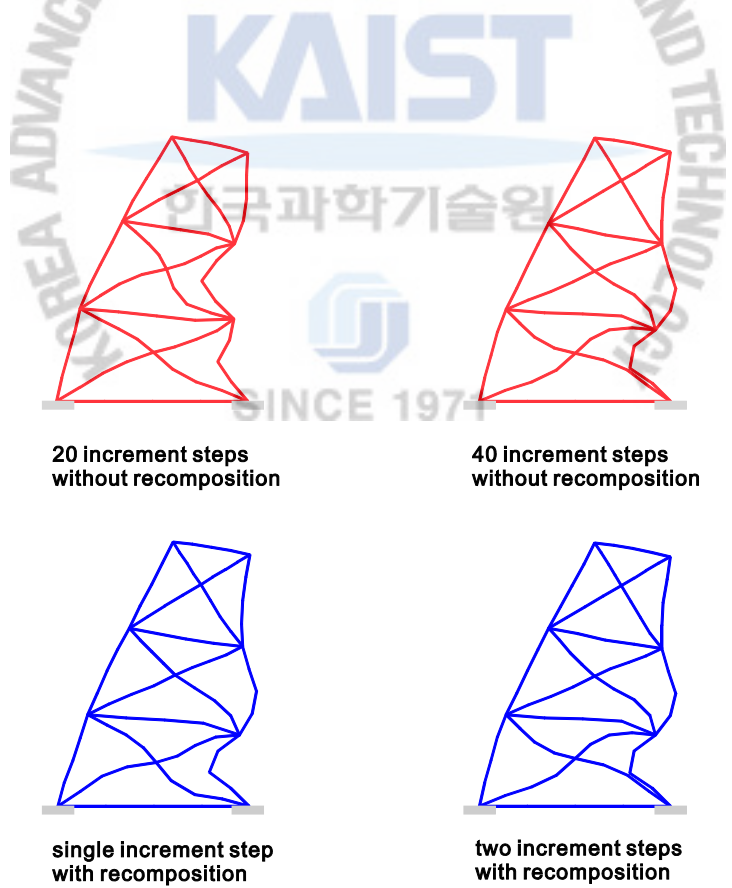


Figure 5-16. Deformed shapes in the offshore jacket problem.

5.7 Concluding Remarks

In this chapter, we presented a new numerical method to improve nonlinear performance: the eigen recomposition. The superior nonlinear performance of proposed method was demonstrated through several numerical examples. In this study, we implement only 2D beam element case for feasibility study, but it can be easily extended to 3D curved beam element case. Furthermore, the proposed method is element-independent, thus it can be easily applied to all of the element.



Chapter 6. Conclusions & Future Works

6.1 Conclusions

The objective in this thesis is to develop the continuum mechanics based beam elements for linear and nonlinear analysis.

In chapter 2, we introduce continuum mechanics based beam finite elements with warping displacements. We present the general formulation including how the geometry and displacements are defined and how warping displacements are efficiently accounted for. The novel features of the beam element are the simple and straightforward formulation, the inclusion of fully coupled warping effects, the ability of handling complicated geometry and only one additional degree of freedom at each beam node. The various numerical results show the effectiveness of the beam elements. Especially, excellent modeling capabilities and solution accuracy of the proposed beam element is observed.

In chapter 3, we propose a new modeling method to construct continuous warping displacement fields for beams with discontinuously varying arbitrary cross-sections. The warping displacement is represented by a combination of three basis warping functions (one free warping function and two interface warping functions) accompanying the corresponding three warping DOFs that are interpolated along the beam length. We also introduce a new numerical method that calculates the free warping functions and the twisting centers simultaneously. Using this method and Lagrange multipliers, a set of coupled equations is formulated to obtain interface warping functions.

In chapter 4, a nonlinear formulation of the continuum mechanics based beam elements is presented and their performance in general nonlinear analyses that focused on large twisting behaviors is demonstrated. Since the beam elements are derived from assemblages of 3D solid elements, they have inherently advanced modeling capabilities in the analysis of complicated 3D beam geometries including curved and twisted geometries, varying cross-sections, eccentricity, and arbitrary cross-sectional shapes. The total Lagrangian formulation is used to obtain the complete tangent stiffness matrix and internal load vector with the warping displacements. The resulting formulation can consider the fully coupled nonlinear behaviors of bending, shearing, stretching, twisting, and warping. In particular, large twisting and lateral buckling behaviors can be accurately predicted and, in the beam formulation, the Wagner effect is implicitly included, unlike other beam elements. Through various numerical examples, the strong modeling and predictive capabilities of the nonlinear formulation of the continuum mechanics based beam elements were demonstrated for general nonlinear analysis. The most valuable asset of the proposed beam elements is their excellent analysis capability in large twisting problems.

In chapter 5, we present a new numerical method to improve nonlinear performance: the eigen recomposition. The superior nonlinear performance of proposed method is demonstrated through several numerical examples. In this study, we implement only 2D beam element case for feasibility study, but it can be easily extended to 3D curved beam element case. Furthermore, the proposed method is element-independent, thus it can be easily applied to all of the element.

6.2 Future Works

While some key points of research in linear and nonlinear analysis of beams are addressed in this thesis, there are still a number of outstanding improvements should be pursued in future works.

First, implementation for composite material is recommended. The continuum mechanics based beam elements are formulated by integrating the stiffness of individual sub beams. For this reason, the composite material model can be easily implemented by applying different material models respectively. However, in order to analysis a twisting action, a free warping function for the composite cross-section should be suggested. The extension to the more precise composite model, zigzag or slip composite, is also valuable.

Second, consideration of cross-sectional distortion mode is recommended. In-plane distortion of the cross-section is frequently observed in thin-walled beam structures. For accounting the correct critical load for buckling failure, the in-plane distortion of the cross-section should be implemented. A crucial point is the evaluation of in-plane distortion modes with minimum addition.

Third, implementation of Jourasky warping theory is recommended. According to Jourasky warping theory, the consideration of the secondary warping effect will provide more accurate prediction of twisting behaviors. In order to implement to the continuum formulation, the evaluation of the secondary warping function for arbitrary cross-section is investigated.

Fourth, implementation for dynamic analysis is recommended. The continuum mechanics based beam elements have additional warping DOF and corresponding external force component. For evaluating the mass matrix for the element, the mass component conjugated with the warping DOF and external force component should be obtained.

Fifth, nonlinear implementation for the proposed new warping model for discontinuously varying cross-section, is recommended. The proposed model can accurately predict the stress distribution. Thus, the analysis for the elastoplastic material condition should be interesting subject.

Sixth, to investigate characteristics of twisting actions is recommended. In new application fields, nano- and bio-fields, twisted structures are frequently observed. Accordingly, To investigate the mechanics of twisted structure and their properties are attractive subject. Through superior nonlinear performance of the presented

beam elements, the nonlinear characteristics of twisting actions, for examples poynting and swift effects, can be studied.

Seventh, post-buckling analysis is recommended. Through superior nonlinear performance and modeling capability of the presented beam elements, the post-buckling behavior of beam members with complicated geometries and material properties is efficiently analyzed. Especially, to predict the buckling response of the twisted structure is original and valuable result.

Eighth, extension of the eigen recomposition method is recommended. The eigen recomposition method is element-independent. It can be easily applied to all of the element, provided that the assumed eigenvector should be correctly chosen. The accurate choice of the assumed eigenvector enable many numerical methods, for examples in-plane and transverse shear locking treatment, volumetric locking treatments, improvement of mesh distortion so on.



Appendix

Appendix A. Geometry of the Wind Turbine Blade

We here give the equations to define the geometry of the wind turbine blade with a NACA airfoil. The equations for the airfoil shape are given by the NACA four-digit series.

The chord length c and blade angle β (deg.) vary depending on the local radius x

$$c = c_0 - (c_0 - c_L) \frac{x}{L} \quad \text{and} \quad \beta = \beta_0 - (\beta_0 - \beta_L) \frac{x}{L}, \quad (\text{A-1})$$

in which L is the blade length, c_0 and c_L are the chord lengths at $x=0$ and $x=L$, respectively, and β_0 and β_L are the blade angles at $x=0$ and $x=L$, respectively.

The height distribution of the airfoil with unit length is

$$z_t = \frac{h}{0.2} (0.2969\sqrt{s} - 0.1260s - 0.3516s^2 + 0.2843s^3 - 0.1015s^4), \quad (\text{A-2})$$

where h is the maximum height of the airfoil.

The mean camber line is defined by the maximum camber m and its position p ,

$$z_c = \begin{cases} m \frac{s}{p} (2p - s), & \text{for } 0 \leq s \leq p \\ m \frac{1-s}{(1-p)^2} (1 + s - 2p), & \text{for } p \leq s \leq 1 \end{cases} \quad (\text{A-3})$$

The coordinates for the airfoil upper mid-surface (y_U, z_U) and lower mid-surface (y_L, z_L) are obtained by

$$\begin{bmatrix} y_U \\ z_U \end{bmatrix} = c \begin{bmatrix} \cos \beta & -\sin \beta \\ \sin \beta & \cos \beta \end{bmatrix} \begin{bmatrix} s - z_t \sin \theta \\ z_c + z_t \cos \theta \end{bmatrix}, \quad \begin{bmatrix} y_L \\ z_L \end{bmatrix} = c \begin{bmatrix} \cos \beta & -\sin \beta \\ \sin \beta & \cos \beta \end{bmatrix} \begin{bmatrix} s + z_t \sin \theta \\ z_c - z_t \cos \theta \end{bmatrix}$$

with $\theta = \arctan\left(\frac{dz_c}{ds}\right)$. (A-4)

Appendix B. Wagner Strain Components for Prismatic and Pure Torsion Condition

The Wagner strain is implicitly included in the geometric nonlinear formulation of the continuum mechanics based beam elements. In order to verify this, the Green-Lagrange strain in the beam formulation is analytically investigated. Two configurations of a rectangular prismatic beam with free warping at time 0 and t are considered: see Fig. A-1. Time 0 and t correspond to undeformed and twisted configurations, respectively.

The material position vector can be rewritten in the following continuum form (non-discretized form) through deduction from Eq. (1), as follows

$${}^t\mathbf{x} = {}^t\mathbf{x}_r + \bar{y}{}^t\mathbf{V}_{\bar{y}} + \bar{z}{}^t\mathbf{V}_{\bar{z}} + {}^t f {}^t\mathbf{V}_{\bar{x}}, \quad (\text{A-5})$$

in which ${}^t\mathbf{x}_r$ is the position of the beam reference line at time t , ${}^t\mathbf{V}_{\bar{x}}$, ${}^t\mathbf{V}_{\bar{y}}$, and ${}^t\mathbf{V}_{\bar{z}}$ are the director vectors \bar{y} and \bar{z} denote the position in the cross-sectional plane, and ${}^t f$ is the warping displacement.

Both configurations in Fig. A-1 are defined using the following vectors

$${}^0\mathbf{x}_r = {}^t\mathbf{x}_r = \begin{bmatrix} x \\ 0 \\ 0 \end{bmatrix}, \quad {}^0\mathbf{V}_{\bar{x}} = {}^t\mathbf{V}_{\bar{x}} = \begin{bmatrix} 1 \\ 0 \\ 0 \end{bmatrix}, \quad {}^0\mathbf{V}_{\bar{y}} = \begin{bmatrix} 0 \\ 1 \\ 0 \end{bmatrix}, \quad {}^0\mathbf{V}_{\bar{z}} = \begin{bmatrix} 0 \\ 0 \\ 1 \end{bmatrix}, \quad {}^t\mathbf{V}_{\bar{y}} = \begin{bmatrix} 0 \\ \cos\theta_x \\ \sin\theta_x \end{bmatrix}, \quad {}^t\mathbf{V}_{\bar{z}} = \begin{bmatrix} 0 \\ -\sin\theta_x \\ \cos\theta_x \end{bmatrix}. \quad (\text{A-6})$$

Using Eq. (A-6) in Eq. (A-5), the material position vectors at time 0 and t are obtained

$${}^0\mathbf{x} = \begin{bmatrix} x \\ \bar{y} \\ \bar{z} \end{bmatrix} \quad \text{and} \quad {}^t\mathbf{x} = \begin{bmatrix} x + {}^t f \\ \bar{y} \cos\theta_x - \bar{z} \sin\theta_x \\ \bar{y} \sin\theta_x + \bar{z} \cos\theta_x \end{bmatrix}. \quad (\text{A-7})$$

Substituting Eq. (A-7) into Eq. (4-23), the covariant base vectors (${}^0\mathbf{g}_1$ and ${}^t\mathbf{g}_1$) are obtained

$${}^0\mathbf{g}_1 = \begin{bmatrix} \partial x / \partial r \\ 0 \\ 0 \end{bmatrix} \quad \text{and} \quad {}^t\mathbf{g}_1 = \begin{bmatrix} \partial x / \partial r + \partial {}^t f / \partial r \\ \partial \theta_x / \partial r (-\bar{y} \sin\theta_x - \bar{z} \cos\theta_x) \\ \partial \theta_x / \partial r (\bar{y} \cos\theta_x - \bar{z} \sin\theta_x) \end{bmatrix}, \quad (\text{A-8})$$

and the covariant Green-Lagrange strain ${}^t\epsilon_{11}$ in the configuration at time t , referred to the configuration at time 0, is calculated

$${}^t\epsilon_{11} = \frac{\partial x}{\partial r} \frac{\partial {}^t f}{\partial r} + \frac{1}{2} \left(\frac{\partial {}^t f}{\partial r} \right)^2 + \frac{1}{2} (\bar{y}^2 + \bar{z}^2) \left(\frac{\partial \theta_x}{\partial r} \right)^2. \quad (\text{A-9})$$

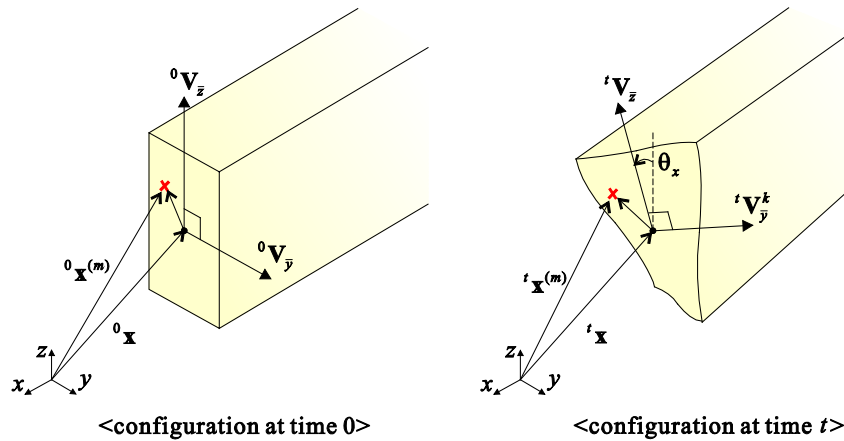


Figure A-1. Initial and deformed configurations of a prismatic straight beam.

Using Eq. (4-24), the local Green-Lagrange strain ${}^t_0\bar{\varepsilon}_{11}$ is given as follows:

$${}^t_0\bar{\varepsilon}_{11} = \frac{\partial' f}{\partial x} + \frac{1}{2} \left(\frac{\partial' f}{\partial x} \right)^2 + \frac{1}{2} (\bar{y}^2 + \bar{z}^2) \left(\frac{\partial \theta_x}{\partial x} \right)^2. \quad (\text{A-10})$$

In Eq. (A-10), it is easily identified that the Green-Lagrange strain used for the continuum mechanics based beam elements automatically contains the Wagner strain term $1/2(\bar{y}^2 + \bar{z}^2)(\partial\theta_x/\partial x)^2$.

Appendix C. Elastoplastic Constitutive Model

A simple von Mises yield criterion with associated flow rule and linear isotropic hardening is introduced here [57]. The constitutive equations used are to be listed:

- Elastoplastic strain split, $\dot{\boldsymbol{\varepsilon}} = \dot{\boldsymbol{\varepsilon}}^e + \dot{\boldsymbol{\varepsilon}}^p$.
- Elastic law, $\mathbf{S} = \mathbf{C}\boldsymbol{\varepsilon}^e$.
- Yield function definition, $\Phi = S_v^2 - \frac{2}{3}\sigma_y^2(\bar{\varepsilon}^p)$.
- Linear isotropic hardening, $\sigma_y(\bar{\varepsilon}^p) = Y_0 + H\bar{\varepsilon}^p$.
- Plastic flow rule, $\dot{\boldsymbol{\varepsilon}}^p = \dot{\gamma} \frac{\partial \Phi}{\partial \mathbf{S}}$.
- Hardening variable evolution, $\dot{\bar{\varepsilon}}^p = \dot{\gamma} \sqrt{\frac{2}{3}} S_v$.
- Loading and unloading criterion, $\dot{\gamma} \geq 0$, $\Phi \leq 0$, $\dot{\gamma}\Phi = 0$.

\mathbf{S} is a vector of the second Piola-Kirchhoff stresses, \mathbf{C} is elastic material law introduced in Eq. (4-32), S_v is the von Mises effective stress, $\bar{\varepsilon}^p$ is an accumulated plastic strain, H is the hardening modulus, $\dot{\gamma}$ is the plastic multiplier which is left indeterminate during plastic yielding. The set of evolution equations integrated with the implicit return mapping framework.

References

- [1] S.P. Timoshenko, J.N. Goodier, Theory of Elasticity, McGraw Hill, 1970.
- [2] V.Z. Vlasov, Thin-Walled Elastic Beams, Israel Program for Scientific Translations, Jerusalem, 1961.
- [3] K.J. Bathe, Finite Element Procedures, Prentice Hall, 1996.
- [4] A. Gjelsvik, The Theory of Thin Walled Bars, Wiley, New York, 1981.
- [5] R.J. Roark, Formulas for Stress and Strain, McGraw Hill, New York, 1965.
- [6] J. Argyris, P.C. Dunne, D.W. Scarpf, On large displacement-small strain analysis of structures with rotational degrees of freedom, Comput. Methods Appl. Mech. Engrg. 14 (1978) 401-451.
- [7] J. Argyris, An excursion into large rotations, Comput. Methods Appl. Mech. Engrg. 32 (1982) 85-155.
- [8] K.J. Bathe, S. Bolourchi, Large displacement analysis of three-dimensional beam structures, Int. J. Numer. Methods Engrg. 14 (1979) 961-986.
- [9] T. Belytschko, L.W. Glaum, Applications of higher order corotational stretch theories to nonlinear finite element analysis, Comput. Struct. 10 (1979) 175-182.
- [10] A. Cardona, M. Geradin, A beam finite element non-linear theory with finite rotations, Int. J. Numer. Methods Engrg. 26 (1988) 2403-2438.
- [11] E.N. Dvorkin, E. Onate, J. Oliver, On a non-linear formulation for curved Timoshenko beam elements considering large displacement/rotation increments, Int. J. Numer. Methods Engrg. 26 (1988) 1597-1613.
- [12] M.A. Crisfield, A consistent co-rotational formulation for non-linear, three-dimensional, beam-elements, Comput. Methods Appl. Mech. Engrg. 81 (1990) 131-150.

- [13] A. Ibrahimbegovic, On the choice of finite rotation parameters, *Comput. Methods Appl. Mech. Engrg.* 149 (1997) 49-71.
- [14] F. Gruttmann, W. Wagner, Finite element analysis of Saint-Venant torsion problem with exact integration of the elasto-plastic constitutive equations, *Comput. Methods Appl. Mech. Engrg.* 190 (2001) 3831-3834.
- [15] A. Dutta, D.W. White, Large displacement formulation of a three-dimensional beam element with cross-sectional warping, *Comput. Struct.* 45 (1992) 9-24.
- [16] J.C. Simo, L. Vu-Quoc, A geometrically-exact rod model incorporating shear and torsion-warping deformation, *Int. J. Solids. Struct.* 27 (1991) 371-393.
- [17] Y.L. Pi, N.S. Trahair, Inelastic torsion of steel I-beams, *J. Struct. Eng. (ASCE)* 121 (1995) 609-620.
- [18] F. Gruttmann, R. Sauer, W. Wagner, Shear stresses in prismatic beams with arbitrary cross-sections, *Int. J. Numer. Methods Engrg.* 45 (1999) 865-889.
- [19] J.L. Krahula, G.F. Lauterbach, A finite element solution for Saint-Venant torsion, *AIAA* 7 (1969) 2200-2203.
- [20] T. Kawai, The application of finite element methods to ship structures, *Comput. Struct.* 3 (1973) 1175-1194.
- [21] A.K. Noor, C.M. Andersen, Mixed isoparametric elements for Saint-Venant torsion, *Comput. Methods Appl. Mech. Engrg.* 6 (1975) 195-218.
- [22] E.N. Dvorkin, D. Celentano, A. Cuitino, G. Gioia, A Vlasov beam element, *Comput. Struct.* 33 (1989) 187-196.
- [23] K.J. Bathe, A. Chaudhary, On the displacement formulation of torsion of shafts with rectangular cross-section, *Int. J. Numer. Methods Engrg.* 18 (1982) 1565-1568.

- [24] R. Gonçalves., M. Ritto-Corrêa, D. Camotim, A new approach to the calculation of cross-section deformation modes in the framework of generalized beam theory, *Comput. Mech.* 46 (2010) 759-781.
- [25] P.S. Lee, G. McClure, A general 3D L-section beam finite element for elastoplastic large deformation analysis, *Comput. Struct.* 84 (2006) 215-229.
- [26] P.S. Lee, G. McClure, Elastoplastic large deformation analysis of a lattice steel tower structure and comparison with full-scale tests, *Int. J. Constr. Steel Res.* 63 (2007) 709-717.
- [27] P.S. Lee, H.C. Noh, Inelastic buckling behavior of steel members under reversed cyclic loading, *Engrg. Struct.* 32 (2010) 2579-2595.
- [28] P.S. Lee, H.C. Noh, C.K. Choi, Geometry-dependent MITC method for a 2-node iso-beam element, *Struct. Eng. Mech.* 29 (2008) 203-221.
- [29] S.W. Lee, Y.H. Kim, A new approach to the finite element modelling of beams with warping effect, *Int. J. Numer. Methods Engrg.* 24 (1987) 2327-2341.
- [30] Y.L. Pi, M.A. Bradford, B. Uy, Nonlinear analysis of members curved in space with warping and Wagner effects, *Int. J. Solids Struct.* 42 (2005) 3147-3169.
- [31] A. Prok \ddot{a} , New warping function for thin-walled beams. I: theory, *J. Struct. Engrg.* 122 (1996) 1437-1442.
- [32] M. Živkovic, M. Koji, R. Slavkovi, N. Grujovi, A general beam finite element with deformable cross-section, *Comput. Methods Appl. Mech. Engrg.* 190 (2001) 2651-2680.
- [33] G.A. Gunnlaugsson, P.T. Pedersen, A finite element formulation for beams with thin walled cross-sections, *Comput. Struct.* 15 (1982) 691-699.
- [34] F. Laudiero, M Savoia, Shear strain effects in flexure and torsion of thin-walled beams with open or closed cross-section, *Thin-Walled Struct.* 10 (1990) 87-119.

- [35] H. Shakourzadeh, Y.Q. Guo, J.L. Batoz, A torsion bending element for thin-walled beams with open and closed cross sections. *Comput. Struct.* 55 (1995) 1045-1054.
- [36] S.W. Park, D. Fujii, Y. Fujitani, A finite element analysis of discontinuous thin-walled beams considering nonuniform shear warping deformation, *Comput. Struct.* 65 (1997) 17-27.
- [37] T.M. Roberts, H. Al-Ubaidi, Influence of shear deformation on restrained torsional warping of pultruded FRP bars of open cross section, *Thin-Walled Struct.* 39 (2001) 395-414.
- [38] R.E. Fatmi, Non-uniform warping including the effects of torsion and shear forces. Part I: A general beam theory, *Int. J. Solids Struct.* 44 (2007) 5912-5929.
- [39] E.J. Sapountzakis, V.G. Mokos, 3-D beam element of composite cross section including warping and shear deformation effects, *Comput. Struct.* 85 (2007) 102-116.
- [40] M.K. Ferradi, X. Céspedes, M. Arquier, A higher order beam finite element with warping eigenmodes, *Engrg. Struct.* 46 (2013) 748-762.
- [41] A. Genoeses, A. Bilotta, G. Garcea, A mixed beam model with non-uniform warpings derived from the Saint Venant rod, *Comput. Struct.* 121 (2013) 87-98.
- [42] V.G. Mokos, E.J. Sapountzakis, Secondary torsional moment deformation effect by BEM, *Int. J. mech. Sci.* 53 (2011) 897-909.
- [43] S.Y. Back, K.M. Will, A shear-flexible element with warping for thin-walled open beams, *Int. J. Numer. Methods Engrg* 43 (1998) 1173-1191.
- [44] F. Minghini, N. Tullini, F. Laudiero, Locking-free finite elements for shear deformable orthotropic thin-walled beams, *Int. J. Numer. Methods Engrg.* 72 (2007) 808-834.
- [45] E. Carrera, G. Guunta, P. Nali, M. Petrolo, Refined beam elements with arbitrary cross-section geometries, *Comput. Struct.* 88 (2010) 283-293.

- [46]] R. Gonçalves, M. Ritto-Corrêa, D. Camotim, A large displacement and finite rotation thin-walled beam formulation including cross-section deformation, *Comput. Methods Appl. Mech. Engrg.* 199 (2010) 1627-1643.
- [47] J. Wackerfuß, F. Gruttmann, A nonlinear Hu–Washizu variational formulation and related finite element implementation for spatial beams with arbitrary moderate thick cross-sections. *Comput. Methods Appl. Mech. Engrg.* 200 (2011) 1671–1690.
- [48] A.D. Stemple, S.W. Lee, A finite element model for composite beams undergoing large deflection with arbitrary cross-sectional warping, *Int. J. Numer. Methods Engrg.* 28 (1989) 2143-2160.
- [49] A. Prokic, Thin-walled beams with open and closed cross-sections, *Comput. Struct.* 47 (1993) 1065-1070.
- [50] K. Yoon, Y.G. Lee, P.S. Lee, A continuum mechanics based beam finite element with warping displacements and its modeling capabilities. *Struct. Engrg. Mech.* 43 (2012) 411-437.
- [51] K Yoon, P.S. Lee, Modeling the warping displacements for discontinuously varying arbitrary cross-section beams, *Comput. Struct.* 131 (2014) 56-69.
- [52] K Yoon, P.S. Lee, Nonlinear performance of continuum mechanics based beam elements focusing on large twisting behaviors, *Comput. Methods Appl. Mech. Engrg.* 281 (2014) 106-130.
- [53] C. Basaglia, D. Camotim, N. Silvestre, Torsion warping transmission at thin-walled frame joints: kinematics, modelling and structural response, *J. Constr. Steel Res.* 63 (2007) 709–717.
- [54] M.A. Crisfield, G. Jelenic, Objectivity of strain measures in the geometrically exact three-dimensional beam theory and its finite-element implementation, *Proc. R. Soc.* 455 (1999) 1125–1147.

- [55] A. Ibrahimbegovic, F. Frey, I. Kozar, Computational aspects of vector-like parametrization of three-dimensional finite rotations, *Internat. J. Numer. Methods Engrg.* 38 (1995) 65–3673.
- [56] Ritto-Correa, D. Camotim, On the differentiation of the Rodrigues formula and its significance for the vector-like parameterization of Reissner–Simo beam theory, *Internat. J. Numer. Methods Engrg.* 55 (2002) 1005–1032.
- [57] E.A.S. Neto, D. Peric, D.R.J Owen, *Computational Method for Plasticity: Theory and Applications*, Wiley & Sons, 2008.
- [58] ADINA R&D, *ADINA theory and modeling guide*, Watertown, MA: ADINA R&D, 2013.
- [59] ANSYS Inc., *Theory reference-Large deformation analysis*, ANSYS user’s manual, 2012
- [60] M. Schulz, F.C. Filippou, Non-linear spatial Timoshenko beam element with curvature interpolation, *Internat. J. Numer. Methods Engrg.* 50 (2001) 761–785.
- [61] J.C. Simo, L. Vu-Quoc, A three-dimensional finite strain rod model. Part II: computational aspects, *Comput. Methods Appl. Mech. Engrg.* 58 (1986) 79–116.
- [62] G. Jelenic, M.A. Crisfield, Geometrically exact 3D beam theory: implementation of a strain invariant finite element for statics and dynamics, *Comput. Methods Appl. Mech. Engrg.* 171 (1999) 141–171.
- [63] J.M. Andeson, N.S. Trahair, Stability of monosymmetric beams and cantilevers, *J. Struct. Div. (ASCE)* 98 (1972) 2647–2662.
- [64] J.M. Battini, *Co-rotational Beam Elements in Instability Problems*, Technical Report, Royal Institute of Technology, Stockholm, 2002.
- [65] J. Wackerfuß, F. Gruttmann, A mixed hybrid finite beam element with an interface to arbitrary three-dimensional material models, *Comput. Methods Appl. Mech. Engrg.* 198 (2009) 2053–2066.

[66] K.J. Bathe, A.P. Cimento, Some practical procedures for the solution of nonlinear finite element equations, *Comput. Methods Appl. Mech. Engrg.* 22 (1988) 59-85.

[67] M. Ritto-Correa, D. Camotim, On the arc-length and other quadratic control methods: Established, less known and new implementation procedures, *Comput. Struct.* 86 (2008) 1353-1368.

[68] Z.X. Li, A co-rotational formulation for 3D beam element using vectorial rotational variables, *Comput. Mech.* 39 (2007) 309-322.

